

# WETTING PROPERTIES OF FLAT-TOP PERIODICALLY STRUCTURED SUPERHYDROPHOBIC SURFACES

THÈSE N° 3692 (2006)

PRÉSENTÉE LE 29 NOVEMBRE 2006

À LA FACULTÉ DES SCIENCES ET TECHNIQUES DE L'INGÉNIEUR  
Laboratoire d'optique appliquée  
SECTION DE MICROTECHNIQUE

ÉCOLE POLYTECHNIQUE FÉDÉRALE DE LAUSANNE

POUR L'OBTENTION DU GRADE DE DOCTEUR ÈS SCIENCES

PAR

**Laura BARBIERI**

laurea di dottore in chimica, Università degli Studi di Genova, Italie  
de nationalité italienne

acceptée sur proposition du jury:

Prof. M.-O. Hongler, président du jury  
Dr P. Hoffmann, directeur de thèse  
Prof. H. Gouin, rapporteur  
Prof. P. Muralt, rapporteur  
Dr D. Quéré, rapporteur



ÉCOLE POLYTECHNIQUE  
FÉDÉRALE DE LAUSANNE

Lausanne, EPFL

2007



*... a voi, mamma e papà,  
che da lassú illuminate la mia vita,  
e continuate ad essere il mio esempio  
oggi come ieri, e domani per sempre...*



---

# Index

<b>Abstract</b>	<b>1</b>
<b>Riassunto</b>	<b>3</b>
<b>1 Introduction</b>	<b>7</b>
1.1 Wetting properties of solid surfaces: contact angle measurements	7
1.2 Wetting properties of solid surfaces: chemistry and roughness	8
1.3 Thesis motivation	11
1.4 Thesis outline	12
<b>2 Superhydrophobic surfaces: State of the art</b>	<b>15</b>
2.1 Introduction	15
2.2 Classic models	16
Wenzel's model for wetted regime	16
Cassie's model for composite regime	18
2.3 Recent theoretical and experimental developments	20
What is the model that should be applied for predicting contact angle on a rough surface?	20
How to predict contact angle hysteresis?	22
How do gravity and contact line tension influence contact angle?	28
What is the ideal roughness shape and size to promote superhydrophobicity?	32
2.4 Conclusions	33
<b>3 Flat hydrophobic surfaces</b>	<b>35</b>
3.1 Introduction	35
Silanization reaction	36

---

3.2	Developed silanization process	38
	Materials	39
	Substrate pre-treatment: cleaning and hydration	39
	Gas-flow apparatus and silanization process parameters	40
3.3	Surface characterization techniques	41
	Contact angle measurement	41
	Transmission electron microscopy (TEM)	42
	Grazing incidence X-ray reflectivity (GIXR)	42
	X-ray photoelectron spectroscopy (XPS)	43
	Atomic force microscopy (AFM)	43
	Weathering resistance	43
3.4	The obtained hydrophobic coating	43
	Impact of substrate pre-treatment and gas-flow silanization parameters	43
	Coating characterization	47
3.5	Conclusions	54
<b>4</b>	<b>Superhydrophobicity: Static contact angle investigations</b>	<b>55</b>
4.1	Theoretical background	55
4.2	Measuring static contact angles	64
4.3	Static contact angle results	65
	Influence of p, spacing between consecutive pillars	65
	Influence of d, cylindrical pillar diameter	70
	Influence of h, cylindrical pillar height	71
	Influence of L, top-surface pillar perimeter	73
	Influence of pillar absolute size	77
	Influence of f, Cassie roughness parameter	79
4.4	Conclusions	80

---

<b>5</b>	<b>Superhydrophobicity: Adv- and Rec-CA investigations with a negligible extra-pressure</b>	<b>83</b>
5.1	Measuring dynamic contact angles with a negligible extra-pressure	83
5.2	Dynamic contact angle results	85
	Influence of pillar spacing on Cassie-Wenzel transition	85
	Influence of pillar diameter on Cassie-Wenzel transition	90
	Influence of pillar height on Cassie-Wenzel transition	92
	Influence of pillar absolute size on Cassie-Wenzel transition	95
	Superhydrophobicity: a macroscopic property of micro- and nano-meter structures	104
	Influence of pillar top-surface perimeter on Cassie-Wenzel transition	108
5.3	Conclusions	112
<b>6</b>	<b>Superhydrophobicity: Adv- and Rec-CA investigations with a non-negligible extra-pressure</b>	<b>115</b>
6.1	Measuring dynamic contact angles with a non-negligible extra-pressure	115
6.2	Introduction	117
6.3	Dynamic contact angle results	118
	Sample series with 10- $\mu\text{m}$ diameter pillars ( $h = 4d$ )	119
	Sample series with 4- $\mu\text{m}$ diameter pillars ( $h = 10d$ )	123
6.4	Super oil-repellent microstructured substrates	125
6.5	Conclusions	129
<b>7</b>	<b>Conclusions</b>	<b>131</b>
7.1	Results summary	131
7.2	Future work	134
	<b>Appendix 1: Silicon microstructuring</b>	<b>137</b>
	Silicon as reference substrate	137

---

---

Periodically microstructured silicon substrates	137
<b>Appendix 2: Tests of Extrand's model on the experimental Cassie-Wenzel transition</b>	<b>141</b>
Extrand's model	141
Comparison with static contact angle results shown in Chapter 4	142
<b>Appendix 3: Comments on other literature data</b>	<b>145</b>
Experiments description	145
Discussion	147
<b>References</b>	<b>149</b>
<b>Acknowledgments</b>	<b>161</b>
<b>Curriculum vitae</b>	<b>163</b>



---

# Abstract

In recent years, superhydrophobic surfaces have attracted a considerable amount of attention from the academic and industrial communities. This growing interest is mainly caused by the fundamental physico-chemical theoretical aspects that remain obscure and the number of promising practical applications emerging in a wide range of fields, such as textiles, self-cleaning coatings, and micro-fluidic systems. Superhydrophobic surfaces exhibit simultaneously high static water contact angles and low resistance to liquid motion on the surface (i.e. low contact angle hysteresis). These properties result from the combination of the chemical hydrophobicity of the topmost layers of the surface and its roughness, the latter being the dominant factor.

In this PhD work, advantage has been taken of recent advances in micro-/nano-processing technologies to fabricate microstructured surfaces with specific and controlled roughness. This has enabled systematic experimental investigations to be carried out to address some of the still unanswered questions relating to superhydrophobic phenomena.

Silicon wafers were microstructured by photolithography in order to obtain periodical distributions of well-defined flat-top obstacles. A gas-phase silanization process was used to cover the prepared microstructured surfaces with a hydrophobic dense mono-layer of perfluorodecyltrichlorosilane. Several series of samples in which each roughness parameter (distance between obstacles, obstacle height, obstacle size, obstacle shape, etc.) was individually varied were fabricated, and static and dynamic contact angle variations as a function of each parameter were studied.

The results obtained by water contact angle measurements were compared to the classic Wenzel and Cassie models. The first assumes that the liquid wets the asperities of the rough substrate completely (referred to as *wetted* state), whilst the second describes the liquid as sitting on a mixture of air and solid (referred to as *composite* state). By systematically varying a given parameter, a transition between the *composite* and the *wetted* regime was observed. Simple thermodynamic considerations based on the energy minimization of the drop-substrate system showed that Cassie and Wenzel contact angles correspond to two energy minima of the system. Experimentally, the Cassie regime is observed when the Cassie angle is the absolute energy minimum, while when the Wenzel angle is the absolute energy minimum, either the

---

Wenzel regime or a metastable Cassie state is observed. The existence of these metastable states is explained theoretically by the energy barrier that the system has to overcome to reach the Wenzel state when a drop is gently deposited on the surface, and good agreement with experimental data is demonstrated.

Water and *n*-hexadecane dynamic contact angle measurements performed in two different configurations, i.e. with a “negligible” and a “NON-negligible” extra-pressure exerted on the drop-substrate system, permitted the validity of the theoretical model proposed to be confirmed. They clearly evidenced the region of stability of both Wenzel and Cassie regimes, and particularly the region where the Cassie regime is metastable, which is the really interesting one for all the potential applications of rough superhydrophobic surfaces as self-cleaning, and non-sticking surfaces, since only the metastable *composite* states are those characterized by a very high contact angle and a very low contact angle hysteresis, the two main requirements for a good superhydrophobic surface.

With systematic reduction of the absolute size of the obstacles in the micrometer range, an increase in the extent and robustness of the *composite* states was observed. Drop contact line fragmentation seems to be the most important factor in determining the extent and robustness of the observed *composite* states. Results obtained by varying the obstacle top-surface shape demonstrate that contact line length and corrugations are only secondary factors. Studies on the influence of asperity absolute size performed in the micrometer range, together with preliminary but fundamental results obtained on nanostructured substrates, allow the proposal of interesting conclusions concerning determination of roughness size where macroscopic superhydrophobicity appears and vanishes. A typical size of  $\sim 50 \mu\text{m}$  (where “typical size” refers to the width of the obstacle top-surface) can be considered the upper limit of the superhydrophobicity scale range, with a length scale of some tens of nanometers as the lower limit. In this range, the length scale comprised between several hundred nanometers and one micrometer can be assumed the most suitable size for obtaining superhydrophobic properties of larger extent and robustness. The related appropriate asperity height must be sufficiently great to prevent the drop meniscus from touching the bottom of the asperities by vibration, inducing a transition to the *wetted* Wenzel state.

**Key-words:** Superhydrophobic surfaces; surface roughness; contact angle; contact angle hysteresis; three-phase contact line; Wenzel model; Cassie model.

---

# Riassunto

Negli ultimi anni, le superfici super-idrorepellenti hanno attratto un interesse considerevole sia da parte della comunità scientifica che da quella industriale. Questo crescente interesse è dovuto principalmente ai fondamentali aspetti fisico-chimici che restano ancora oscuri e alle numerose promettenti applicazioni pratiche in un'ampia varietà di campi, quali quello tessile, dei ricoprimenti auto-pulenti, dei sistemi utilizzati in microfluidica. Sono denominate "superfici super-idrofobiche" quelle superfici che poste in contatto con una goccia d'acqua esibiscono contemporaneamente un alto angolo di contatto, e una bassa resistenza al moto del liquido (i.e. un basso valore dell'isteresi dell'angolo di contatto). Queste proprietà sono impartite alla superficie dalla combinazione di due fattori: la natura idrofobica della chimica superficiale, e la rugosità superficiale, quest'ultima essendo il fattore determinante.

In questo lavoro di tesi, sono stati sfruttati i vantaggi costituiti dai recenti progressi avvenuti nelle tecnologie di micro-/nano-fabbricazione per realizzare superfici microstrutturate con una rugosità specifica e controllata. Questo ha permesso di effettuare indagini sperimentali sistematiche finalizzate a rispondere ad alcune delle questioni ancora aperte nel campo dei fenomeni di super-idrofobicità.

Attraverso le tecniche standard della fotolitografia, substrati di silicio sono stati strutturati al fine di ottenere delle distribuzioni periodiche di ostacoli microscopici a superficie piatta. Per omologare tutti i substrati ad un'unica chimica superficiale idrofobica, è stato utilizzato un processo di deposizione di perfluorodeciltriclorosilano in fase gas. Sono state fabbricate diverse serie di campioni, ciascuna relativa alla variazione di uno solo dei parametri di rugosità definiti inizialmente (quali la distanza tra ostacoli successivi, l'altezza dell'ostacolo tipo, la sua dimensione tipica, la forma della sua superficie superiore, etc.), e la variazione degli angoli di contatto statico e dinamici (cioè in avanzamento e in ritrazione) è stata studiata in funzione di ogni parametro di rugosità.

Tutti i risultati ottenuti attraverso misure dell'angolo di contatto con acqua sono stati comparati ai modelli classici di Wenzel e di Cassie, il primo che assume un contatto completo tra il liquido e il substrato (riferito come stato *bagnato*), il secondo che descrive la goccia di liquido sospesa su una superficie composta da solido e da aria (riferito come stato *composito*). Variando sistematicamente un preciso parametro di rugosità alla volta, è stato possibile localizzare una transizione tra lo stato *composito* e quello *bagnato*. Semplici considerazioni di

---

natura termodinamica, basate sulla minimizzazione dell'energia del sistema goccia-substrato considerato, hanno mostrato che gli angoli di contatto di Cassie e di Wenzel corrispondono a due minimi di energia del sistema. Sperimentalmente, il regime di Cassie si osserva quando questo rappresenta il minimo di energia, mentre, quando il minimo di energia assoluto è rappresentato dall'angolo di Wenzel, si possono osservare o il regime di Wenzel, o uno stato di Cassie metastabile. L'esistenza di stati *compositi* (Cassie) metastabili è spiegata teoricamente attraverso l'identificazione di una barriera di energia che il sistema deve superare per raggiungere lo stato di Wenzel, nel caso in cui una goccia delicatamente depositata sulla superficie rugosa assuma lo stato di Cassie. In questo contesto, tutti i risultati sperimentali raccolti hanno mostrato un buon accordo con le previsioni teoriche.

Misure dinamiche di angolo di contatto, svolte sia con acqua che con *n*-hexadecano, in due diverse configurazioni dell'apparato di misura (i.e. applicando sul sistema goccia-substrato una pressione extra in un caso "trascurabile" e nell'altro "NON trascurabile") hanno permesso di confermare la validità del modello teorico proposto. Queste hanno evidenziato chiaramente le regioni di stabilità di entrambi i regimi di Wenzel e di Cassie, e soprattutto la regione di metastabilità del regime di Cassie, il quale rappresenta il solo realmente interessante per tutte le eventuali applicazioni dove una superficie super-idrofobica sia necessaria per le sue proprietà autopulenti e anti-adesive, in quanto soltanto gli stati *compositi* metastabili sono quelli caratterizzati da un alto angolo di contatto, e da una bassa isteresi, le due proprietà fondamentali di una superficie super-idrofobica di buona qualità.

Variando in modo sistematico le dimensioni assolute dell'ostacolo nella scala micrometrica, si è mostrato che il rimpicciolimento dell'ostacolo genera un aumento dell'estensione e della robustezza dello stato *composito* di Cassie. La frammentazione della linea di contatto è risultata essere il fattore più importante nel determinare l'entità di tali tendenze. Sulla base dei risultati ottenuti variando la forma della superficie superiore dell'ostacolo è stato possibile dimostrare che la lunghezza e la tortuosità della linea di contatto rappresentano fattori secondari. Lo studio svolto sulle micro-strutture in funzione delle dimensioni assolute dell'asperità, insieme ai risultati preliminari ma fondamentali ottenuti su substrati nano-strutturati, hanno permesso di suggerire interessanti conclusioni rispetto al problema di determinare l'intervallo di dimensioni dell'ostacolo dove la super-idrofobicità appare e svanisce, cosiccome, all'interno di questo intervallo, la taglia ottimale per cui la super-idrofobicità presenta le migliori caratteristiche (angolo di contatto alto, e isteresi bassa).

---

Una dimensione tipica di  $\sim 50 \mu\text{m}$  (dove per “dimensione tipica” si intende l’ampiezza della superficie superiore dell’ostacolo) puo’ essere considerata come il limite superiore dell’intervallo di dimensioni dove si osserva la super-idrofobicit , mentre alcune decine di nanometri il limite inferiore. In questo intervallo, dimensioni comprese tra alcune centinaia di nanometri e un micron possono essere considerate quelle per le quali si presenta una super-idrofobicit  di maggiore estensione e robustezza. L’altezza dell’asperit  pi  appropriata si ritiene debba essere sufficientemente grande da evitare che il menisco presente tra un’asperit  e l’altra tocchi la base delle asperit  in seguito ad eventuali vibrazioni, fenomeno che indurrebbe l’inevitabile transizione allo stato di Wenzel-*bagnato*.

**Key-words:** Superfici super-idrofobiche; superfici rugose; angolo di contatto; isteresi dell’angolo di contatto; linea di contatto tri-fasica; modello di Wenzel; modello di Cassie.

---

---

# 1 Introduction

## 1.1 Wetting properties of solid surfaces: contact angle measurements

The wetting of liquids on solid surfaces is a research topic of fundamental interest [1] with a variety of technological implications. Micro-fluidics for biotechnology, thin film technology, lubrication, textiles, self-cleaning and anti snow-sticking surfaces are just some examples of applications where it has a significant impact.

Experimentally, the wetting properties of solids can be investigated by contact angle measurements of a sessile drop on the surface, which is an easy to handle technique requiring only a small area of the surface to be studied. Three values are normally required:

- the static contact angle  $\theta$ , i.e. the contact angle of the drop in equilibrium (Fig. 1.1);
- the advancing contact angle  $\theta_a$ , i.e. the contact angle of the drop when water is added to the drop, corresponding to the advancing motion of the three-phase contact line (Fig. 1.2-a);
- the receding contact angle  $\theta_r$ , i.e. the contact angle of the drop when water is sucked out from the drop, corresponding to the receding motion of the three-phase contact line (Fig.1.2-b).

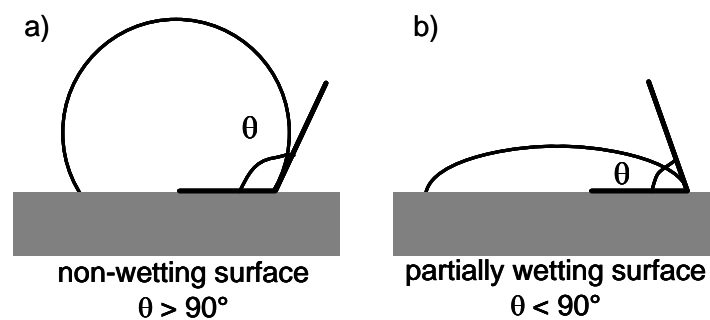


Fig. 1.1 Static contact angle representation for a “non-wetting” surface (a), and for a “partially wetting” surface (b).

If a surface is tilted, the drop begins to move when the lower contact angle reaches the advancing angle and the upper contact angle reaches the receding angle (Fig. 1.2-c). The range

of angle  $\Delta\theta = \theta_a - \theta_r$  is referred to as contact angle hysteresis, and correlates with the ability of a drop to move on the surface.

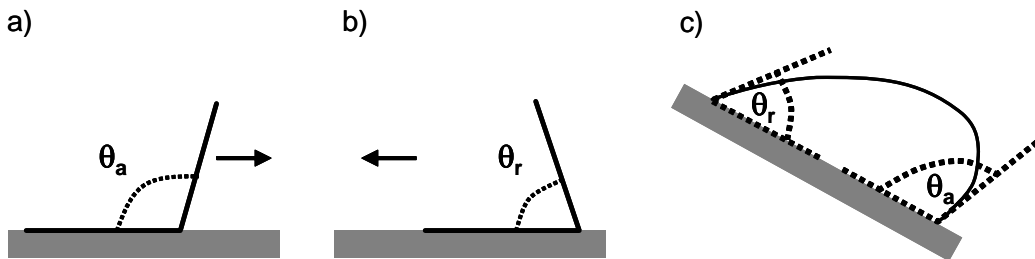


Fig. 1.2 (a) Advancing contact angle, (b) receding contact angle, and (c) advancing and receding contact angles shown by tilting experiments.

## 1.2 Wetting properties of solid surfaces: chemistry and roughness

The behavior of a liquid drop on a solid surface depends mainly on two solid properties: the **surface energy**, determined by the chemical nature of the topmost molecular layer of the studied solid, and its **surface roughness**. A very good example combining these two features is offered by nature: the superhydrophobic/self-cleaning properties of lotus flower leaves (Fig. 1.3-a). This explains why liquid super-repellency is often referred to as the “*Lotus effect*” [2][3]. This natural phenomenon can be ascribed to the low surface energy of the paraffin layer covering the surface leaves and its 3-D morphology. In fact, the surface consists of a random distribution of micron-scale paraffin crystals, which in scanning electron microscope investigations even exhibit nano-scale sub-structures (see Fig. 1.3-b).

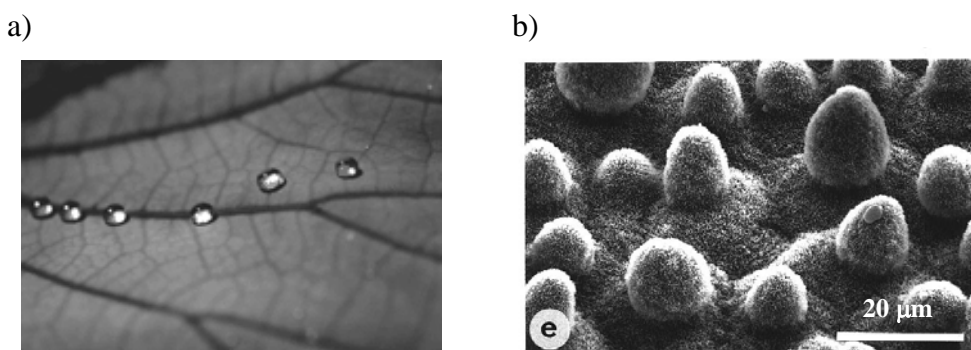


Fig. 1.3 a) Superhydrophobicity of lotus flower leaves: millimeter water drops lie like spheres on the surface, showing contact angles of  $180^\circ$ , or roll off the surface very easily. (b) Scanning electron microscope image of wax crystalloids on surface of lotus flower leaf (*Nelumbo nucifera*) [2].



In recent years, the rapid development of microscopy and micro-/nano-processing technologies has given a renewed impetus to research in the wide field of solid wetting properties, with particular attention being devoted to superhydrophobic surfaces [4][5][6][7], i.e. surfaces that, similarly to lotus flower leaves, exhibit both high water contact angles (greater than 150°) and low hysteresis. Studies on super-repellent surfaces first appeared in scientific literature in the 1930s thanks to Robert Wenzel [8], and ever since this subject has received continued attention [9]-[18]. However, interest has intensified over the last ten years [19]-[55] due to the potential of super-lyophobicity (i.e. general super-repellency to any liquid) in a variety of applications, such as super-repellent fabrics, self-cleaning surfaces, microfluidics devices, and drag reduction in fluid flow [56].

Chemically, the most hydrophobic flat surfaces (i.e. those with lowest surface energy) are fluorocarbon compositions, such as Teflon-based copolymers, which exhibit water contact angles comprised between 110° and 120° [48]. The highest reported water contact angle measured on a “flat” surface was 120° and was obtained on regularly aligned closest-hexagonal packed fluoromethyl- groups (-CF<sub>3</sub>) (see references in [57] or Chapter 3). The lowest critical surface energy ever reported is  $\gamma_c = 5.6$  mN/m, and was obtained by Hare [58][59] on a “flat” self-assembled monolayer of perfluorolauric acid (CF<sub>3</sub>-(CF<sub>2</sub>)<sub>11</sub>-COOH) adsorbed on a platinum foil. Much effort has been invested in the preparation of hydrophobic coatings [60]-[63], especially by alkyl- or perfluoroalkyl-silanization [64]-[66]. However, it was long ago recognized that surface roughness has a much more pronounced effect on hydrophobicity than does surface chemistry [8]. Contact angles approaching 180° have been observed and shown to be experimentally not very sensitive to surface chemistry [37].

Depending on the surface fabrication technique, roughness inducing superhydrophobicity may be observed on irregular or random obstacles [7][14][28][31][67]-[69], regularly micro-textured surfaces [6][35][37][44][47][53][70]-[73], fractal or hierarchical structures [27]-[29][43][74], and nano-rod or nanotube forests [52][75]-[78][83].

The contact angle  $\theta_{\text{flat}}$  that a drop of a certain liquid forms in contact with an ideally flat, homogeneous and rigid surface is expressed by the Young equation (1805) [79]

$$\cos \theta_{\text{flat}} = \frac{\gamma_{\text{SV}} - \gamma_{\text{SL}}}{\gamma_{\text{LV}}} \quad (1.1)$$

where  $\gamma_{\text{SV}}$ ,  $\gamma_{\text{SL}}$  and  $\gamma_{\text{LV}}$  are the interfacial free energies per unit area of the solid-vapor, solid-liquid, and liquid-vapor interfaces, respectively.

Two models describe the contact angle between a liquid drop and a rough surface, depending on the configuration adopted by the drop:

- The first model, proposed by Wenzel (1936) [8], describes the case of complete wetting of a liquid drop on the rough surface asperities (referred to as *wetted* regime). The corresponding so-called “*Wenzel apparent contact angle*”  $\theta_{\text{wet}}$  is expressed by the equation

$$\cos\theta_{\text{wet}} = r \cos\theta_{\text{flat}} \quad (1.2)$$

where  $r$  is the Wenzel roughness factor, defined as the ratio between the actual area of the rough surface and the geometric projected area, which is always larger than 1. Thus, the equation indicates that in the *wetted* regime, the surface roughness enhances the hydrophilicity of hydrophilic surfaces (i.e.  $\theta_{\text{flat}} > 90^\circ$ ) and the hydrophobicity of hydrophobic surfaces (i.e.  $\theta_{\text{flat}} < 90^\circ$ ).

- The second model, proposed by Cassie and Baxter (1944) [9], describes the liquid drop as being suspended at the asperities’ surface, with air pockets trapped among the asperities (referred to as *composite* regime). The “*Cassie apparent contact angle*”  $\theta_{\text{comp}}$  is expressed by the equation

$$\cos\theta_{\text{comp}} = f r_f \cos\theta_{\text{flat}} - (1 - f) \quad (1.3)$$

where  $f$  is the Cassie roughness factor, defined as the fraction of the solid-liquid interface at the drop-surface contact base,  $r_f$  the roughness ratio of the wet area, and  $(1 - f)$  the fraction of the solid-air interface at the same drop-substrate contact base.

These models, which can be derived by the surface energy minimization of a hemispherical drop sitting on a rough surface, under a certain number of assumptions [49] (see next section), are used in almost all scientific studies in the field, since they approximately describe all experimental data.

Following the pioneering work of Wenzel and Cassie, many scientists have focused their interest on the understanding of wetting phenomena on rough surfaces, proposing many interesting experimental results together with improved and revised theories to explain them [32][35][37][42][44]-[51]. Although much progress has been made, many points remain incompletely understood, that should be further investigated by more systematic experimental studies. Some examples of outstanding questions relate to: 1) a good criterion for predicting which kind of wetting regime (*composite* or *wetted*) occurs on a selected rough surface; 2) the relative stability of *composite* metastable states; 3) the influence of the main roughness

parameters on the Cassie-Wenzel transition; 4) the effect of the contact line on stationary and dynamic wetting phenomena; 5) the ideal roughness size and shape of a robust superhydrophobic surface; 6) the range of asperity absolute size where the superhydrophobicity occurs.

## **1.3 Thesis motivation**

The aim of this thesis project has been to focus on understanding the influence of roughness on the wetting properties of regularly micrometer- and submicrometer- structured substrates, hydrophobized by perfluorosilanization. The approach adopted has been to start with rigorous experimental observations, systematically comparing the static and dynamic contact angle values exhibited by prepared substrates as a function of each individual geometrical roughness parameter. All the defined roughness parameters considered together describe all the possible variations of a rough surface constituted by a regular distribution of the same flat-top model obstacle.

The main objective has been to show experimentally the potential of existing physico-chemical laws concerning wetting phenomena, in order to contribute to the understanding of mechanisms that are still not fully understood and yet have considerable impact on a variety of technological, environmental and biological processes.

At the beginning of this thesis work, the most important outstanding questions were defined (listed in the previous paragraph), and the attempt to shine a new light on them has constituted a strong motivation throughout the planning and development of this project.

A truly systematic and extensive experimental approach, to provide concrete and precise answers to at least some of the above-mentioned fundamental aspects, has not yet been conceived. Numerous valuable experimental and theoretical contributions have however been published both prior to and during this work, confirming the continuous and growing interest of the scientific community in the topic.

The thesis work reported here thus represents an attempt to compensate for this lack, presenting and discussing in a systematic and rigorous way a large number of contact angle experiments.

To conclude, it must be remembered that every experiment presented here, with the related discussions, was conceived and performed with the aim of linking it to all the others,

each constituting not a separate and floating “drop” in the huge “ocean” of “solid-wetting” phenomena, but strictly adhering to the others to form a coherent ripple in this fascinating sea...

### 1.4 Thesis outline

In Chapter 2, a theoretical and experimental “state of the art” in the field of superhydrophobicity is presented. The classic Wenzel and Cassie models are described, together with variations subsequently proposed by other authors, and experimental contributions generally considered as supporting references for these theories.

Chapter 3 presents the realization method, and the complete characterization of the hydrophobic perfluorosilane coating deposited on all the structured substrates studied in this work, in order to make them all comparable in their non-wetting surface chemical composition.

In Chapter 4, the results obtained by water static contact angle measurements as a function of each defined geometrical roughness parameter are presented and discussed on the basis of the thermodynamic interpretation of the Wenzel and Cassie approaches. A simple theoretical model is also described in order to predict the position of the transition between the *composite* Cassie and the *wetted* Wenzel regime observed for each roughness parameter.

Chapter 5 describes the experimental results acquired as a function of each defined roughness parameter, by water advancing and receding contact angle measurements performed with a negligible extra-pressure exerted on the drop-substrate system. Here the validity of the previously presented theoretical interpretation is emphasized. Moreover, qualitative and phenomenological considerations are proposed to explain the observed contact angle hysteresis tendency and the influence of the three-phase contact line features on the extent of the *composite* state, both aspects being studied when absolute asperity size falls within the micrometer- and submicrometer range. In conclusion, the optimum roughness considerations size range of superhydrophobic pillar-like surfaces is suggested.

In Chapter 6, the results of dynamic contact angle measurements with a NON-negligible extra-pressure exerted on the drop-substrate system are presented and discussed in term of the thermodynamic interpretation described in Chapter 4. The metastability region of the Cassie-*composite* regime as a function of different geometrical roughness parameters is clearly shown, by the comparing the two possible wetting regimes (*composite* and *wetted*) observed on the same rough substrate, depending on the intensity of the pressure exerted on the drop-substrate system.

A new wetting state, referred to as “super-wetted” state of a rough substrate, associated with a *wetted* regime with hysteresis values as high as  $120^\circ$  (i.e. high advancing contact angle, and particularly very low receding contact angle), is shown to be specific to the substrate that has geometrical roughness similar to that where thermodynamics predicts the Cassie-Wenzel transition.

As further support to the proposed interpretation, contact angle values obtained on microstructured substrates using *n*-hexadecane instead of water are presented.

In Chapter 7 general conclusions are drawn, and future work suggested.

Finally, the annex section comprises:

- I. Description of the method used to prepare the micro-structured substrates.
- II. Extrand’s model tests applied to the experiments presented in Chapter 4.
- III. Comments on other literature data.



---

## 2 Superhydrophobic surfaces: State of the art

*In this chapter, an overview on the theoretical and experimental state of the art in the field of superhydrophobicity is presented. The chapter begins with a description of the most important classic models (Wenzel and Cassie models), and continues the trip through the literature, trying to discuss the fundamental aspects that should be addressed when dealing with the considered topic.*

### 2.1 Introduction

A little exercise, just for curiosity...

If we perform a quick bibliographic research, considering all scientific articles published “before”, and “after 2002” (i.e. year of the reported Ph.D. work beginning), mentioning in the abstract, or key-words list, terms as “superhydrophobic surfaces” or “wetting *and* rough surfaces”, we surprisingly discover that until the end of 2002 there are about 100 publications on the topic, in contrast to the over 200, published in the following last 4 years...

All together, they are surely far to constitute a complete and omni-comprehensive bibliographic research on the argument, however such a result is very effective to demonstrate the very recent growing interest in all scientific aspects related to superhydrophobicity. As already mentioned, the main motivation may derive from the numerous applications that a deep understanding of superhydrophobic phenomena suggests in various fields, from microfluidics for biotechnology to textiles or self-cleaning surfaces.

Moreover, the proposed exercise helps in justifying the impossibility to make this section fully exhaustive in the description and discussion of the whole literature in the field. Here the reader will find information concerning a limited number of contributions, precisely those considered the most representative in the topic by the author, also on the basis of the number of citations they present.

Although some of the articles published in parallel to this work present experiments similar to those performed by the author, or discuss aspects that are also considered here, it has

to be precised that all the presented experimental results, discussed in this report on the basis of thermodynamic considerations, remain original. With the remarks made concerning fundamental aspects in the topic, as the possible interpretation of the contact angle hysteresis results, or the influence of contact line features on the extent and robustness of metastable Cassie states, the author hopes that the results presented here could suggest interesting future digressions especially to the theoreticians working in the field.

## 2.2 Classic models

It is well known that chemistry and roughness are the two main factors in determining the wetting behavior of a surface. However, roughness has been recognized to play the most important role already long ago [8]-[14].

In particular, a liquid drop deposited on a rough substrate can adopt two configurations: either the liquid completely wets the asperities (referred to as *wetted* configuration), or the drop is suspended over air pockets (referred to as *composite* configuration) (see Fig. 2.1).

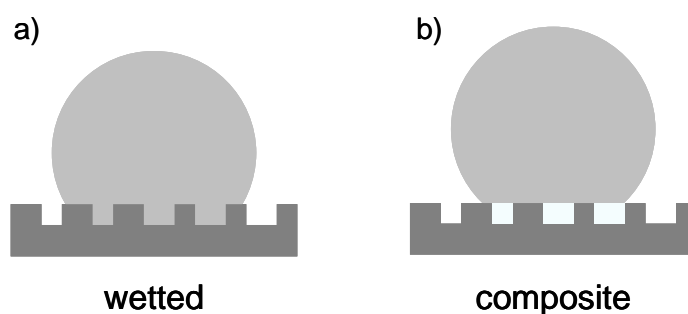


Fig. 2.1 *Wetted* (a) and *composite* configuration (b) of a liquid drop deposited on a rough surface.

In the following sections, these two configurations are considered, and the models predicting the related apparent contact angle (already mentioned in the previous chapter) are described with more details.

### Wenzel's model for *wetted* regime

Derived by Wenzel exactly 60 years ago [8] studying the water-proofing of fabrics, it empirically relates the apparent liquid contact angle  $\theta_W$  formed from a drop in contact with a rough surface to the contact angle  $\theta_{\text{flat}}$  shown by the same liquid deposited on a flat surface with the same chemical composition. The Wenzel contact angle is determined by the equation



$$\cos \theta_W = r \cos \theta_{\text{flat}} \quad (2.1)$$

where  $r$  is the roughness ratio, defined as the ratio between the actual and projected solid surface area ( $r = 1$  for a smooth surface, and  $> 1$  for a rough surface) and it assumes that the liquid completely penetrates into the roughness grooves (Fig. 2.2). Because of this, such a situation is referred to as *wetted* regime.

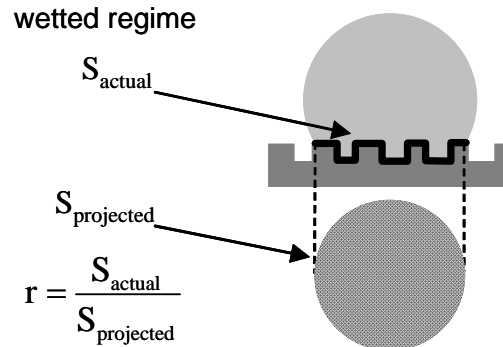


Fig. 2.2 Definition of the Wenzel roughness ratio  $r$  related to the *wetted* regime.

Eq. 2.1 implies that the wetting properties of a specific chemical surface is reinforced by roughness: increasing the roughness ratio  $r$ , a hydrophilic or partially wetting surface (i.e. with  $\theta_{\text{flat}} < 90^\circ$ ) will become superhydrophilic, whereas a hydrophobic surface (i.e. with  $\theta_{\text{flat}} > 90^\circ$ ) will become super-hydrophobic. Actually, this tendency was demonstrated experimentally [85], and intelligent methods for chemical [86][88] or photo-induced [87] reversible switch between superhydrophobicity and superhydrophilicity were proposed by varying  $\cos \theta_{\text{flat}}$  from negative to positive. It has to be noted that the Wenzel law loses its meaning in case of too big roughness ratio  $r$ , since  $\cos \theta_W$  cannot be larger than 1.

The Wenzel equation was derived in a rather intuitive way, averaging the fine details of the roughness, and defining the apparent contact angle as the angle that minimizes the surface energy of the drop during a hypothetical displacement  $dx$  of the contact line [35] (see Fig. 2.3). The surface energy change  $dE$  associated with the contact line displacement  $dx$  can be expressed by the equation

$$dE = r (\gamma_{\text{SL}} - \gamma_{\text{SV}}) dx + \gamma_{\text{LV}} dx \cos \theta_W \quad (2.2)$$

respect to the contact line unit length. Equilibrium corresponds to the minimum of energy. If  $r = 1$  (i.e. on a flat surface) the Young equation is obtained (Eq. 1.1), whereas the Wenzel law (Eq. 2.1) is obtained for a rough surface ( $r > 1$ ).

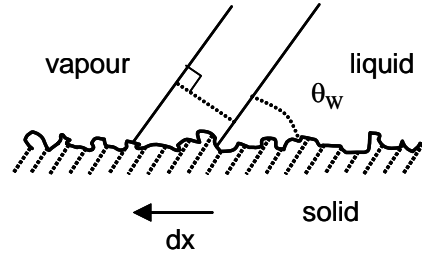


Fig. 2.3 Wenzel's model: hypothetical small displacement  $dx$  of the contact line on a rough surface.

Recently, several authors, as Swain and Lipowsky [32], Wolansky and Marmur [81][82], derived the Wenzel law by detailed thermodynamic considerations. In particular, Marmur reveals [81] that the Wenzel equation is an approximation improving when the drop becomes larger in comparison with the typical roughness size. The question of the limit roughness size where it should apply has not been fully understood yet. On the basis of some simulations and preliminary experimental results [84], it seems that such an equation applies if the considered drop is two or three orders of magnitude larger than the roughness size. In addition, it has been established that the Wenzel contact angle represents the most stable apparent contact angle on a rough surface, corresponding to the global minimum of the system free energy [49][82].

### Cassie's model for *composite* regime

Proposed in the general form by Cassie [10] in 1948, this model empirically describes the liquid apparent contact angle  $\theta_C$  on heterogeneous solid surfaces composed of two different materials, each one characterized by a specific liquid contact angle on the corresponding flat surface  $\theta_{flat}$ . The Cassie law can be expressed by the equation

$$\cos \theta_C = f_1 \cos \theta_{(1)flat} - f_2 \cos \theta_{(2)flat} \quad (2.3)$$

where  $\theta_{(1)flat}$  and  $\theta_{(2)flat}$  are the contact angles on the flat surfaces of the two different materials, and the factors  $f_1$  and  $f_2$  represent the related area fractions. Eq. 2.3 implies that the Cassie apparent contact angle is the weighted average of the different contact angles presented by the chemically different materials constituting the considered surface. The weighted averaging is done according to the area fraction of each chemistry.

Also the Cassie equation results an approximation that improves when the drop size becomes larger with respect to the typical size of the chemical heterogeneity [84], and

similarly to the Wenzel case, the Cassie contact angle represents the most stable apparent contact angle corresponding to the global minimum of the system free energy [49][84].

As previously reported (Chapter 1), when a rough chemically homogeneous surface is considered, air bubbles may be trapped in the roughness grooves, under the liquid. In this case, referred to as *composite* regime, the solid surface may be considered constituted by two chemical compounds where air is the second chemistry to be considered in Eq. 2.3. Such an equation may be thus applied in the form

$$\cos\theta_{\text{comp}} = f r_f \cos\theta_{\text{flat}} - (1 - f). \quad (2.4)$$

This law was proposed by Cassie and Baxter [9] considering  $\theta_{(2)\text{flat}}$  in Eq. 2.3 equal to  $180^\circ$  for water drop in air. The  $f$  parameter represents the fraction of the solid surface in contact with the liquid,  $r_f$  its roughness ratio, and  $(1 - f)$  the fraction of the air surface in contact with the liquid at the drop base (see Fig. 2.4). For  $f = 1$ , then  $r_f = r$ , and Eq. 2.4 turns into the Wenzel equation.

The existence of the *composite* state was demonstrated experimentally: with solidification of molten tin on a rough silica substrate [89], with impedance spectroscopy [90], using a UV polymerized liquid monomer [52]. With these techniques, no partial filling of the roughness by the liquid was observed.

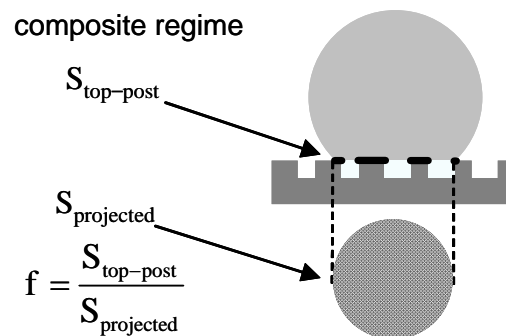


Fig. 2.4 Definition of the Cassie roughness factor  $f$  corresponding to the surface fraction of the liquid-solid contact area related to the *composite* regime.

However, molecular dynamics studies [91] of wetting on a nanometer pillar surface as a function of the pillar height showed some intermediate filling of the roughness by the liquid (drop radius 2 nm,  $\theta_{\text{flat}} = 83.3^\circ$ , pillar diameter 1.2 nm, height varying from 3.4 Å to 61.4 Å).

## 2.3 Recent theoretical and experimental developments

The classic Cassie and Wenzel models were shown to empirically describe the apparent contact angle on rough surfaces in a good qualitative way. Systematic and experimental studies on model rough surfaces in order to investigate the bases of superhydrophobicity were initiated more than 60 years ago [11]-[13], and saw a more or less continuous interest [14]-[26] until about 10 years ago, when the experimental success in producing polymeric superhydrophobic surfaces by the Japanese research group of Kao Corporation [27][28] turned on an extraordinary growing interest for surface superhydrophobicity. In the last three, four years, such an interest has even seen an exponential increase (see Introduction paragraph).

Recently, a rigorous and detailed theoretical analysis of the fundamental bases of the two classic models have been independently proposed by several researchers, as Drelich [23]-[26], Marmur [33][45][46][81][82][84], Swain-Lipowsky [32][38], Extrand [42][55][95], Patankar [49]-[51]. In parallel, a wide range of techniques have been developed to produce superhydrophobic surfaces in a well controlled way in the micrometer range, including processes like photolithography and silanization of silicon wafers [37][71], siloxane sol-gel molding and silanization [35], Si wafer dicing and silanization [44], PDMS molding [53][70][73], molding and UV-curing of a mixture of perfluoro-/non perfluoro-acrylates [47], photolithography with deep reactive ion etching inducing Teflon<sup>®</sup>-like polymer passivation [72], and in the nanometer range, especially by e-beam lithography or UV-photolithography, and etching [52]. Practically, all produced rough surfaces have been the object of experimental wetting investigations, but only a few of the proposed theories [25][26][42][55][49][50] have been tested by concrete experimental data, and the others remain too much complicated for being applied to real experimental cases.

### **What is the model that should be applied for predicting contact angle on a rough surface?**

Already long ago, experimental variation of some surface roughness parameters showed to induce a change of wetting regimes between *composite* and *wetted* modes [14]. As briefly mentioned in the previous paragraph (and accurately in the first paragraph of Chapter 4), thermodynamic analysis shows that Cassie and Wenzel contact angles are respectively connected to two free energy minima of a drop on a rough surface [46][51][70], being the energetically favored state between the two possible (i.e. *wetted* or *composite*) that associated

with the lower contact angle. A thermodynamic criterion (Eq. 4.12, in Chapter 4), expressed as a function of surface geometrical parameters, was proposed by Bico et al. [92] to predict which regime is that thermodynamically favored. However, experience shows that drops on rough surfaces do not always present the wetting configuration with the absolute minimum energy, and in particular, metastable *composite* states have been frequently observed when liquid drops are smoothly deposited on rough surfaces [47][51][53][93]. This metastability was associated with the idea of an energy barrier to overcome to reach the *wetted* state [49][51][70][93]. Experimentally, it was proven that providing energy to the drop, either by applying a force on it [47], or dropping it from some height [50], or dragging it on the rough surface [72], would no longer lead to a metastable *composite* state but to a *wetted* state. It was also proven that such metastable states are not observed when the drop is formed on the surface by condensation from the vapor phase [47]. The reasons and details of the energetic transition from a metastable *composite* state to a *wetted* state are unknown, but it was proposed that the energy barrier can be estimated as the energy required to fill with water the surface asperities, keeping the *composite* contact angle constant [51] (see calculations in Chapter 4). This assumption, so far tested by Patankar [51] only on a few experimental data of Yoshimitsu [44], in Chapter 4 will be applied to several experiment series, each one considering one selected geometrical roughness parameter.

An approach based on considerations far from thermodynamics was proposed by Extrand [42] to predict advancing and receding contact angles. This is based on the assumption that contact angles manifest themselves as fractional contributions along the contact line on the surface. He formulated two fundamental criteria that must be met in order for a surface to show *composite* superhydrophobicity [55]: the first referred to as “contact line density criterion” (obtained balancing the drop weight by the surface forces along the contact line, which was already suggested several decades before [18]), and the second referred to as “asperity height criterion” (obtained by assuming a meniscus curvature at the liquid-air interface among the asperities). These criteria were tested by Extrand with reasonable agreement on experiments selected in literature, from He [50], Yoshimitsu [44], Oner [37] and Bico [35]. However, more systematic investigations would be needed to validate such a model, which appear theoretically not as valuable as thermodynamic derivation, since it is based on still to be proven assumptions. Additionally, the quantitative comparison with the experimental results produced during this work is not so convincing, as it is shown in Appendix 2.

## How to predict contact angle hysteresis?

As briefly precised in Chapter 1, superhydrophobicity requires high contact angle and low contact angle hysteresis, permitting the drop to roll off the surfaces for a very small tilt angle, as recognized by several authors [42][36][94][46][52], some even claiming that the hysteresis value is even more important than the absolute contact angle value [36][94]. Concerning this aspect, the “rolling” motion associated with drops in *composite* regime on rough surfaces was recently verified, in contrast to the “sliding” motion, at least in the case of drop radii smaller than the capillary length [96].

The force required for inducing a drop deposited on a surface to move is related to the hysteresis by the equation given by Furmidge [31]

$$F = mg \frac{(\sin \alpha)}{\omega} = \gamma_{LV}(\cos \theta_{adv} - \cos \theta_{rec}) \quad (2.5)$$

where  $m$  and  $\omega$  are the mass and the width (parallel to the direction movement) of the drop,  $\alpha$  is the minimum tilt angle at which the drop will spontaneously move,  $g$  is the gravity acceleration. Such a force  $F$  is the pinning force that the drop experiments at the contact line, and that has to be overcome by external forces (i.e. gravity) for inducing the drop motion.

It is considered that contact angle hysteresis derives from the deviations of a real surface from the ideal condition, and it is associated with the existence of many thermodynamic metastable states related to the systems having three-phase (solid-liquid-vapor) boundaries, with a different intrinsic contact angle for each metastable state. Practically, contact angle hysteresis has been attributed to different causes, like surface roughness [8][11][13]-[15][85][97], surface chemical heterogeneity [12][16][17][98]-[101], drop size effect [102][103][105], molecular re-orientation [106] and surface deformation [107][108], inter-diffusion due to the size of the liquid molecules [109], adsorption/desorption phenomena [110][114].

Since it is very difficult to experimentally study ideal surfaces with absolute homogeneity and smoothness at the atomic level, hysteresis remains a strongly discussed topic. The existence of an intrinsic hysteresis was proposed [42][115] due to the specific molecular interactions between the liquid and the solid molecules. On the other hand, it was observed that hysteresis does not exceed a few degrees on surfaces carefully prepared to be smooth and homogeneous [36][105].

The importance of hysteresis in relation to the surface roughness has been discussed in literature since 1948 [11], but Bartell and Shepard in 1953 [13] were the first to report results of systematic studies on the hysteresis values measured on paraffin substrates, roughened in a controlled way. Later, Dettre and Johnson [14] studied the hysteresis behaviour observed on wax surfaces with different  $r$ , Wenzel roughness parameter. Johnson and Dettre showed that static contact angle and hysteresis increase coherently with the roughness parameter  $r$  of the hydrophobic surface. But for  $r$  greater than a certain value, there is an inversion, and the static contact angle increase occurs with a decrease of the hysteresis. This decrease in hysteresis can be qualitatively explained by the switch from Wenzel to Cassie regime, with air trapped at the macroscopic liquid-solid interface. By computer simulations carried out considering an ideal sinusoidal surface roughness [15], they suggested the interpretation of the hysteresis phenomenon as that due to energy barriers that have to be overcome when the liquid moves on the rough surface from a metastable state to another. Although they had the merit to clearly evidence the importance of barrier energies between metastable states, their theory presents the two main disadvantages 1) of being applied on not very realistic surfaces, especially considering the possibility of the current micro-fabrication techniques, and 2) of being based on cumbersome and complicated calculations. The theories proposed later by Neumann and Good [111], Huh and Mason [112], Cox [97], Schwartz and Garoff [113], also present the same drawback of being obscured by mathematical complexity and rest difficult to be applied to the nowadays available textured surfaces.

Presenting new experimental results, obtained thanks to the recently improved micro-fabrications techniques, the most recent contributions [35][37][42][44][49][53][92]-[117] try to be less speculative and complicated, and some of them will be shortly described below.

Bico et al. [35][92] defined a simple criterion (Eq. 4.12), derived by classic Wenzel and Cassie laws, for predicting the advancing contact angle on textured surfaces, and emphasized that the fraction  $f$  of the solid area actually in contact with the liquid (i.e. Cassie roughness parameter) represents the most important parameter. They underlined that for the receding contact angle the question remains open.

McCarthy's group has the merit to have underlined for the first time [36] the strict relation existing between the three-phase contact line characteristics, as shape and continuity, and the hysteresis value observed on very rough surfaces. They considered three different ideal structured surface, as those illustrated in Fig. 2.5.

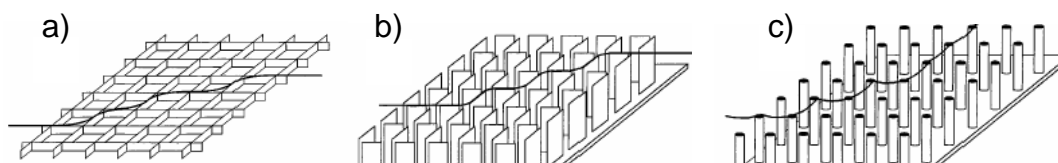


Fig. 2.5 Surface with three different roughness topologies. The dark lines describe possible three-phase contact line: a) continuous contact line; b) separated ridges (intermediate case); c) very discontinuous contact line connecting separated pillars [36].

The best case for minimizing hysteresis was claimed to be the case (c), where the very high discontinuity of the contact line makes negligible the energy difference between different states. The Oner and McCarthy contribution [37] was also the first to show the influence of different geometrical roughness parameters on superhydrophobicity, presenting a systematic investigation of water advancing and receding contact angles on several periodically microstructured and silanized silicon surfaces, with posts of different sizes, shapes and separations. They showed that ordered distributions of square obstacles with  $30\ \mu\text{m}$  as typical dimension, and similar distances, present very high hydrophobicity (water  $\theta_{\text{adv}} \sim 170^\circ$ , water  $\theta_{\text{rec}} \sim 140^\circ$ ). They found such a behavior to be independent of the considered surface chemistry and obstacle height. For the substrates with obstacles of a wider dimension (up to  $128\ \mu\text{m}$ ), and similar distances, both advancing and receding angles decrease. This was interpreted by the increase of the three-phase contact line length and by the augmented pinning of water at the asperity edges, both aspects due to the liquid penetration between the obstacles. When the distance between obstacles with characteristic size lower than  $32\ \mu\text{m}$  is increased, they found that a maximum in receding contact angle is achieved, presumably due to the water penetration between the obstacles. Although the contribution is valuable for the many data provided, the observations made concerning contact line continuity, length, and shape constitute an unclear point. The receding angle increase (i.e. the contact angle hysteresis diminution) observed by increasing the distance between the posts, and varying post shape, is in fact ambiguously related to the contact line length and fragmentation. Other remarks about the Oner and McCarthy approach are expressed in Chapter 4, as well as in Appendix 3.

In the experiments of Yoshimitsu et. al [44], the approach is different than that of Oner and McCarthy. In contrast to the direct measurement of advancing and receding contact angle, Yoshimitsu performed wetting investigations on microstructured and hydrophobized silicon substrates by static contact angle measurements, and sliding angles measured for drops of



different weight. By systematically varying also the height of the obstacles, he showed that for a certain microscale roughness the liquid intrusion between the obstacles does not take place for drop volume (i.e. weight) lower than a critical value. In this contribution, as soon as gravity force induces the liquid sinking into the cavities, and Wenzel's contribution becomes more significant, the sliding angle increases for higher structures. Further comments on Yoshimitsu's experiments are reported in Appendix 3.

The theory proposed by Patankar et al. [49][53], bases on the surface energy minimization of the drop-substrate system, explains the multiple equilibrium wetting regimes observed on the same rough substrate, and suggests a possible method for predicting the contact angle hysteresis on a certain substrate, depending on the considered regime. In particular, although the formulae proposed for predicting the advancing contact angle are shown to work properly in the case described by Bico et al. [35], those proposed for predicting the receding contact angle lead to a significant discrepancy from the observed experimental value. To explain such a difference, Patankar et al. repropose the hypothesis already suggested by Roura and Fort [118] assuming that the receding liquid leaves behind a liquid thin film on the asperity surfaces, instead of leaving a dry surface. Always from energy consideration, Patankar derives the equation

$$\cos\theta_{\text{rec}} = 2f - 1 \quad (2.6)$$

which results in agreement with the experiments of Bico [35].

As mentioned in the previous section, the model proposed by Extrand [42] for predicting advancing and receding contact angle considers them to depend on fractional contributions along the contact line. In particular, he defines a "contact line density" criterion, that permits to predict if a drop will assume a *composite* or a *wetted* state, depending on the value of the contact line density associated with the geometrical roughness of the considered rough surface. For contact line density higher than a certain critical value, the drop will assume a *composite* state, whereas for lower values the drop will completely wet the asperities. He describes the hysteresis phenomenon on a pillar-like surface as being directly dependent on the hysteresis measured on the flat surface with the same chemical composition, i.e. the "true" contact angle hysteresis  $\Delta\theta_0$ . In this way, he interprets the high advancing contact angle shown by a *composite* drop as due to the "true" advancing contact angle (i.e. the advancing contact angle on the flat surface) assumed by the drop at the side of the asperity, i.e. respect to the vertical

line at the asperity edge. On the other side, the receding contact angle of the *composite* drop cannot be lower than the “true” receding contact angle (i.e. the receding contact angle on the flat surface), since, in the attempt to form it at the asperity side, the receding contact line jumps to the next asperity. The contact angle hysteresis is finally expressed by the equation

$$\Delta\theta = \lambda_p(\Delta\theta_0 + \omega) \quad (2.7)$$

for *composite* states, and by the equation

$$\Delta\theta = \Delta\theta_0 + 2\lambda_p\omega \quad (2.8)$$

for the *wetted* states, where in both cases  $\lambda_p$  is the linear fraction of the contact line on the asperities, and  $\omega$  is the rise angle at the asperity side. Although the density contact line criterion is shown to be valid for predicting both the *composite* and *wetted* regimes observed by Oner and McCarthy [37], and Bico et al. [35] on their regularly microstructured surfaces, Eqs. 2.7 and 2.8 are in agreement with the hysteresis contact angle values obtained only for drops in *composite* regime. Concerning the discrepancies shown for drops in *wetted* state, the necessity of “better accounting for contact line contours and variations in the contact angles near asperities” suggested by the author seems not satisfying.

A theoretical model for predicting equilibrium contact angle and contact angle hysteresis on a rough substrate has been developed by McHale et al. [116], based on the comparison between the Wenzel and Cassie angles, in relation to their dependence on the contact angle on the flat surface, the shape of the curves obtained for different  $r$  and  $f$  factors (i.e. Wenzel and Cassie roughness parameters respectively), and their derivatives. The key and original point of the proposed model consists in the consideration of the Wenzel and Cassie equations derivatives. Referred to as “gain factors”, they determine the contact angle variation associated with both the Wenzel and Cassie theories, for any perturbation of the contact angle on the flat surface. In this way, McHale and colleagues emphasize that for  $\theta_{\text{flat}} > 90^\circ$  Wenzel theory predicts both an increase in the apparent contact angle and an amplification of any changes from that contact angle value, whereas Cassie theory predicts an increase in the contact angle but an attenuation of any change from that contact angle value.

Assuming the advancing and receding contact angles as being the effects of the perturbations induced by the contact line motion, the suggested method for predicting the contact angle hysteresis on a rough surface considers the hysteresis on the flat surface, and multiplies it by the appropriate “gain factor”. Since the gain factor is larger than unity for the

Wenzel case, and lower than unity for the Cassie case, hysteresis will be increased for drops in the Wenzel regime, and decreased for drops in the Cassie regime.

The most recent model for predicting contact angle hysteresis is that proposed by Li and Amirfazli [117]. Even if it will not be tested by the experimental results described in this work, it seems to represent a surely original and well-grounded interpretation of the Johnson and Dettre classic model. Based on the thermodynamic approach that minimize the free energy of a system constituted by a 3-D structured surface and a drop deposited on it, the Li and Amirfazli theory defines the different possible stable and metastable states. The original aspect is the significant simplification introduced representing the 3-D system in its simplified 2-D version, which practically permits a relatively easy calculation of the energy barriers associated with the advancing and receding motion of the contact line as a function of the pillar width, height and spacing, in both *composite* and *wetted* contact between the drop and the rough surface. By their method, Li and Amirfazli emphasize that Wenzel and Cassie angles calculated for defined surface geometries correspond to minima of free energy, and in particular that, for a Wenzel roughness ratio  $r$  lower than the value where Wenzel and Cassie apparent contact angles are coincident, the *wetted* regime is that thermodynamically favored, and vice versa, for larger  $r$  values, the favored regime is *composite*. Initial definition of the reference positions assumed by the contact line during its motion on the rough surface allows to show the local minima and maxima of the free energy curve as a function of the possible contact angles comprised between the advancing and receding angles. In particular, the related free energy barriers associated with the advancing and receding contact line motions can be calculated considering the difference between the corresponding energy peak and the neighboring energy valley for the advancing process, and between the same energy peak and the opposite neighboring energy valley for the receding process. In this way, the values of the energy barriers associated with the motion of the contact line, in the two possible advancing and receding directions, can be related to a specific contact angle. The contact angle hysteresis value can be derived by the difference between the pairs of contact angle that makes the energy barrier equal to the vibration energy associated with the advancing and receding motion. To simplify, they consider the case where the vibration energy is zero and the related contact angle hysteresis is the maximum exhibited by the system. The authors conclude emphasizing that, on the basis of their model, hysteresis of *composite* states clearly appears not influenced by the  $r$  roughness parameter, since it is independent of the pillar height, differently from the hysteresis of *wetted*

states. With the validation of the experimental results of Oner and McCarthy for microstructures [37], of Lau et al. [76] and Fan et al. [77] for nanostructures, they suggest their model to represent a good criterion for predicting wetting properties on pillar-like surfaces, the transition between *composite* and *wetted* states, and for designing superhydrophobic surfaces.

### **How do gravity and contact line tension influence contact angle?**

The equations of Young, Cassie and Wenzel were derived considering only the surface tension, and assuming that the shape of the drop is hemispherical. However, two additional possible effects can be considered that influence contact angles: they are gravity and contact line effects. Experimentally, these effects were mainly cited to explain the experimental results showing the contact angle variations occurring when the drop volume [102][105][119] is changed, on both flat and rough surfaces. Although in Chapter 4 this two effects will be neglected developing the thermodynamic analysis, it is appropriate to offer here at least a brief description concerning the existing approaches that do not neglect the influence of these factors.

#### **Gravity effect**

In absence of gravity, drops are expected to exhibit a hemispherical shape.

It is currently accepted that the effect of gravity on the drop shape is negligible as long as the drop radius  $R$  is smaller than the capillary length  $\alpha$  [120]

$$\alpha = \sqrt{\frac{\gamma_{LV}}{\Delta\rho g}} \quad (2.9)$$

where  $\Delta\rho$  is the difference between the liquid density and the density of the surrounding air. For water,  $\alpha = 2.7$  cm [47].

Another criterion proposed to verify if gravity can be neglected is to calculate the so-called “drop shape factor” SF (referred to as shape factor [121], or Bond number [122], or Eotvos number [123]) for the considered drop by the equation

$$SF = \frac{\rho g R_0^2}{\gamma_{LV}} \quad (2.10)$$

where  $R_0$  is the radius of curvature at the drop apex, and neglect gravity only for values much smaller than unity.

Usually, in literature, water drops with radius of millimeter size (i.e. with volume up to 10-12  $\mu\text{L}$ ) are considered to be spherical [4][42].

For drops believed to be spherical, simple geometric considerations based on the drop height and diameter [124] permit to determine the contact angle by the equation

$$\tan \frac{\theta}{2} = \frac{H}{r_b} \quad (2.11)$$

where  $H$  is the drop height and  $r_b$  the radius of the drop-solid contact area.

However, this method is not correct for drops affected by gravity, such as large drops or drops of a high density liquid. In this case, the shape of the drop is described by the Laplace equation (with the assumption of an axisymmetric drop)

$$\gamma_{LV} \left( \frac{1}{R_1} + \frac{1}{R_2} \right) = \Delta \rho g z + \Delta P_0 \quad (2.12)$$

where  $R_1$  and  $R_2$  are the radii of curvature in two normal planes,  $z$  is the height of the drop, and  $\Delta P_0$  is the pressure variation across the interface at the drop apex.

The numerical resolution of this equation allows to determine the contact angle value assumed by drops affected by gravity, by fitting images of the drops. Techniques based on this principle are referred to as ADSA (from Axisymmetric Drop Shape Analysis) [123][125] [126]. The values of contact angles defined by this method rely on the combination of two elements:

- an image processing method to evaluate the drop profile from a drop picture. The first image processing method was proposed more than 20 years ago [127], and further on improved [125];

- an algorithm to fit the drop profile obtained by the adopted image processing method based on the Laplace equation solution [123]-[125].

Two main ADSA techniques exist, mainly developed by the Neumann's group (review [126]):

- *ADSA-profile*: permitting simultaneous determination of contact angle, interfacial tension and drop surfaces area and volume [126][128][129]. However, this technique requires the location of the solid substrate.

- *ADSA-contact diameter*: based on experimental measurements of the drop-solid contact diameter, with liquid tension, liquid volume as input parameters (especially good for measurements of very low angles) [130].

For rough surfaces, Cassie and Wenzel laws do not consider gravity, and it was theoretically demonstrated that they do not apply in this case [32].

Concerning theoretical models for the contact angle determination based on energy minimization of the system, some authors include a term of gravity in the energy expression [32][38][132]. However, as no analytical form of the drop shape under gravity exists, few authors tend to propose correction for gravity, and the assumption of considering gravity expressed by the variation of the drop body mass with respect to the contact angle, assuming a hemispherical shape, has been recognized to be a poor assumption (see references in [105]).

### Contact line tension effect

The line tension concept was proposed by Gibbs more than a hundred years ago as the one-dimensional analog of the surface tension. It can be associated with the excess of free energy of a solid-liquid-vapor system per unit length of contact line [133], or with the excess of force acting along the three-phase boundary line of a three-phase system to shorten or lengthen it [134].

Actually, the line tension  $\sigma$  is probably the most controversial quantity in wetting science: physical significance, sign and magnitude remain contentious. Line tension has been the object of a lot of theoretical discussions [102][134]-[137], and several simple estimations of the line tensions were proposed, correlating it with molecular dimensions [38][136][138]. Experimental techniques to estimate line tensions are reviewed in [136].

On an ideal flat, rigid, homogeneous substrate, the line tension influences the contact angle according to the modified Young equation:

$$\cos\theta_{\text{flat}} = \cos\theta_{\infty} - \frac{\sigma}{\gamma_{LV}} K \quad (2.13)$$

where  $K$  is the geodesic curvature on the three phase line,  $\cos\theta_{\infty}$  is the angle obtained for  $K = 0$ . In case of a spherical drop, Eq. 2.13 can be written as follows:

$$\cos\theta_{\text{flat}} = \cos\theta_{\infty} - \frac{\sigma}{\gamma_{LV}} \frac{1}{r_b} \quad (2.14)$$

where  $r_b$  is the radius of the drop-solid contact area. Eq. 2.14 was extensively applied to estimate  $\sigma$  and measure contact angles by varying the drop volume (therefore  $r_b$ ) [102][105][139]-[141]. A huge discrepancy was obtained in literature for  $\sigma$  values: positive or

negative values, and values between  $10^{-16}$  and  $10^{-6}$  J/m, with most values around  $10^{-6}$  J/m (references in [33][38][102][134][136][142]). Recent scanning force microscopy investigations of the liquid surface topography of a three-phase system [133] determined contact line tensions in the range of  $10^{-10}$  to  $10^{-11}$  J/m. With the support of theoretical analyses based on different approaches, such a range is shown to be consistent with theoretical predictions (references in [133][141]). Different considerations explain the discrepancy between the experimental values and the theoretically calculated values:

- $\sigma$  values are extremely small quantities, therefore very difficult to estimate. Young's modified equation is valid for flat, homogeneous surfaces, and homogeneity and smoothness at the atomic/molecular level are extremely difficult to be achieved and controlled [105]. It was proposed that surface heterogeneity significantly influences the contact-angle/drop-size relationship [102], inducing a corrugation of the contact line. Therefore, some authors proposed to consider "a pseudo-line tension" rather than "a line tension" value for the related experimental results [102][103]. Other authors claim that the corrugation of the contact line (varying curvature from point to point) definitely explains the deviation of the experimental results from the values predicted by the classic theories, respectively, of Young for ideal flat surfaces, of Wenzel for *wetted* states on rough surfaces, and of Cassie for chemically heterogeneous surfaces or *composite* states on rough surfaces [45][119][136][138][141].

- According to Eq. 2.14, line tension is important only for small drops. Usually, experiments are carried out with drops showing an  $r_b$  value in the millimeter range, which gives a  $\sigma$  value in the order of  $10^{-6}$  J/m [103].

- $\sigma$  is usually assumed to be constant: however, Marmur proposes that  $\sigma$  should depend on the contact angle [143].

On rough and heterogeneous surface, the line tension is thought to play an important contribution if the scale of roughness or heterogeneity, and consequently of the related contact line curvature radius, is in the order of magnitude of a few micrometers or less [33][136][144].

Two modifications of the classic laws were proposed that consider contact line effects.

- Drelich [136] proposed the equation

$$\cos\theta_C^* = \cos\theta_C - \frac{1}{\gamma_{LV}} \left( \frac{f_1\sigma_1}{r_1} - \frac{f_2\sigma_2}{r_2} \right) \quad (2.15)$$

as revised Cassie's law, where  $r_1$  and  $r_2$  are the contact line curvature radius on the surfaces 1 and 2, respectively, that are different in chemical composition; and the equation

$$\cos\theta_W^* = \cos\theta_W - v \frac{\sigma}{\gamma_{LV}} K \quad (2.16)$$

as revised Wenzel's law, where  $v$  is the actual length of the contact line over the apparent length of the geometrical contact line, and  $K$  the geodesic curvature of the contact line.

- Swain and Lipowsky [32] proposed the equation

$$\cos\theta^* = \sum_i r_i \left( \cos\theta_i - \frac{\sigma C_i}{\gamma_{LV}} \right) + \Delta\rho g \bar{Z}^2 \quad (2.17)$$

as general equation for rough and chemically heterogeneous surfaces, where  $r_i$  is the Wenzel roughness ratio of the  $i$  surface,  $\theta_i$  the contact angle on a flat surface of the material of surface  $i$ , and  $C_i$  the curvature of the contact line on the  $i$  surface. It has to be noted that in this expression is also included the gravity effect in the term  $\Delta\rho g \bar{Z}^2$ , where  $\bar{Z}^2$  represents the mean square height of the surface roughness.

### **What is the ideal roughness shape and size to promote superhydrophobicity?**

From the literature excursus so far presented, it is clear that pillar textured surfaces can often exhibit superhydrophobic properties. In particular, general criteria were suggested for designing rough surfaces where *composite* states should be favored. For instance, Patankar et al. [49] suggest that suitable geometrical features for a surface to show superhydrophobicity are those associated with: 1) a spacing between pillars that makes indistinguishable the *wetted* from the *composite* angle (i.e. that corresponding to the intersection point of the Cassie and Wenzel curves); 2) a possibly small values of the ratio between the typical pillar size and its height. Although the Cassie angle does not depend on the asperity height, the latter has an important influence on its robustness. In fact, determining the horizontal position of the Wenzel curve for example in the graph as a function of pitch (see Chapter 4), it defines the region of thermodynamic stability of the two different regimes.

However, the best shape, size, and surface disposition of the pillars have never been clearly indicated, even if some advises have been proposed. By their experiments on microstructured surfaces, Oner and McCarthy [37] suggested a length of 32  $\mu\text{m}$  as the



maximum size imparting *composite* superhydrophobicity (i.e. the one associated with high advancing contact angle, low hysteresis, and small rolling off angle) for surfaces consisting of square posts. Recently, a surface density comprised between 3 and 8% was proposed by Callies et al. [72] concerning micrometer pillars in order to reach maximum contact angles and minimum hysteresis. For robust *composite* states, simultaneous “shrinking” of pillar size and spacing was theoretically previewed [95]. It has also be suggested that designing microtextured surfaces to approach the point where Cassie and Wenzel contact angles are coincident should guarantee a high contact angle [53], although in this case hysteresis would depend on the *wetted* regime [73]. Most promising are probably bio-mimetic hierarchical surfaces, on which a nano-roughness is added to micro-roughness [54][74][145][146].

On the basis of the experimental results obtained during this work, proposition on the ideal asperity roughness size will be suggested in Chapter 5.

## 2.4 Conclusions

This chapter pointed out the main aspects that must be addressed when dealing with wetting properties of solid surfaces, especially in relation to their dependence on surface roughness, in all cases citing the most important contributions appeared in literature.

In the next chapters, presenting and discussing the experimental results obtained in this work, the novelties suggested by them respect to particular approaches selected among the many cited here will be illustrated.



---

## 3 Flat hydrophobic surfaces

*This chapter describes the method adopted in this study to chemically modify the surfaces of all the considered samples, in order to make them all comparable in their hydrophobic surface chemistry. The introduction motivates the choice of using a silanization reaction with perfluoroalkylsilane molecules, and presents also the main features of the process. Subsequently, the conceived and built gas-flow silanization apparatus is described. A complete characterization of the obtained hydrophobic layer is presented, following a brief introduction for each of the used surface analysis techniques.*

### 3.1 Introduction

Hydrophobic/low energy surface coatings have attracted a considerable amount of attention in the last decades, because of their numerous applications in many fields. Some examples are anti-sticking coatings in self-assembly in micro-assembly [147][148], coatings for the release of suspended-cantilever and mobile silicon devices [60][63], and hydrophobic windshield coatings [61][62].

Several techniques exist to produce hydrophobic layers, mainly based on the deposition of organic or perfluoro-organic compounds. Some examples are: (a) radio frequency magnetron sputtering of polymers like polyethylene (PE) or polytetrafluoroethylene (PTFE) [149]-[151]; (b) polysiloxanes ultra-thin layer deposition by activation of Si-H bonds [152]; (c) inorganic-organic polymer films synthesis by two steps sol-gel process [153]; (d) PFTE coatings deposition by ion-plating [154]; (e) radio frequency and microwave plasma-enhanced chemical vapor deposition (PECVD) of organo-silicon compounds and fluoroalkylsilanes gaseous mixture [155][156]; silanization reaction in liquid- or gas-phase with alkyl- or perfluoroalkyl- silane molecules. All the mentioned techniques deal with films that present variable thickness, non-ordered molecular structure, and variable surface morphology depending on the deposition condition and time, except the method based on the silanization reaction. Belonging to the class of the so-called Self-Assembled Monolayers [157][158],

organo-silane based coatings, grafted especially on silicon oxides (or even on other metal oxides and polymeric surfaces) present the peculiarity of a highly ordered structure, with molecules preferably oriented due to the spontaneous chemical reaction at the interface. This aspect is considered the reason why the thickness of the deposited layer should be limited to the order of the maximum molecule size together with its roughness.

Depending on the chosen silane, with specific “functional” and “substituent” groups (e.g. amino-, chloro-, methoxy-, ethoxy-, and alkyl-, perfluoro-, amino-, vinyl-, epoxy-, mercapto-respectively), different molecules can be suitable for different applications, for instance, from adhesion promoter in liquid- and gas-phase chromatography, to surface activator in biosensors for antibodies immobilization, from non-wetting/self-cleaning coatings for optical devices to anti-sticking coatings for MEMS/NEMS technology.

#### **Silanization reaction**

In the last decades, many studies aimed at the fundamental understanding of the silanization reaction [159]-[163] were performed on layers obtained with mono- and tri-functional alkyl-silanes reacting with hydroxylated silica surfaces by a liquid phase process. They showed that the layer properties resulting from the silanization reaction (i.e. molecules orientation with respect to the surface, thickness, chains density) strongly depend on several reaction conditions such as temperature [164]-[166], presence and thickness of the water interfacial layer [163][167][168], and nature of the solvent [169]. Despite the many progresses in the field, discrepancies still exist concerning the way all these factors influence the process and mechanism of the film growth.

The interpretation of the final silane film implies the creation of strong covalent bonds between the silane functional groups and the -OH groups saturating the silicon oxide surface. Monofunctional silanizing agents give rise to a mono-molecular layer, since the single reactive site (e.g. methoxy-, ethoxy-, chloro-) can only bind to one surface silanol group (see Fig. 3.1-a for dimethylchlorosilane), whereas bi- and tri-functional silanes lead to more complex reaction mechanisms, offering the possibility of multiple bonding to the surface as well as lateral cross-polymerization between neighboring silane molecules [161][163][167]. On the other hand, monolayers derived from monofunctional silanes present alkyl chains surface density lower than bi- and tri-functional silanes [170], due to the steric hindrance of the methyl- groups attached to the silicon linker. The reaction control of bi- and tri-functional silane is however

more critic. Since they are very sensitive to both surface adsorbed water and ambient moisture, multi-functional silane molecules can easily polymerize and generate a three-dimensional polysiloxane network (see Fig. 3.1-b for trichlorosilane).

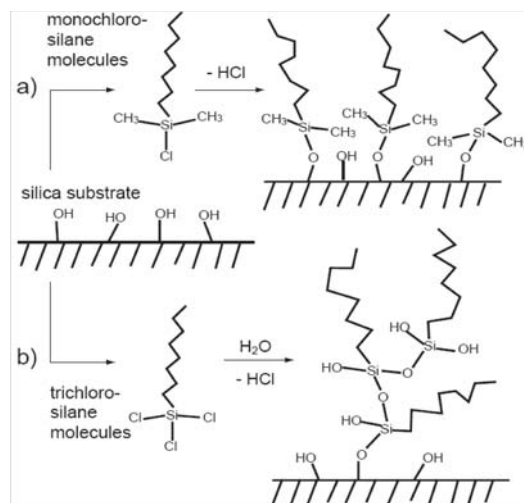


Fig. 3.1 Scheme of the qualitative silanization reaction between (a) mono- and (b) tri-functional silane molecules and the hydroxylated silicon oxide surface.

Among the factors that influence the reaction, the presence of water plays a key role. It has to guarantee the highest concentration of surface reactive -OH groups and it hydrolyzes the Si-X bonds of silane molecules (with X- equal to CH<sub>3</sub>O-, CH<sub>3</sub>CH<sub>2</sub>O-, Cl-) to form Si-OH groups. The silane -OH groups interact through condensation reaction with the surface -OH groups forming Si-O-Si bonds at the substrate and/or with adjacent head groups, creating a cross-linked network at the surface. It has also been reported that the water content in silane solutions affects the mechanism of layer formation, changing it from a continuous growing of a homogeneously disordered layer at low moisture (due to a random and isotropic configuration of molecules), to a heterogeneous island growth, at high water content [171]-[174].

In the liquid process with alkylsilane, molecular aggregations due to van der Waals (VdW) interactions between alkyl-tails should occur already before the adhesion of the silane to the substrate, promoting the formation of a denser layer [157]. In contrast, perfluorinated silane molecules do not experience VdW forces strong enough to be packed as dense as hydrocarbon chains. This depends on the low polarizability of perfluorinated hydrocarbon entities. For the same reason, however, they are the most effective reagents for preparing highly hydrophobic/low energy surface coating [64][175][176]. This leads to their low critical

surface energy. The lowest critical surface energy ever reported is  $\gamma_c = 5.6$  mN/m, and corresponds to a contact angle of  $120^\circ$ , i.e. the highest contact angle value obtained on a flat surface. Such a critical surface energy was measured by Hare on compressed  $-(CF_2)_7-CF_3$  end chains, obtained as Langmuir-Blodgett films of perfluorolauric acid ( $CF_3-(CF_2)_{11}-COOH$ ) adsorbed on an atomically flat platinum foil [58][59]. Moreover, the chemical inertness of perfluorocarbon compounds against acids and bases, as well as against oxidation and thermal decomposition, favor them respect to simple alkylchain coatings. Strong attachment of the chains to the surface and longevity of the coating have to be guaranteed in order to avoid perfluorinated molecules emanation into the atmosphere, that would not be a sustainable solution and therefore not to be applied.

The following paragraph presents the method developed to deposit in a reproducible way a highly non-wetting molecular coating using perfluorodecyltrichlorosilane and shows its long term stability under normal exposure conditions. An optimized gas-flow silanization process is described, and the results obtained by extensive characterization of the highly non-wetting layer are presented. In particular, the use of transmission electron microscopy (TEM) for visualizing the organic molecular layer is emphasized, supported by more standard characterization methods, such as grazing incidence X-ray reflectivity (GIXR). As expected, the measured thickness is similar to the molecule length and confirms that the deposition of trifunctional-perfluoroalkylsilane molecules do not generate a multi-layer coating. The estimation of the coating surface energy was possible by the Zisman plot [59]. Surface homogeneity and surface roughness values were determined by atomic force microscopy (AFM) measurements. X-ray photoelectron spectroscopy (XPS) measurements evidenced the correlation between water repellency and fluorine atomic concentration. Weathering tests proved the good resistance of the coating to the aging process.

## 3.2 Developed silanization process

A gas-phase silanization process was selected since it presents numerous advantages compared to a solution-based process [65][177][178]. The competition between adsorption of reagent molecules and solvent molecules can be avoided and the reaction rate is increases overcoming the limited diffusion rate in liquid solution. Vapor-phase conditions are also

preferred since to maintain a solvents anhydrous dipping hydrated substrate samples into the reaction solution is not possible.

In particular, a “gas-flow” apparatus that allows the surface silanization at atmospheric pressure by continuous evacuation of the reaction by-products and continuous reagent supply was built. Being two separate parts, the liquid silane reservoir and the reaction chamber can be maintained at different temperatures, and the silane molecules in vapor-phase are brought to the substrate by a carrier gas. The substrate pre-reaction treatment constitutes a fundamental phase of the process, especially in the essential hydration step.

## Materials

The perfluoroalkylsilane  $\text{CF}_3\text{-(CF}_2\text{)}_7\text{-(CH}_2\text{)}_2\text{-SiCl}_3$  - referred to as “PF3” - [CAS: 78560-44-8] (ABCR GmbH & Co. KG Germany) was used without any further purification (purity > 97%).

Two different substrates were used for studying each individual reaction parameter:

a) Ordinary microscope glass slides - referred to as “glass” sample - (76 x 25 x 1 mm<sup>3</sup>, Semadeni SA, chemical composition: SiO<sub>2</sub> 72.30%, Na<sub>2</sub>O 14.30%, CaO 6.40%, MgO 4.30%, K<sub>2</sub>O 1.20%, Al<sub>2</sub>O<sub>3</sub> 1.20%, SO<sub>3</sub> 0.30%).

b) Float glass discs - referred to as “silica” sample - (8-mm diameter, 1-mm thick) with a 500-nm SiO<sub>2</sub> layer, deposited by Ar sputtering (SwissOptic AG).

## Substrate pre-treatment: cleaning and hydration

The substrate pre-treatment is a crucial phase of the adopted silanization process. In particular, the cleanliness of the silica substrate must be guaranteed and verified with water contact angle measurements (values > 5° are not acceptable). Cleaning and pre-treatment procedures are applied as follows: after a pre-cleaning step by ultra-sonication in a mixture of distilled water and iso-propanol (1:1) at 50 °C, and drying in a N<sub>2</sub> gas stream, the substrates are exposed to O<sub>2</sub> plasma (Plasmaline 415, Barrel Type Asher, Tegal Corporation<sup>TM</sup>) to complete the oxidation of all the residual organic contaminants at the surface. The O<sub>2</sub> plasma treatment is chosen since it eliminates the risk of contamination absorption associated with wet chemical treatments. Subsequently to the O<sub>2</sub> plasma exposure, and before the introduction in the silanization chamber, each substrate is exposed to a water vapor flow.

### Gas-flow apparatus and silanization process parameters

There are two main advantages of a gas-flow system: first, the silane can be completely isolated from the reaction place, and second, it can also be kept at different temperature than the substrate. A vector gas is used to transport the silane to the substrate and to evacuate the by-products. In this reactor,  $N_2$  is used as carrier gas, flowing through a bubbler filled with pure (97%) liquid silane (see Fig. 3.2).

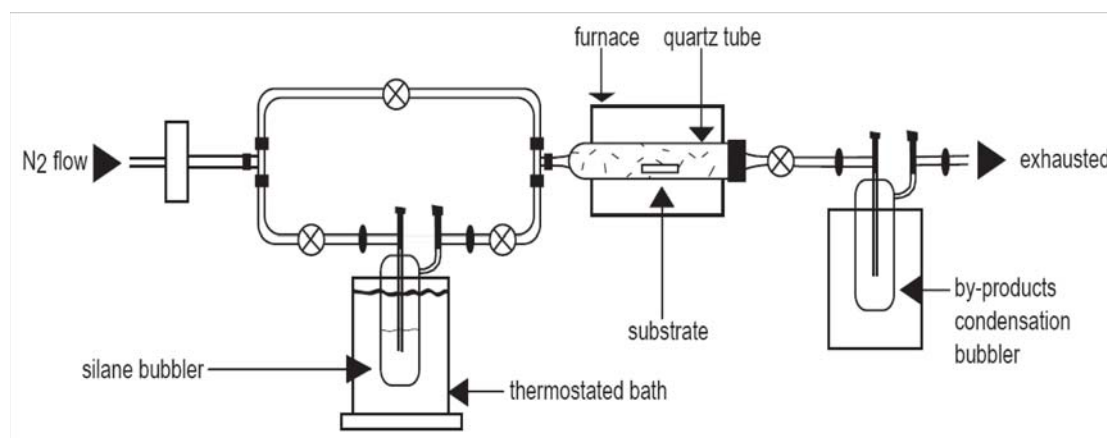


Fig. 3.2 Schematic set-up of the gas-flow system.

The substrate is placed in a quartz tube reaction chamber, which is connected to the gas circuit. A tube furnace maintains the substrate zone at controlled temperature. Two parallel copper gas lines converge in front of the reaction chamber and allow the operator to select indifferently or the pure  $N_2$  gas flow or the silane- $N_2$  gas mixture flow. The gas lines are kept at a controlled higher temperature than that of the silane bubbler bath, in order to avoid the silane condensation along the system. A mass-flow controller regulates the  $N_2$  gas flow. A condenser allows the condensation of by-products and unreacted silane molecules.

The sample is introduced in the quartz tube after the hydration step, while pure  $N_2$  gas flows through the system. The silanization reaction begins when the  $N_2$  gas flow is deviated in the silane bubbler, kept at the desired temperature, and the produced silane- $N_2$  gas mixture reaches the substrate. When the desired reaction time has elapsed, the silane valves are closed and the pure  $N_2$  gas flow is again selected in order to complete the evacuation of by-products and unreacted silane. Then the substrate is extracted from the reaction chamber.

The following parameters were systematically varied:

-  $t_{\text{drying}}$  = pre-reaction desorption time (i.e. exposure time of the substrate to the  $N_2$  gas flow, at



controlled temperature, to eliminate the adsorbed H<sub>2</sub>O excess);

-  $T_{\text{reaction}}$  = reaction temperature (i.e. temperature in the reaction chamber);

-  $t_{\text{reaction}}$  = reaction time (i.e. exposure time of the substrate to the silane-N<sub>2</sub> gas mixture);

-  $T_{\text{silane}}$  = silane temperature (i.e. temperature of the silane bubbler bath);

-  $t_{\text{desorption}}$  = post-reaction desorption time (i.e. exposure time of the silanized substrate to the N<sub>2</sub> gas flow, to eliminate the adsorbed silane molecules and aggregates);

-  $\Phi_{\text{N}_2}$  = vector-gas flow (i.e. N<sub>2</sub> gas flow imposed by the mass-flow controller; range < 90 sccm, where “sccm” designates “standard square centimeter”).

### 3.3 Surface characterization techniques

#### Contact angle measurement

Static and dynamic contact angles were measured at laboratory environment ( $T=23\pm 2$  °C, RH%=50±5) by a homemade system consisting of an optical microscope (Projectina Swiss - Heerbrugg). The conditions of drop formation and deposition were kept constant for reproducibility. Digitized images of the liquid drops were recorded maximum 5 seconds after the drop deposition. All reported values represent the average of ten contact angle values per sample, corresponding to the left and right contact angles of five drops, deposited on the substrate maximum 24 hours after the end of the silanization process. All calculated standard deviation values were never larger than 3°, indicating a good macroscopic homogeneity of the coatings. A complete characterization of the wetting properties of the obtained coating, by static, advancing and receding contact angles measurements [36][179][180], was done on the coated substrates showing water static contact angle equal to, or larger than, 120°.

For determining the critical surface energy (i.e. the surface energy of the hypothetical liquid that spreads in contact with the studied surface), a series of homologue *n*-alkanes was used for the extrapolation at  $\cos\theta = 1$  of the critical value  $\gamma_C$  by the Zisman plot [59]. The following *n*-alkanes were used (whose surface tensions were taken from [181]): C<sub>8</sub>H<sub>18</sub> ( $\gamma = 21.14$  mN/m), C<sub>10</sub>H<sub>22</sub> ( $\gamma = 23.74$  mN/m), C<sub>11</sub>H<sub>24</sub> ( $\gamma = 24.65$  mN/m), C<sub>12</sub>H<sub>26</sub> ( $\gamma = 25.58$  mN/m), C<sub>16</sub>H<sub>34</sub> ( $\gamma = 27.49$  mN/m).

### Transmission electron microscopy (TEM)

A copper-SiO<sub>2</sub> TEM grid was silanized in the gas-flow reactor at optimized parameters (see Fig. 3.3-a). The grid was embedded into a polystyrene resin by an in-situ radical polymerization of distilled styrene. The resin was then cut by ultra-microtomy using a diamond knife to obtain 50-nm thick slices. These lasts were placed onto a TEM grid for a direct observation by transmission electron microscopy (see Fig. 3.3-b). Images were recorded using a Hitachi HF-2000 microscope.

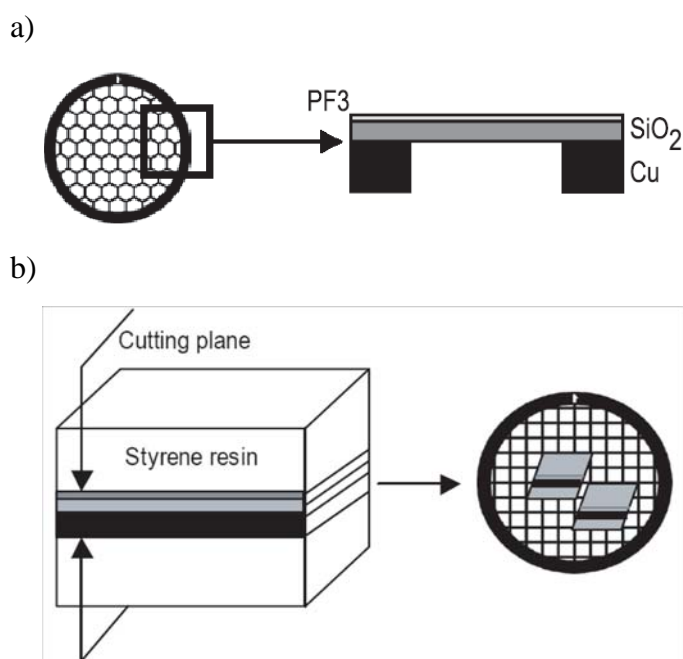


Fig. 3.3 Schematic of the procedure used to prepare the sample for TEM observation. a) Left: Copper-SiO<sub>2</sub> silanized TEM grid. Right: vertical section of a silanized TEM grid fragment. b) Left: zoom of the silanized TEM grid, embedded in a polystyrene resin. Right: 50-nm thick slices deposited on a grid for TEM observation.

### Grazing incidence X-ray reflectivity (GIXR)

X-ray reflectivity measurements of the PF3 thin layers deposited on a thermally oxidized silicon wafer (50-nm SiO<sub>2</sub>) were performed. A PF3 layer deposited on a GaAs substrate covered with a SiO<sub>2</sub> layer, 10-nm thick, deposited by plasma-enhanced chemical vapor deposition (PECVD), represented the reference sample. The experiments were performed at the Swiss Light Source (SLS,) at the Material Science beam line (5-circle diffractometer in horizontal geometry), and on a Bruker D5000 2-circle diffractometer with a special reflectivity stage.

### **X-ray photoelectron spectroscopy (XPS)**

The chemical composition of silica surfaces coated in different conditions in the gas-flow system was analyzed in an X-ray photoelectron spectrometer (Kratos Axis Ultra - UK), equipped with a conventional hemispherical analyzer. The employed X-ray source was the mono-chromatized Al  $K_{\alpha}$  line (1486.6 eV), operating at 150 W. The pass energy was 80 eV for wide-scan, and the acquisition time was 2 min. Analyses were performed under ultra-high vacuum conditions ( $10^{-9}$  Torr) on a sample area of  $300 \times 700 \mu\text{m}^2$ , at take-off angles of  $90^\circ$  and  $20^\circ$  (corresponding to different surface sensitivities). The spectra were calibrated by Au  $4f_{7/2}$ .

### **Atomic force microscopy (AFM)**

The topography of the substrates before and after coating deposition in the optimized conditions was examined in a Topometrix Explorer system ( $\text{Si}_3\text{N}_4$  cantilever with  $k = 0.05 \text{ N/m}$ ), in contact-mode, at laboratory environment ( $T=23\pm 2^\circ \text{C}$ ,  $\text{RH}\%=50\pm 5$ ). The root mean square (RMS) roughness value was calculated from  $1 \mu\text{m} \times 1 \mu\text{m}$  images.

### **Weathering resistance**

Standard weathering tests were carried out in a Vötsch Climatic Cabinet VCL4100 MH, where relative humidity, temperature, and UV-vis irradiation (295 - 780 nm) can be freely varied and monitored. The applied aging cycle of 1-month duration (sub-cycles of 24 h) corresponds to a one-year outdoor exposure. Temperature was varied between  $-15^\circ \text{C}$  and  $+50^\circ \text{C}$ , relative humidity between 15% and 70%, UV-vis irradiation intensity was kept constant at about  $500 \text{ W/m}^2$  (that is about 3 times higher than the natural sunlight in central Europe). Water and *n*-hexadecane static contact angle measurements were performed before and after the aging cycle.

## **3.4 The obtained hydrophobic coating**

### **Impact of substrate pre-treatment and gas-flow silanization parameters**

The state of the cleaned sample surface immediately before any chemical surface treatment is crucial for the final process results. The surface should be completely hydrated and free from any organic contamination.

The hydration phase saturates all the surface active groups created by the O<sub>2</sub> plasma, relaxes highly excited states like dangling bonds, and efficiently completes the hydroxylation of the silica surface. A glass slide that was plasma treated but not hydrated before the silanization process showed a water contact angle of 85° (Fig. 3.4-A). In contrast, a plasma treated and hydrated glass slide, subsequently subjected to the same silanization process, showed a water contact angle of 107° (Fig. 3.4-B).

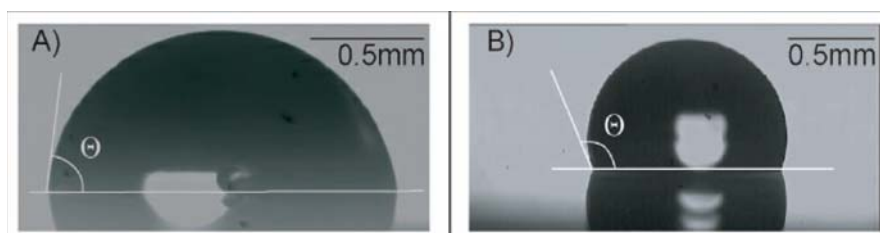


Fig. 3.4 Water repellency of two glass microscope slides silanized during the same process. A) Slide not hydrated after the plasma treatment,  $\theta = 85^\circ$ ; B) slide hydrated after the plasma treatment,  $\theta = 107^\circ$ .

The fundamental aspects regarding the influence of each process parameters (see the list in “Gas-flow system and silanization process parameters” paragraph) are summarized in Fig. 3.5. In the silanization process, the reagents are silane molecules and -OH groups (belonging to H<sub>2</sub>O molecules, or saturating the oxide surface). Therefore, the parameters determining the amount of evaporated silane molecules per time unit, and those that influence the amount of water in the system during the reaction are considered. The amount of evaporated silane molecules that transit in proximity of the substrate per time unit depends on several factors. They are: a) the silane bath temperature ( $T_{\text{silane}}$ ); b) the amount of silane in the bubbler; and c) the N<sub>2</sub> gas flow ( $\Phi_{\text{N}_2}$ ). Only the silane temperature strongly influences the process efficiency. Fig. 3.5-a shows that for the selected conditions ( $\Phi_{\text{N}_2} = 90$  sccm,  $T_{\text{substrate}} = 150$  °C,  $t_{\text{reaction}} = 60$  minutes), increasing the silane bath temperature above 80 °C does not improve the final hydrophobicity of the treated glass substrate. At temperature lower than 80 °C, the reaction is mass-transport limited, whereas for temperature above 80 °C the deposition is chemically limited, and the selected reaction time is largely sufficient for completing the monolayer formation.

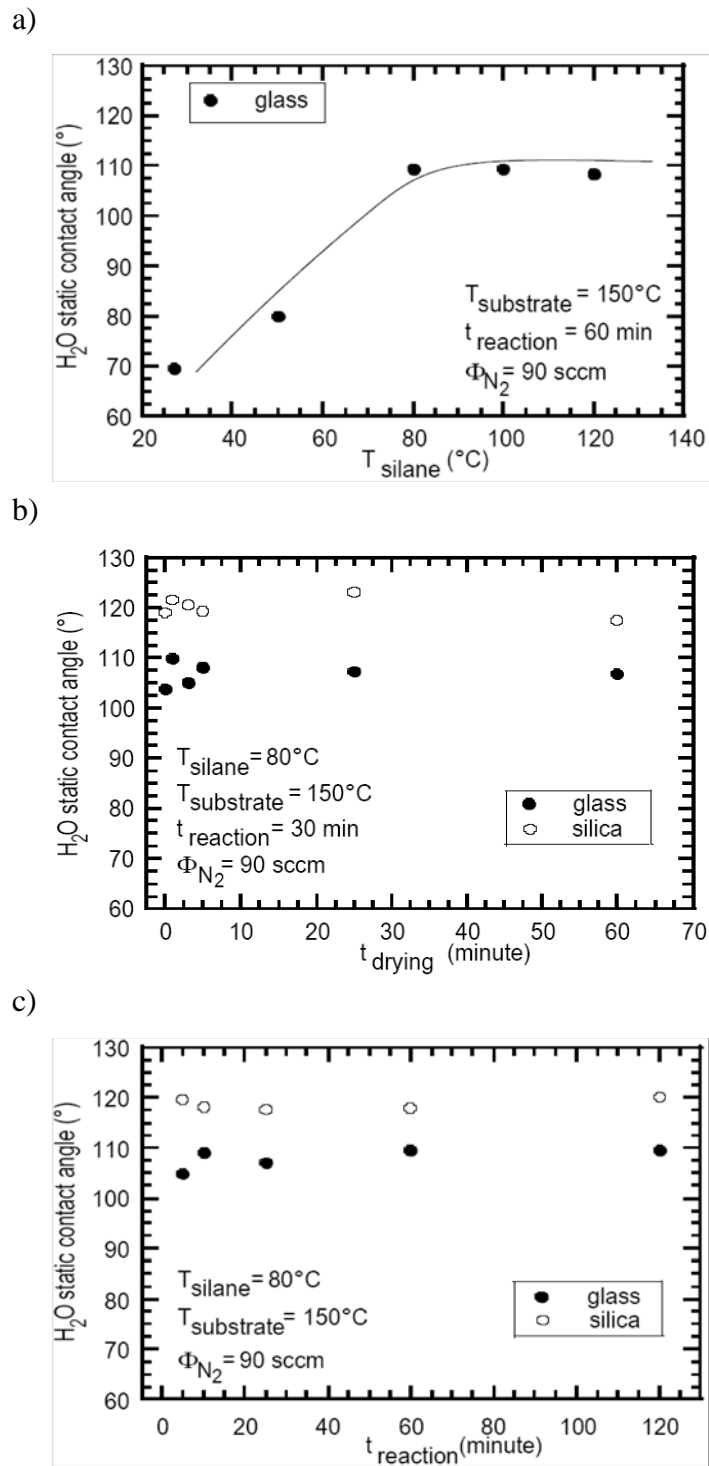


Fig. 3.5 Water static contact angle values for glass and silica substrates silanized in different conditions (see each graph insert). Each graph corresponds to one selected process parameter. Silane temperature is the parameter with the highest influence on water contact angle. The line in a) serves as visual guide.

The excess of molecule evaporated at higher temperature do not participate to the coating formation, and are evacuated together with the reaction by-products. Fig.3.5-b reveals that the

“pre-reaction desorption time” does not play an important role in the efficiency of the process, at least for the considered reaction times. Substrate temperature and N<sub>2</sub> gas flow conditions are not sufficiently strong to eliminate the excess of physically adsorbed H<sub>2</sub>O [182][183] in a few seconds. Since water static contact angle does not change with the drying time, it can be hypothesized that the water molecules of the film adsorbed on the substrate, partially evaporated, hydrolyze the chloro-silane molecules that arrive in the system with the N<sub>2</sub> vector gas. Perfluoroalkylsilanols are bonded via hydrogen bonds to the silanol groups at the silica surface. The condensation reaction takes place, and by continuous vector gas flowing, the subsequent elimination of the water molecules trapped between the organic chains and the substrate leads to the final dense molecular coating, directly grafted to the silica surface. The ideal coating would derive from the so-called horizontal polymerization, where each molecule is chemically linked to the substrate and to other two neighboring silane molecules by three Si-O-Si bridges. So far, the experimental results are not sufficient for claiming to be in the horizontal cross-polymerization ideal case. However, since the contact angle values measured on perfluorosilanzed silica substrates (i.e. static: 123°, advancing: 125°, receding: 111°) are similar to those observed for densely packed CF<sub>3</sub>- groups [184], one can suppose to have a dense layer of perfluorinated chains, with a high fraction of chains presumably perpendicular to the substrate [66]. Fig. 3.5-c shows that 5-minutes exposure of the substrate to the silane-N<sub>2</sub> gas mixture is sufficient to reach the maximum static water contact angle. With an estimated size of the perfluorinated chain cross-section of 0.25 nm<sup>2</sup> in densely packed layers [184][185], and a number of 4.6 -OH groups per nm<sup>2</sup> of a perfectly hydroxilated SiO<sub>2</sub> surface [182][186], it is clear that even in the ideal case of horizontal cross-polymerization, some -OH groups at the substrate surface must remain unreacted [187]. All the experimental results shown in Fig. 3.5 support the general interpretation that the silanization process with amphiphilic silane molecules is limited to a monomolecular layer. After the formation of the first layer, no other silane molecules can react with the still available reactive silanols at the surface because of the steric hindrance due to already linked chains. The discrepancy observed comparing the water repellency of glass and silica substrates exposed to the same silanization process (see Fig. 3.5-b, c) can be explained by the difference in the initial Si-OH surface concentration, since their initial RMS roughness values are comparable. According to the glass composition, the surface concentration of other oxides than SiO<sub>2</sub> should be about 18%, and it is possible that the most appropriate substrate for silanization reaction is silicon oxide.

## Coating characterization

### *Determination of the coating thickness*

TEM of cross-sectional cuts [188][189] and GIXR [190][191] were selected as complementary methods for thickness determination of ultra-thin films. Whereas TEM gives local information and offers a direct measurement of the layer thickness, GIXR averages over large sample surfaces. AFM was not chosen to measure the height difference (step height) between the locally uncoated substrate and the coated parts, since the measured height difference does not correspond to the real thickness of ultra-thin coatings. The measured layer thickness obtained by AFM in fact depends on the chemical composition of the coating molecule (e.g. factors like backbone, terminal groups, molecule stiffness, and creation of a dipole in  $-\text{CH}_2-\text{CF}_3$  [192] chains change the interaction with the scanning AFM tip).

**Transmission electron microscopy.** Fig. 3.6 shows overview dark field TEM images of the coating deposited on the embedded sample obtained by the preparation method previously described.

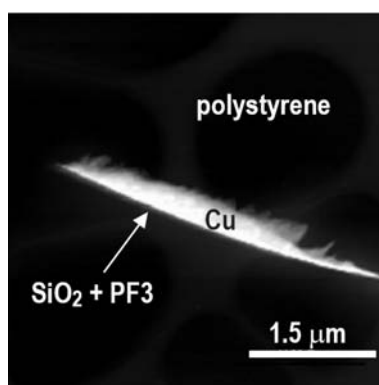


Fig. 3.6 Dark field TEM images of a slice of the resin embedded sample: a copper TEM grid with a  $\text{SiO}_2$  membrane, submitted to a silanization reaction and embedded into a polystyrene resin.

Bright field TEM images of an ultra-thin section of the embedded sample, showing the  $\text{SiO}_2$  film, the perfluorosilane coating and the resin, are presented in Fig. 3.7 at two different magnifications.

Fig. 3.8 illustrates how the thickness of the silane coating was estimated. The intensity profile (Fig. 3.8-b) established from the bright field TEM image (Fig. 3.8-a) was used to draw

the thickness of the thin layer attributed to the PF3 part. The thickness of the PF3 layer deduced by this method is 1.82 nm.

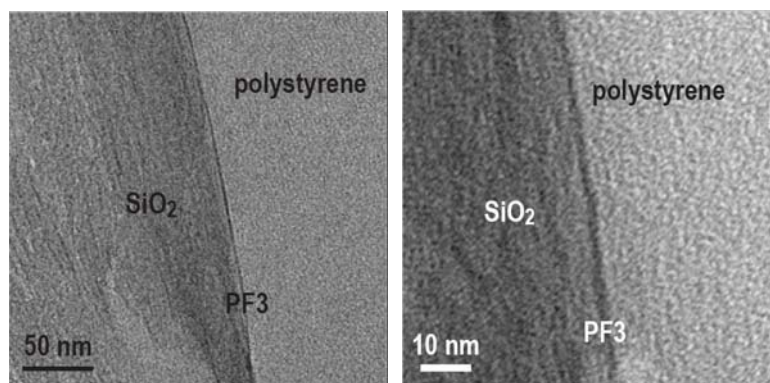


Fig. 3.7 TEM images at different magnifications of the copper-SiO<sub>2</sub> perfluorosilanized substrate, embedded in the styrene resin and sliced. The nanometric thickness of the perfluoro-organic layer is well detectable.

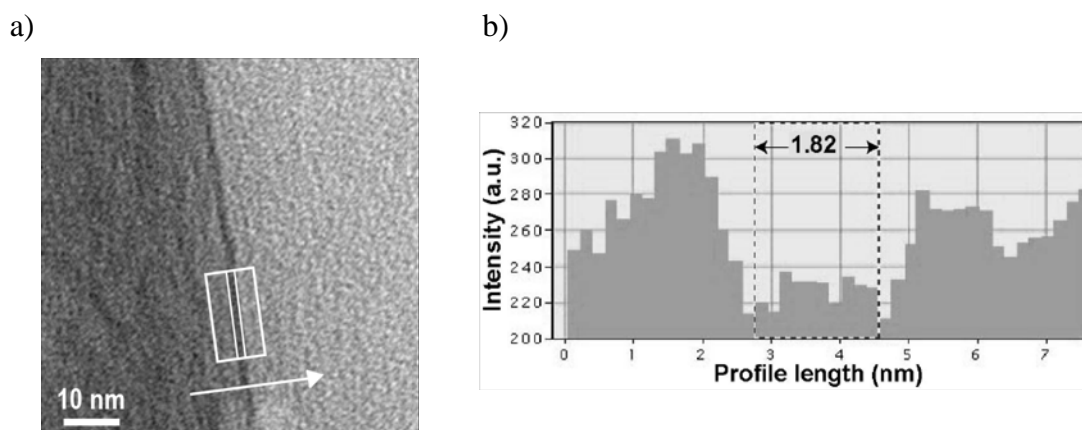


Fig. 3.8 Determination of the thickness of the thin layer attributed to the PF3 coating. The intensity profile reported in (b) is established across the region of the layer marked by the white frame in (a).

**Grazing incidence X-ray reflectivity.** In order to confirm the PF3 layer thickness defined by TEM measurements, grazing incidence X-ray reflectivity measurements were performed. GIXR probes the electronic density profile perpendicular to the surface. This profile is normally modeled in terms of density, thickness, and roughness parameters of a multi-slice structure. The quality of GIXR measurements depend strongly on the substrate flatness and the contrast of the electron densities of substrate and coatings. The perfluorinated silane coating deposited on a silicon wafer (S) covered by a thermally grown SiO<sub>2</sub> layer of ~ 50- nm thickness (RMS roughness 0.2 nm), was analyzed, and compared to the thickness



measured of the PF3 layer deposited on a GaAs substrate (G), covered by a SiO<sub>2</sub> layer of ~ 10-nm thickness, obtained by plasma-enhanced chemical vapor deposition (PECVD) (RMS roughness 0.75 nm). The presence of the organic layer could be confirmed on both S and G substrates. The X-ray reflectivity curves are given in Fig. 3.9 (thicker lines), together with their simulations (thinner lines).

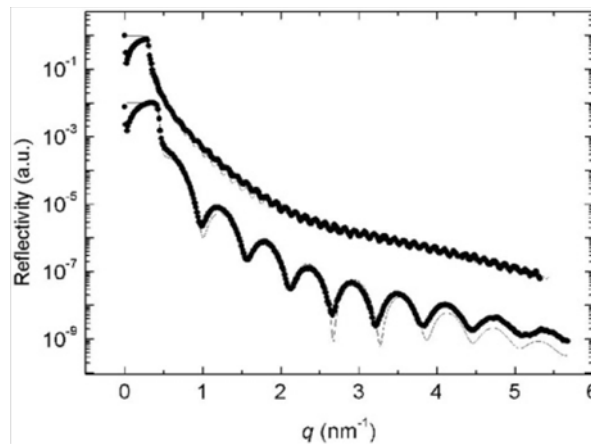


Fig. 3.9 GIXR curves of the perfluorosilane layer deposited on a thermally oxidized silicon wafer (SiO<sub>2</sub> layer ~ 50- nm thick) - lower curve (sample S)-, and on a ~ 10-nm thick PECVD deposited SiO<sub>2</sub> layer on a GaAs substrate - upper curve (sample G). Thick lines represent experimental values, and thin line represent simulations.

The thicknesses derived from simulations are 1.3 nm and 1.6 nm for S and G, respectively, and result in acceptable agreement with the estimations obtained by TEM observations. The densities determinations provided 1.2 and 1.3 g/cm<sup>3</sup> as the best values for sample S and G, respectively. Despite the excellent resolution in real and reciprocal space obtained using synchrotron X-rays, a partial degradation of the organic layer probably occurred with X-ray exposure, as it is documented by previous literature [46].

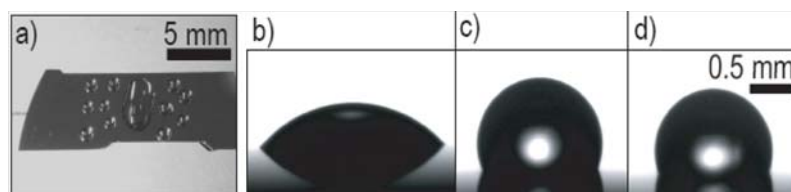


Fig. 3.10 Wetting study on perfluorosilvanized SiO<sub>2</sub>-coated GaAs. a) Behavior of water drops after synchrotron X-rays irradiation. b) Contact angle on the irradiated zone. c) Contact angle on a side of the irradiated zone. d) Contact angle before any irradiation.

Water static contact angle measurements performed on the sample regions that were exposed to the synchrotron X-rays showed a significant decrease, indicating that the organic layer was damaged by x-ray irradiation (Fig. 3.10).

From these TEM and GIXR results one can conclude that the optimized and controlled silanization process deposited about a monolayer of the trifunctional perfluorinated silane.

#### ***Determination of the coating roughness***

The roughness of the coating was measured by AFM. High roughness can be found if some reaction parameters are not controlled, especially the presence of water. The RMS roughness of the naturally oxidized silicon wafer and of a silanized wafer was the same (i.e. 0.7 nm), within the error affecting AFM measurements. The RMS roughness of the silica substrate in the original state (1.2 nm) was higher than after the silanization process (RMS 0.3 nm). This difference can be attributed to the fact that the silane molecules forming the layer are not all bonded directly to the substrate, since the surface density of -OH groups at the silica surface ( $\sim 4.6$  -OH groups/nm<sup>2</sup>) is higher than the maximum density of densely packed perfluoroalkylchains (being the perfluorinated chain cross-section in densely packed layers  $\sim 0.25$  nm<sup>2</sup>). The film homogeneity is however guaranteed by the lateral cross-polymerization. An AFM image of the silanized glass disc substrate is shown in Fig. 3.11. The topographic clustered character of the analyzed surface is due to the silica substrate.

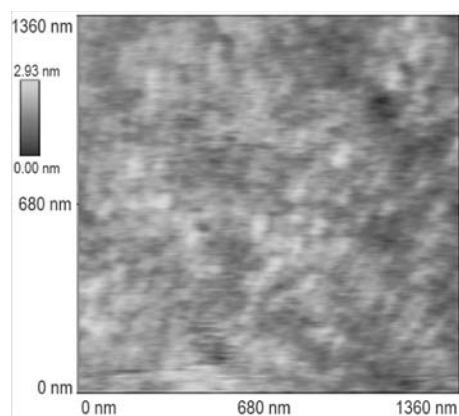


Fig. 3.11 Contact mode AFM image of the silanized silica surface (initial RMS roughness  $\sim 1.2$  nm; final RMS roughness  $\sim 0.3$  nm). The underlying characteristic clustered appearance of the silica surface is still visible.

### Critical surface energy and chemical composition

Static contact angle measurements performed with liquids having different chemical and physical properties proved the general high liquid-repellency of the developed coating (see Fig. 3.12).

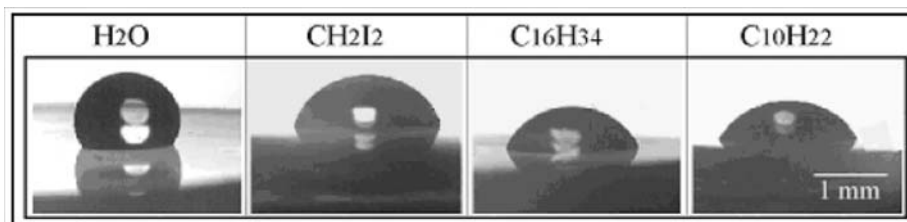


Fig. 3.12 Static contact angle images of different liquids on the PF3 coated silica substrate (silanization performed under optimized conditions). H<sub>2</sub>O: 123°; CH<sub>2</sub>I<sub>2</sub>: 78°; C<sub>16</sub>H<sub>34</sub>: 60°; C<sub>10</sub>H<sub>22</sub>: 50°.

The coating is not only very hydrophobic but also only partially wetted by alkanes. This oil-repellent character leads to a very low critical surface energy, which can be determined by Zisman's method using five *n*-alkanes (see Fig. 3.13).

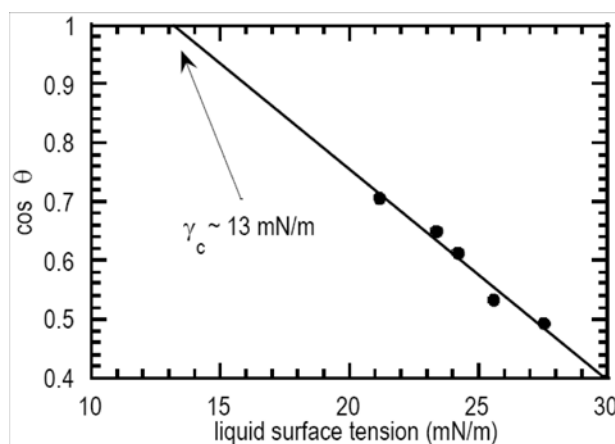


Fig. 3.13 Zisman's plot of the PF3 coating, obtained by static contact angle measurements with five different *n*-alkanes. They are: C<sub>8</sub>H<sub>18</sub>: 45°; C<sub>10</sub>H<sub>22</sub>: 49°; C<sub>11</sub>H<sub>24</sub>: 52°; C<sub>12</sub>H<sub>26</sub>: 58°; C<sub>16</sub>H<sub>34</sub>: 60°. The value of the critical surface energy extrapolated at  $\cos \theta = 1$  is 13 mN/m.

The obtained  $\gamma_c$  value was as low as 13 mN/m. This value is intermediate between the characteristic value of -CF<sub>2</sub>-CF<sub>2</sub>- polytetrafluoroethylene polymer surfaces (i.e. 18 mN/m), and the value of densely packed -(CF<sub>2</sub>)<sub>n</sub>-CF<sub>3</sub> end group [59][184] (i.e. 6 mN/m).

XPS analyses permitted the comparison of three PF3 coatings presenting different water contact angles (123°, 117°, and 96°), because deposited in different conditions of N<sub>2</sub> gas flow

and silane temperature. Each of the three considered samples was analyzed at two different take-off angles, varying the sensitivity depth of the chemical analysis. At take-off angle of 20°, XPS analysis is especially sensitive to the most upper molecular layer, whereas at take-off angle of 90° the information comes from a thicker layer, but still smaller than 5 nm.

XPS	% at. conc. for $\theta = 123^\circ$		% at. conc. for $\theta = 123^\circ$		% at. conc. for $\theta = 123^\circ$	
	90°	20°	90°	20°	90°	20°
<b>F 1s</b>	28	31	24	29	18	21
<b>C 1s</b>	14	30	18	31	14	28
<b>Si 2p</b>	18	18	19	18	21	24
<b>O 1s</b>	40	21	39	22	47	27
<b>F/C</b>	2.0	1.0	1.3	0.9	1.3	0.7

Table 3.1 XPS data of three silica samples presenting different water repellency

The obtained results (reported in Table 1) show that the sample with the highest static contact angle also presents the highest F atomic concentration. Considering individually each sample, and the two analyses at different take-off angle, it results that an increase in F concentration is always associated with an increase in surface sensitivity (i.e. lower take-off angle), and with a decrease in F/C ratio. This fact confirms that the hydrocarbon contaminations possibly adsorbed are on the sample surface, and comparing the three samples allows to conclude that the most repellent coating ( $\theta = 123^\circ$ ) presents the lowest contaminant concentration, since its F/C ratio is the highest for both the different surface sensitivities.

In Fig. 3.14, the C 1s peak is observed at high magnification, in order to identify the contributions originated by different chemical groups.

The order of water repellency is coherent with the concentration of the fluorinated carbon species. The variation of the ratio between the signal of the -CF<sub>2</sub>- backbone and that of the CF<sub>3</sub>- terminal group (CF<sub>2</sub>/CF<sub>3</sub> ratio), permits the assumption that denser layers present higher concentrations of vertically upright perfluorocarbon chains.

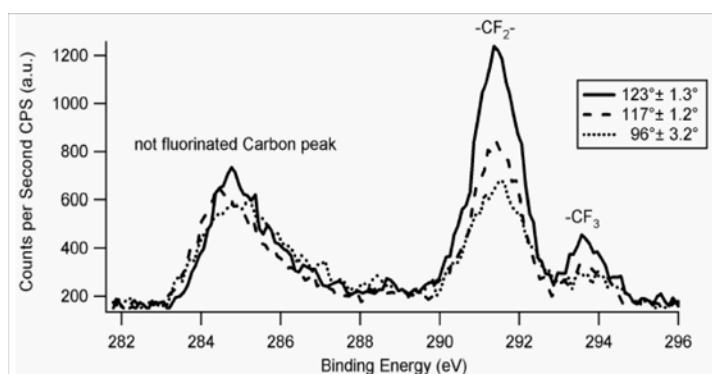


Fig. 3.14 C 1s XPS high resolution spectra of three samples, presenting different static water contact angle (123°, 117°, 96° respectively), analyzed at 20° take-off angle.

### Durability test

The resistance to the external environment and the durability of PF3 coatings are particularly interesting for their potential applications. A high chemical resistance is expected, since the bonds between the molecule and the substrate are covalent and symmetric [Si-O-Si]. A standard weathering test was performed in a commercial climatic cabinet, where a one-month aging cycle simulates one year of outdoor exposition. The samples were continuously irradiated with artificial sunlight, and the relative humidity and temperature were varied between 15 and 70% and -15° and +50°C, respectively.

Water and *n*-hexadecane contact angle values for three different samples, measured before and after the aging cycle in the commercial climatic cabinet, are reported in Fig. 3.15.

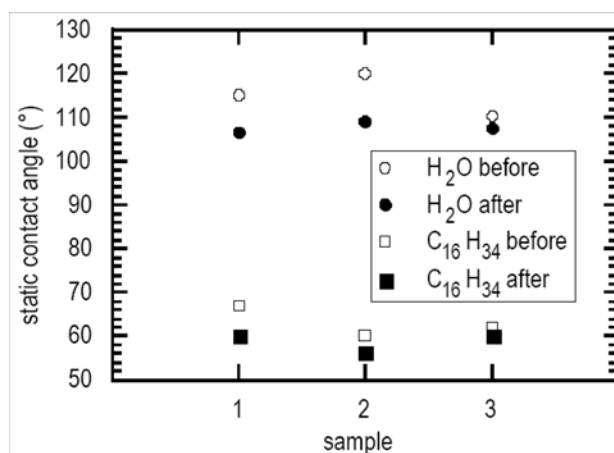


Fig. 3.15 Water and *n*-hexadecane static contact angles for three different coated silica substrates. The reported values are measured before and after one-month aging cycle in a climatic cabinet that simulates one year of outdoor exposition.

Water contact angles values decreased by maximum  $10^\circ$  after the weathering test. It is possible to conclude that the perfluorinated silane layer did not significantly suffer from temperature and humidity changes, and from UV exposure, presumably because it is linked at the substrate by strong covalent bonds.

## 3.5 Conclusions

This chapter presented the method developed for depositing hydrophobic molecular coatings on silicon oxide substrates, in a controlled and reproducible way, by a gas-flow apparatus, using perfluorodecyltrichlorosilane molecules.

The value of  $123^\circ$  measured for water contact angle on a perfluorosilanized silica substrate is similar to that found in literature for densely packed perfluorinated chains. However, the contribution of the initial substrate roughness to the very low critical surface energy of  $13\text{mN/m}$  (estimated by the Zisman plot) cannot be completely excluded, and no experimental evidence exists that permits its quantification.

It was shown that the complete surface hydration is a fundamental aspect to ensure the success of the silane molecules grafting process. The described apparatus permitted to investigate the influence of each individual silanization process parameter on the water contact angle. The only parameter that showed a strong influence is the temperature at which the silane reservoir is kept, since it directly influences the number of silane molecules reaching the substrate per time unit.

TEM imaging was used to measure the silane coating thickness. Resulting in the order of a molecule length, the TEM estimated thickness suggested that the coating is presumably constituted by a monolayer of trifunctional silane molecules, and GIXR confirmed this result.

The realized coating was also proved to be aging resistant.

The developed coating presents all the properties necessary to be systematically applied on all the structured silicon substrates used in this thesis work, in order to make them all comparable in their hydrophobicity, due to their new perfluorocarbon based surface chemical composition. As emphasized in Chapter 1, the hydrophobic chemical composition is, with the surface roughness, one of the two fundamental requirements for having superhydrophobic solid surfaces.

---

## 4 Superhydrophobicity: Static contact angle investigations

*In this chapter, the results of water static contact angle investigations on structured hydrophobic surfaces consisting of perfluorosilanized periodical distribution of flat-top obstacles are presented as a function of different roughness geometrical parameters. The chapter begins presenting the simple thermodynamic model developed to predict the transition between the composite-Cassie regime and the wetted-Wenzel regime, observed varying each roughness parameter. Subsequently, all the experimental static contact angle results are described and their good agreement with the proposed model is discussed<sup>1</sup>.*

### 4.1 Theoretical background

The equation of Young, Wenzel, and Cassie can be derived by minimization of the free energy of the drop-substrate system under consideration at equilibrium with the following assumptions [46][49][70]: (i) the drop is hemispherical and its contact line is circular, (ii) it is large compared to roughness asperity size, (iii) the volume of liquid in the asperities is negligible with respect to the total liquid volume, (iv) gravity effects and line tension contribution are neglected, (v) the liquid-air interface below the drop is flat and at a constant height, (vi) the surfaces delimiting the main substrate roughness (i.e. top, lateral and bottom pillars surfaces) are considered atomically flat; and (vii) all molecular and microscopic interactions, especially at the level of the three-phase contact line, are ignored. Such a derivation will be presented below, adapted to the rough surface types considered in this work and the validity of the different assumptions will be discussed.

The system is composed of a volume  $V$  of water and a surface  $S_{\text{total}}$  of rough substrate.

The model surface consists of periodic distributions of identical flat-top obstacles, perfluorosilanized by the method described in Chapter 3. For the details on the adopted microstructuring process, see Appendix 1. The characteristic geometrical parameters of these surfaces are the following: pitch  $p$  (minimum distance between two consecutive obstacles),

1. A scientific article presenting the results discussed in this chapter has been accepted for publication on Langmuir, in December 2006.

disposition factor  $A$  (statistical number of obstacles per unit surface area  $p^2$ ), obstacle height  $h$ , obstacle top-surface area  $s$ , perimeter of the horizontal obstacle section  $L$ . The parameters  $p$  and  $A$  as defined here permit the description of all possible statistical regular obstacle distributions, and are directly correlated to the number of obstacles per surface area  $N$  (i.e. asperity surface density), by the relation  $N = A/p^2$ . The scanning electron microscope (SEM) and optical microscope images of a typical substrate are shown in Fig. 4.1. In this work, millimeter drops on micrometer pillars are studied, therefore it can be assumed that the obstacles are small compared to the drop base surface, and that the water meniscus between obstacles is practically flat. A nanometer roughness on the side of the structured obstacles necessarily exists, due to the fabrication process, but it is neglected in this work.

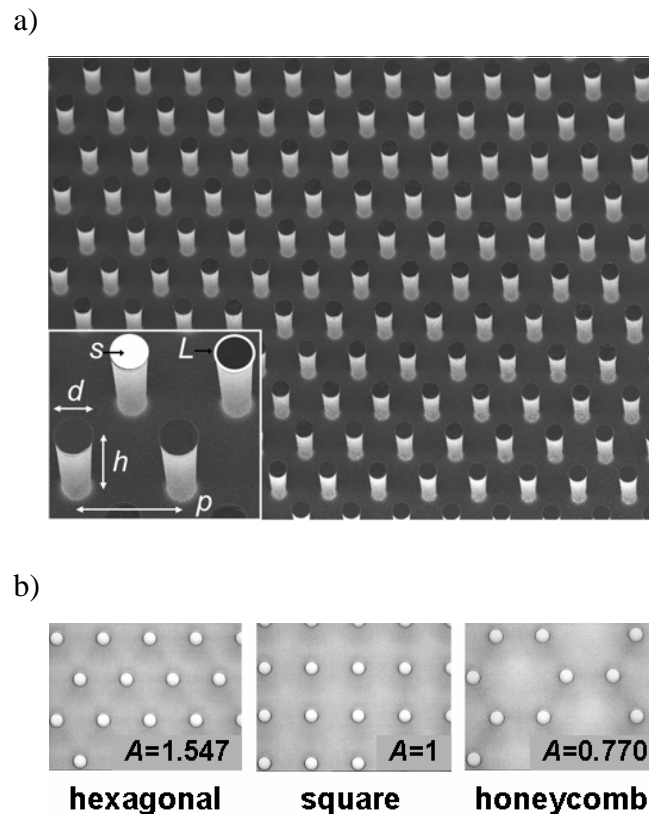


Fig. 4.1 *Model rough substrates.* a) SEM micrograph (tilt angle  $20^\circ$ ) of typical micro-structured Si surface showing the hexagonal arrangement of  $10\text{-}\mu\text{m}$  diameter cylindrical pillars ( $h = 40\ \mu\text{m}$ ,  $p = 30\ \mu\text{m}$ ). The main roughness parameters (diameter  $d$ , height  $h$ , pitch  $p$ , obstacle top-surface perimeter  $L$ , and area  $s$ ) are shown in the inset. b) Top view optical microscope images of three selected surface geometrical arrangements of cylindrical pillars (hexagonal, square, honeycomb). Obstacle disposition factors values  $A$  are also reported, corresponding to the statistical number of pillars per unit surface (i.e.  $p^2$ ).

On the basis of the assumptions above-described, the statistical parameters  $r$  and  $f$ , Wenzel and Cassie roughness factor respectively, can be expressed as



$$r = 1 + \frac{A}{p^2}hL \quad (4.1)$$

and

$$f = \frac{A}{p^2}s. \quad (4.2)$$

The free energy of the system should include an interfacial energy term, a potential energy term, and a line tension term [131], as proposed in literature [32]. The variation of the drop potential energy depending on the position of its mass center [132] is a weak term, which will not be considered in this work, as it only induces a variation of a few degrees in the contact angle estimation, especially if the drop is assumed to be hemispherical. The influence of the drop hemisphericity is a more critical aspect, and by estimation of the drop shape factor SF (for its definition see “Gravity effect” in Chapter 2), Chatterjee [123] showed that, especially for superhydrophobic surfaces (i.e. with contact angles up to  $170^\circ$ ), drops with volume less than  $0.15 \mu\text{L}$  should be used to induce an error due to gravity of less than  $1^\circ$ . Line tension was a very controversial concept for a long time, but recent measurements confirm theoretical predictions proving that its contribution is negligible [133]. Therefore, the free energy may be restricted to the sum of the interfacial energies, which is expressed as

$$E_{\text{surf}} = \gamma_{\text{LV}}S_{\text{LV}} + \gamma_{\text{SV}}S_{\text{SV}} + \gamma_{\text{LS}}S_{\text{LS}} \quad (4.3)$$

where  $\gamma_{ij}$  are the interfacial energies between  $i$  and  $j$ ,  $S_{ij}$  are the corresponding interfaces between the phases L, V and S, for liquid, vapor, and solid, respectively. Introducing  $S_{\text{ext}}$  (the external drop surface),  $S_{\text{base}}$  (the geometric drop base surface),  $S_{\text{total}}$  (the total solid sample surface),  $x$  (the penetration depth of water in the asperities), and  $y$  (the ratio of the true interface vapor-liquid meniscus in the asperities to the horizontal section) - see Fig. 4.2 -, the surface energy is respectively:

- in a *composite* regime

$$\begin{aligned} E_{\text{surf}}(\text{composite}) &= \gamma_{\text{LV}}[S_{\text{ext}} + (1-f)yS_{\text{base}}] + \gamma_{\text{LS}}\left(fS_{\text{base}} + x\frac{A}{p^2}LS_{\text{base}}\right) \\ &+ \gamma_{\text{SV}}\left[r(S_{\text{total}} - S_{\text{base}}) + (1-f)S_{\text{base}} + \frac{A}{p^2}LS_{\text{base}}(h-x)\right] \\ &= \gamma_{\text{LV}}S_{\text{ext}} + C_{\text{comp}}S_{\text{base}} + \gamma_{\text{SV}}rS_{\text{total}} \end{aligned} \quad (4.4)$$

$$\text{with } C_{\text{comp}} = -\gamma_{\text{LV}}\left[f\left(1 + \frac{Lx}{s}\right)\cos\theta_{\text{flat}} + (f-1)y\right]; \quad (4.5)$$

- in a *wetted* regime

$$\begin{aligned}
 E_{\text{surf}}(\text{wetted}) &= \gamma_{LV}S_{\text{ext}} + \gamma_{LS}rS_{\text{base}} + \gamma_{SV}r(S_{\text{total}} - S_{\text{base}}) \\
 &+ \gamma_{SV}\left[r(S_{\text{total}} - S_{\text{base}}) + (1-f)S_{\text{base}} + \frac{A}{p^2}LS_{\text{base}}(h-x)\right] \\
 &= \gamma_{LV}S_{\text{ext}} + C_{\text{wet}}S_{\text{base}} + \gamma_{SV}rS_{\text{tot}}
 \end{aligned} \tag{4.6}$$

with  $C_{\text{wet}} = -\gamma_{LV}r\cos\theta_{\text{flat}}$  (4.7)

and  $\cos\theta_{\text{flat}}$  given by Young's equation.

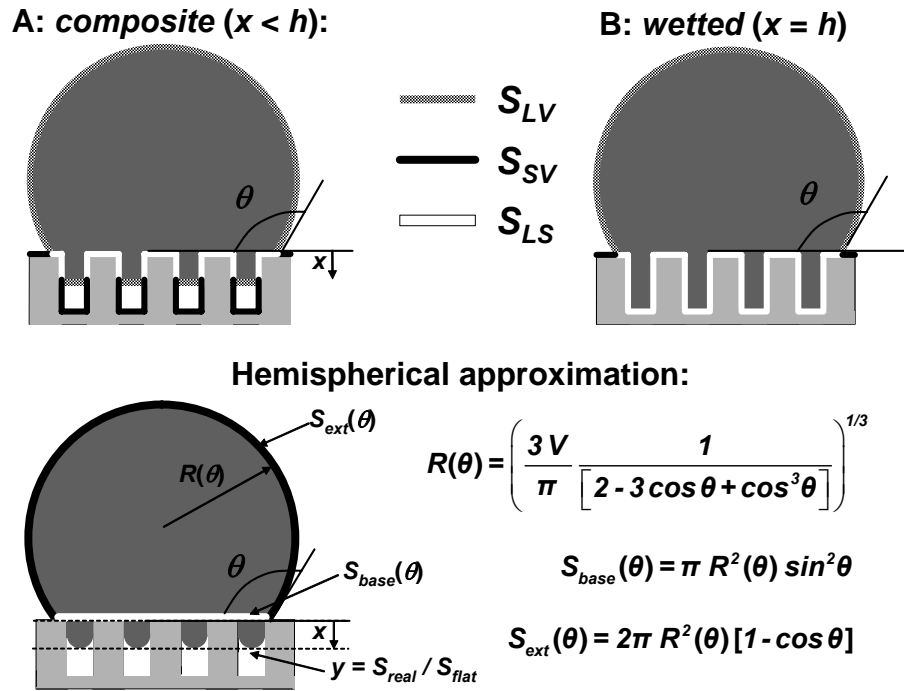


Fig. 4.2 *Surface energy minimization.* Top images: different interfaces (liquid-vapor, solid-vapor, liquid-solid) are highlighted, both for the *composite* and *wetted* case. Bottom image: notations and formulae used in the hemispherical drop approximation are reported.

Consequently, the general free energy can be expressed as a function of the measured contact angle  $\theta$  by the following equation

$$\begin{aligned}
 E_{\text{surf}}(\theta, x, y) &= \pi \left(\frac{3V}{\pi}\right)^{(2/3)} \frac{1}{(2 - 3\cos\theta + (\cos\theta)^3)^{(2/3)}} \\
 &[2\gamma_{LV}(1 - \cos\theta) + C(x, y)(\sin\theta)^2] + \gamma_{LV}rS_{\text{total}}
 \end{aligned} \tag{4.8}$$

where  $C(x, y)$  is either  $C_{\text{comp}}$  or  $C_{\text{wet}}$ , and  $\cos\theta$  is in the range  $[-1, 1]$ .

Changing variable with  $X = \cos\theta$  and calculating the derivative of the function with respect to  $X$  gives

$$\frac{\partial E_{\text{surf}}}{\partial X}(X, x, y) = 2\pi \left(\frac{3V}{\pi}\right)^{2/3} \frac{[\gamma_{\text{LV}}X + C(x, y)](X+1)^2}{[(X-1)^2(X+2)]^{5/3}} \quad (4.9)$$

The sign of this expression is negative with increasing  $X$  until  $X = X_{\text{ext}} = \frac{-C(x, y)}{\gamma_{\text{LV}}}$  or  $X = -1$ , and then it becomes positive. Therefore, the function  $E_{\text{surf}}$  exhibits a minimum in  $\theta$  for  $\cos\theta = X_{\text{ext}}$  or  $\theta = \pi$ , and the lower  $\theta$ , the lower the surface energy. The solutions for  $\cos\theta = X_{\text{ext}}$  are presented below, but it should not be forgotten that when these solutions are not in the range  $[-1, 1]$ , the derivation also gives  $\theta = \pi$ , as limited cases in both *wetted* and *composite* regimes.

In the *composite* case, the minimum surface energy  $E_{\text{surf}}(\theta, x, y)$  is obtained for

$$\cos\theta_{\text{min}}^{\text{comp}} = f \left(1 + \frac{Lx}{s}\right) \cos\theta_{\text{flat}} - (1-f)y \quad (4.10)$$

This equation is a generalized Cassie's equation, with  $f$  from Eq. 4.2, expanded by the liquid penetration depth  $x$  and the curvature  $y$  of the penetrating liquid. Similar equations have already been derived [32][193] with different interpretations of the coefficients [34][46][90].

By increasing either  $x$  or  $y$ , the minimum *composite* contact angle  $\theta_{\text{min}}^{\text{comp}}$  increases, which shows that the minimum energy is obtained for  $x = 0, y = 1$ : partial filling of the roughness structure is thermodynamically less favorable, and does not take place, which agrees with experimental observations [20][52], although contradicts assumptions of other authors [44][55].

In the *wetted* case, the minimum surface energy  $E_{\text{surf}}(\theta, x, y)$  is obtained for

$$\cos\theta_{\text{min}}^{\text{wet}} = r \cos\theta_{\text{flat}} \quad (4.11)$$

which is Wenzel's equation, with  $r$  from Eq. 4.1.

The Cassie configuration corresponds to the lowest energy state in the *composite* case (Eq. 4.10), whereas the Wenzel configuration corresponds to the lowest energy state in the *wetted* case (Eq. 4.11). Therefore, two energy minima are obtained for the system, one for the *composite* case (Cassie), without a filling of the asperities (Fig. 4.2-a), and one for the *wetted* case (Wenzel), corresponding to a complete filling of the asperities (Fig. 4.2-b). The absolute interfacial energy minimum corresponds to the lower minimum contact angle of both.

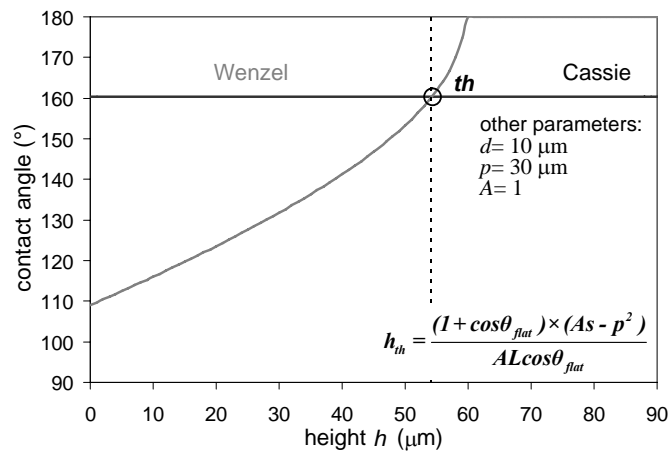
Therefore, a thermodynamic criterion that can be employed to define which of the two regimes is more favored can be derived by equating the Cassie and Wenzel contact angles [92]. Defining the contact angle on the flat surface that delimits the two regimes on a rough surfaces, the equation thus obtained

$$\cos\theta_{\text{flat}} = \frac{1-f}{f-r} \quad (4.12)$$

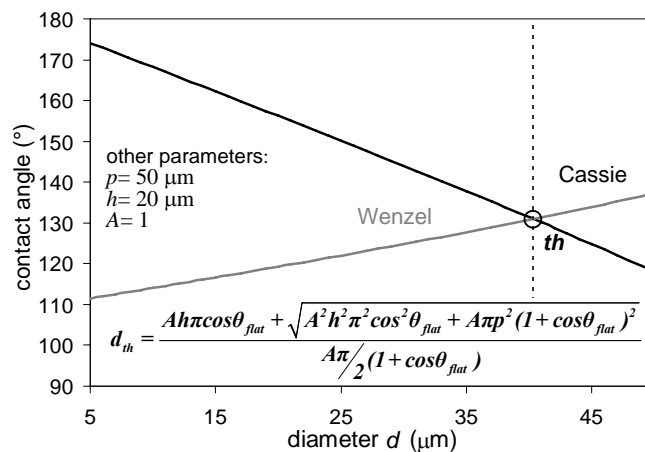
expresses the condition for which the energy for both Cassie and Wenzel states are equal, and it therefore enables to calculate the point where the thermodynamic transition between the *wetted* and *composite* regime occurs. For instance, the Cassie state is thermodynamically favored if  $\cos\theta_{\text{comp}} > \cos\theta_{\text{wet}}$ , that is, when  $\cos\theta_{\text{flat}} < (1-f)/(f-r)$ .

Examples of the theoretical evolution of the contact angle as a function of one geometrical parameter, keeping the others constant, are shown in Fig. 4.3 and Fig. 4.4-A for both the Cassie and Wenzel models.

a)



b)



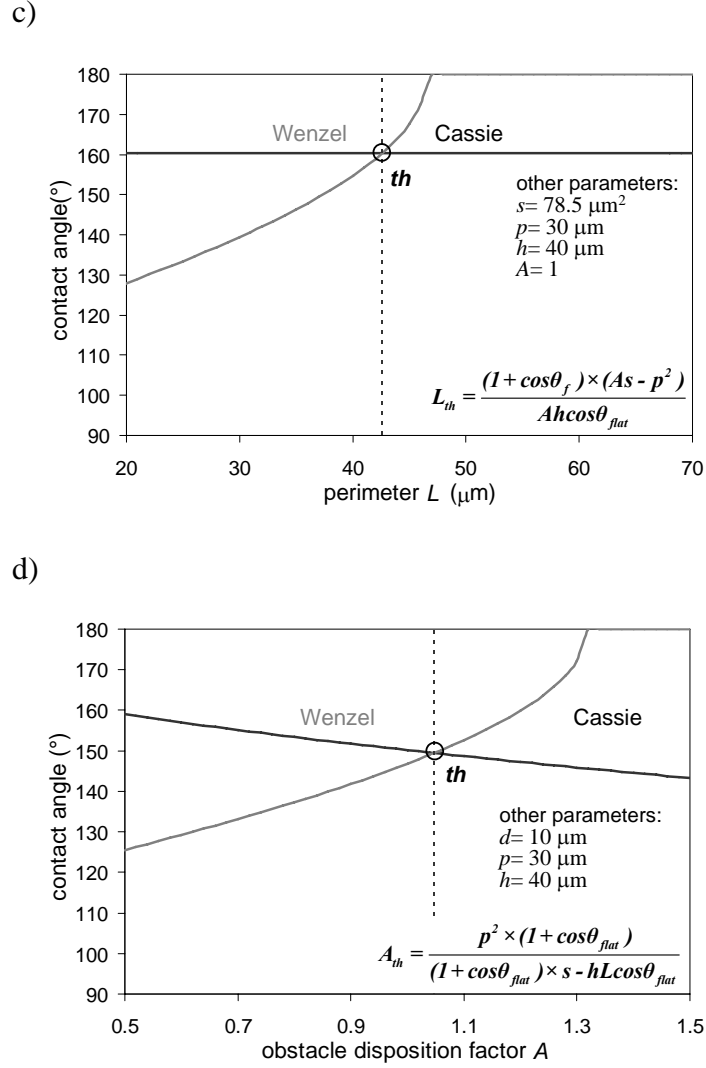


Fig. 4.3 *Influence of different geometrical roughness parameters.* Cassie (black) and Wenzel (gray) theoretical curves as a function of each roughness parameters: a), b), and c) correspond to square arrangements of cylindrical flat-top pillars as a function of pillar height ( $h$ ), diameter ( $d$ ), and perimeter ( $L$ ) of the top-surface, respectively; d) corresponds to the obstacle disposition factor ( $A$ ) influence on Wenzel and Cassie angles. The formula giving the parameter value of the thermodynamic transition point  $th$  is reported in each graph.

All parameters were chosen to fit the realized experiments, with a constant static contact angle on the flat substrate  $\theta_{flat} = 110^\circ$ . Smaller contact angles in the Cassie state, i.e. smaller total energy states, are obtained for smaller values of the variables diameter ( $d$ ), disposition factor ( $A$ ), and pitch ( $p$ ), until the crossing to the Wenzel curve appears (see Fig. 4.3-b, d, and Fig. 4.4-A, respectively). In contrast, for smaller values of the variable height ( $h$ ) and perimeter ( $L$ ), the Wenzel curve corresponds to smaller contact angles (see Fig. 4.3-a, and c). The intersection of the lines, corresponding to the value where both states are energetically equal, is evidenced in each graph by  $th$ , and the related mathematical expression (from Eq. 4.12) is also reported.

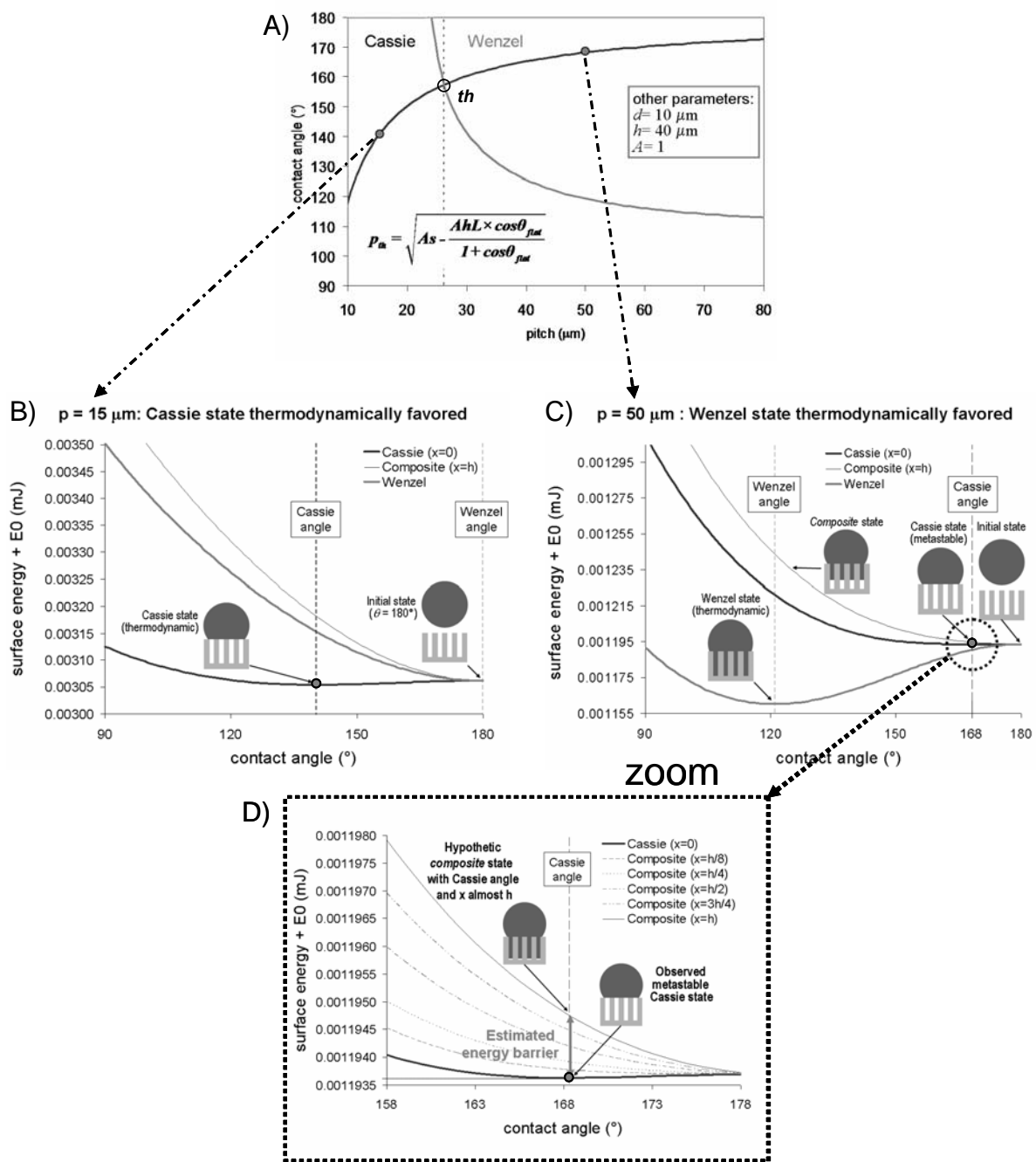


Fig. 4.4 *Thermodynamic study of composite and wetted energy states as a function of pitch.* Image A shows the calculated Cassie and Wenzel contact angle curves as a function of pitch, for square distributions of flat-top cylindrical pillars, and the thermodynamic intersection *th* between the two regimes is also indicated. B and C show energy calculations, B for a pitch of 15 μm, where Cassie is the energy minimum state, and C with a pitch of 50 μm, where Wenzel is the energy minimum state. D is a “zoom” of the “Cassie angle” region delimited by the dashed circle in C. Graphical representations of the liquid drop states on the structured surfaces are linked by a flash to the corresponding points in the graphs. Energy calculations are carried out for a 3-μL drop, on a circular substrate area of 3-mm radius.

However, as already mentioned in the introduction, experience shows that drops gently deposited on rough surfaces do not always assume the *wetted* configuration, even when this represents the absolute minimum energy. This is easily understandable from a thermodynamic perspective, as explained for one example in Fig. 4.4. This figure presents in A the contact angle curves as a function of pillar distance (pitch), keeping all other parameters constant; and in B and C (and D) the energy curves are given as a function of contact angles for two different pitch values, falling respectively into the “Cassie” thermodynamic region for B, and into the “Wenzel” thermodynamic regions for C (and D), calculated using Eq. 4.10 (with  $y = 1$ , varying  $x$ ) and Eq. 4.11. The surface energies presented in Fig. 4.4-B, C and D correspond to a “drop-substrate” system consisting of a water drop of  $\sim 3\text{-}\mu\text{L}$  volume deposited on a circular area of 3-mm radius of a perfluorinated silicon microstructured substrate. The related interfacial energies values are  $\gamma_{LV} = 72 \times 10^{-12} \text{ mJ}/\mu\text{m}^2$ ,  $\gamma_{SV} = 13 \times 10^{-12} \text{ mJ}/\mu\text{m}^2$  (i.e. the critical surface energy of the developed perfluorosilane coating estimated by the Zisman plot -see Chapter 3-), and  $\gamma_{SV} = 37.6 \times 10^{-12} \text{ mJ}/\mu\text{m}^2$  (derived by Young’s equation with  $\theta_{\text{flat}} = 110^\circ$ ). The above precised values are those considered in all the thermodynamic analyses presented in this work for water contact angle investigations.

With the fixed geometrical roughness parameters, from Fig. 4.4-A the isoenergetic pitch would be  $\sim 26 \mu\text{m}$ , with a contact angle of  $157^\circ$  (solution of Eq. 4.12). Smaller pitch values, i.e.  $15 \mu\text{m}$  as presented in Fig. 4.4-B, results in an energy difference of about 100 nJ between the favored Cassie *composite* state and the corresponding *wetted* state, for the reference drop of 3- $\mu\text{L}$  volume.

When Wenzel is the thermodynamically favored state, like for example at 50- $\mu\text{m}$  pitch (see Fig. 4.4-C), the energy curves show that, from the initial spherical drop in air to the smoothly deposited drop on the substrate (right part of Fig. 4.4-C), the system can easily enter into the metastable *composite* state shown in the zoom in Fig. 4.4-D, and associated with a local energy minimum. Moving from this state to the thermodynamic favored Wenzel state requires that an energy barrier is overcome, due to the filling of the asperities with water (see Fig. 4.4-C and D). A transition energy barrier of about 1.5 nJ between the Cassie and Wenzel state is obtained for the reference 3- $\mu\text{L}$  drop by calculating the energy required to fully fill the asperities, assuming that the contact angle (here the Cassie contact angle corresponding to the metastable lowest energy state) remains constant in this transformation [51] (see Fig 4.4-D).

Using Eq. 4.8 to evaluate the surface energy  $E_{\text{surf}}^{\text{comp}}$ , the barrier energy can be estimated by the expression

$$\Delta E_{\text{surf}}^{\text{comp}} = E_{\text{surf}}^{\text{comp}}(\theta_{\text{comp}}, x = h) - E_{\text{surf}}^{\text{comp}}(\theta_{\text{comp}}, x = 0) \quad (4.13)$$

As the variations of surfaces we are dealing with are extremely small, it is convenient to correct for the liquid volume in the asperities for this energy calculation. The corrected drop radius  $R(\theta, x)$  is found solving the 3<sup>rd</sup> polynomial equation

$$\frac{\pi}{3}(2 - 3 \cos \theta + (\cos \theta)^3)R(\theta, x)^3 + (1 - f)\pi(\sin \theta)^2 x - V = 0 \quad (4.14)$$

and the corrected volume can be introduced in Eq. 4.8.

## 4.2 Measuring static contact angles

In this work, all contact angle measurements have been performed by the sessile drop method in a Digidrop apparatus (GBX, Romans-sur-Isère, France), under a controlled atmosphere of water vapor almost saturated of  $N_2$  (relative humidity  $\sim 90\%$ ), at controlled room temperature ( $23^\circ\text{C} \pm 1^\circ\text{C}$ ). Puriss. p.a. water (Fluka, Switzerland) was used as probe liquid. For static contact angle measurements, water drops are formed at the tip of homemade perfluorosilanized glass capillaries. They detach from the tip, and fall onto the substrate, when they reach a precise volume comprised between  $2.5 \mu\text{L}$  to  $6 \mu\text{L}$ , depending on the tip size. Different capillaries (i.e. different drop sizes) were used especially on samples with structures around the metastable to stable Cassie-Wenzel transition. The distance of the specific capillary from the substrate was kept constant and at a value as to minimize the kinetic energy of the falling drop. Digitized images of the drop-substrate system were recorded when the drop external surface stopped to vibrate (i.e.  $\sim 3$ -5 seconds after the drop-substrate contact occurred, depending on the drop size). Each reported static contact angle value is obtained averaging at least six measurements, corresponding to the left and right angles of three drops deposited at different spots on the same substrate. Static contact angle estimations were performed by a computer program for drop shape analysis method based on the Laplace equation [126][128][129]. All the reported static contact angle measurements are within  $\pm 3^\circ$  of the averages.



### 4.3 Static contact angle results

“SCA” hereafter designates “static contact angle”.

#### Influence of $p$ , spacing between consecutive pillars

Fig. 4.5 presents the results of water SCA measurements performed as a function of the spacing between consecutive pillars (pitch  $p = 15 \mu\text{m}$  to  $150 \mu\text{m}$ ), for cylindrical pillars ( $d = 10 \mu\text{m}$  and  $h = 40 \mu\text{m}$ ) in a square arrangement ( $A = 1$ ).

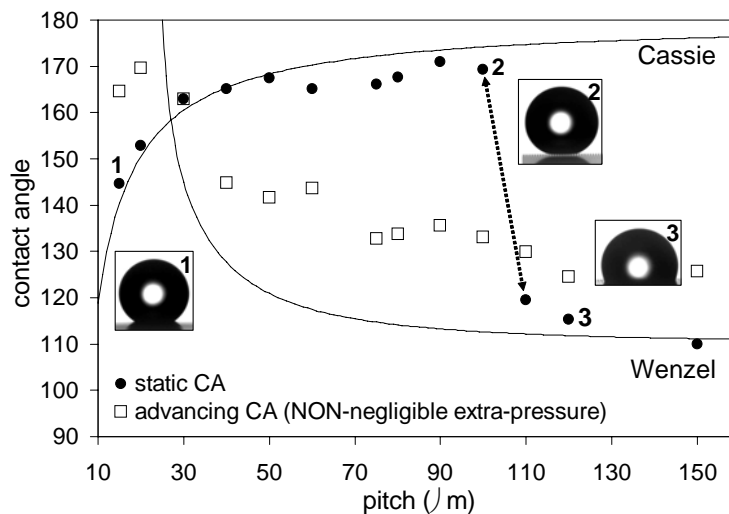


Fig. 4.5 *Pitch influence on SCAs.* Water SCAs values of  $\sim 3\text{-}\mu\text{L}$  drops softly deposited on the microstructured surfaces as a function of pitch, for square distribution ( $A = 1$ ) of cylindrical pillars ( $d = 10 \mu\text{m}$ ,  $h = 40 \mu\text{m}$ ). Cassie and Wenzel theoretical curves are also reported. Cassie-Wenzel transition position is indicated by the dashed double arrow. ( $\square$ ) Advancing contact angle values measured exerting a NON-negligible extra-pressure on the drop-substrate system<sup>1</sup>.

The reported SCA values (full dots) are in good agreement with the Cassie and the Wenzel models. With increasing pitch, a sharp transition from the Cassie to the Wenzel regime appears when passing from  $p = 100 \mu\text{m}$  to  $p = 110 \mu\text{m}$ , for drops deposited softly on the surface. The sharpness of the transition clearly shows that no state with partial filling of the asperities with water is observed, but only the extreme cases of the Cassie ( $x = 0$ ) or Wenzel regime ( $x = h$ ) are possible. When pushing the drop into the structures keeping the needle close to the substrate (i.e. exerting a NON-negligible extra-pressure on the drop-substrate system), dynamic contact angle measurements (in Fig. 4.5 open squares represent advancing contact angles) show the Cassie-Wenzel transition for  $p \sim 30 \mu\text{m}$ , which corresponds to the thermodynamic transition, given theoretically by the intersection of Cassie and Wenzel curves<sup>1</sup>. Therefore, the *composite*

states observed after soft deposition of the drop on the substrate for  $30 \mu\text{m} < p < 100 \mu\text{m}$  are metastable *composite* states, corresponding to the theoretical situation depicted in Fig. 4.4 (C and D). To predict the limit of stability of these *composite* states, the energy barrier from the Cassie state to the Wenzel state was calculated considering a complete filling of the asperities [51], according to Equation 4.13. This thermodynamic analysis is reported in Fig. 4.6.

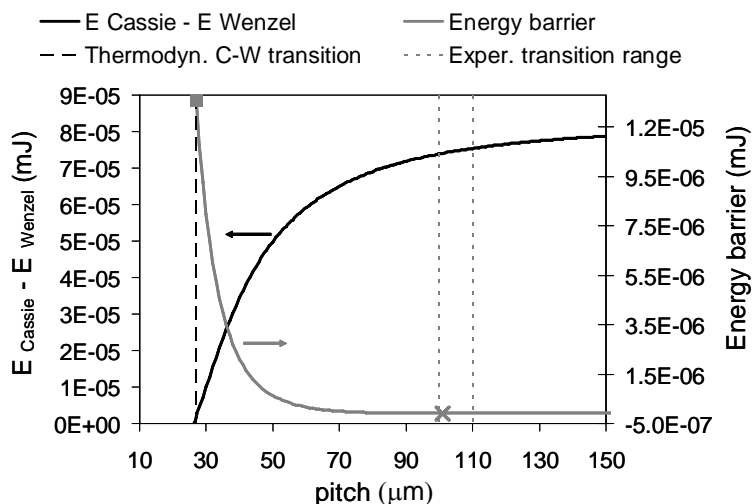


Fig. 4.6 *Pitch influence on system thermodynamic energy.* Black line (left scale) represents the energy difference between Cassie and Wenzel states as a function of pitch, and gray line (right scale) represents the energy barrier to fill the asperities, keeping the Cassie angle constant, in the range where the Cassie regime is metastable (Eq. 4.13). Symbol (■) represents the energy barrier at Cassie-Wenzel equal energy point. The lowest energy barrier, marked with (X), falls in the range where the experimental transition occurs.

While the difference between the free energy of the Cassie and Wenzel states (black curve referred to the left axis, and calculated by Eq. 4.8, 4.7, and 4.5) increases with increasing the pitch, the estimation of the energy barrier that a drop in the metastable *composite* regime has to overcome in order to reach the thermodynamically favored *wetted* state (gray curve referred to the right axis, and calculated by Eq. 4.13) decreases with increasing  $p$ , from  $1.26 \times 10^{-5}$  mJ at the equal energy state, to even negative values at the experimental transition, and presents a

1. As it will be shown and discussed in Chapters 6, at  $p = 30 \mu\text{m}$  there is a large discrepancy between the contact angle hysteresis values measured applying a “negligible” or a “NON-negligible” extra-pressure on the drop-substrate system. In the case of a “negligible” extra-pressure, the Cassie-Wenzel transition falls practically in the same range of the static one, and the corresponding hysteresis is very low, whereas with a “NON-negligible” extra-pressure hysteresis passes from values in the order of  $20^\circ$  for  $p = 20 \mu\text{m}$ , to a value as large as  $120^\circ$  for  $p = 30 \mu\text{m}$ . The corresponding very low receding angle confirms the complete liquid penetration among the asperities. This proves the *wetted* regime for the drops formed on the samples with  $p \geq 30 \mu\text{m}$ , and the *composite* regime for smaller pitches, and consequently the Cassie-Wenzel transition localized at the Cassie-Wenzel curves intersection (i.e. the thermodynamic equal energy point).

minimum marked with **X** for  $p = 99 \mu\text{m}$ . The precision of the calculated values should not be over-interpreted, in view of the large number of assumptions used, especially the neglecting of gravity, both in terms of drop distortion from a hemispherical cap and of potential energy. However, qualitatively, the graph shows that the stability of the metastable regime decreases with increasing pitch, and in particular, the experimental transition belongs to a pitch range (delimited by the two vertical dashed lines) in agreement with the minimum value position of the energy barrier curve.

In the literature, it has been proposed that the transition occurs when the gravitational energy compensates the energy barrier [51][194]: the author would rather think that the gravitational energy should be taken into account in the calculation of free energy and contact angle, and that the transition occurs when the drop vibration energy at the moment of the drop-substrate contact balances the energy barrier. For comparison, an energy barrier of  $1 \times 10^{-5}$  mJ corresponds to the kinetic energy of a 3- $\mu\text{L}$  water drop falling freely from 340  $\mu\text{m}$ , whereas an energy barrier of  $1 \times 10^{-7}$  mJ is balanced by the kinetic energy of the same drop falling from 3.4  $\mu\text{m}$ . Although this aspect is still under investigation, it can be already affirmed that a first estimation of the energy associated with the performed SCA measurements appears in agreement with the order of magnitude of  $10^{-7}$  mJ. Such an observation is based on the assumption that any contact angle investigation is inevitably associated with an even though small, but always present energy, for instance perceivable in the drop vibrations.

A water drop size effect on the transition from the metastable *composite* state to the *wetted* state was not observed for drop volumes between 2.5  $\mu\text{l}$  and 10  $\mu\text{l}$  (see Fig. 4.7), contradicting published assumptions [44], but supporting recent experimental results [47].

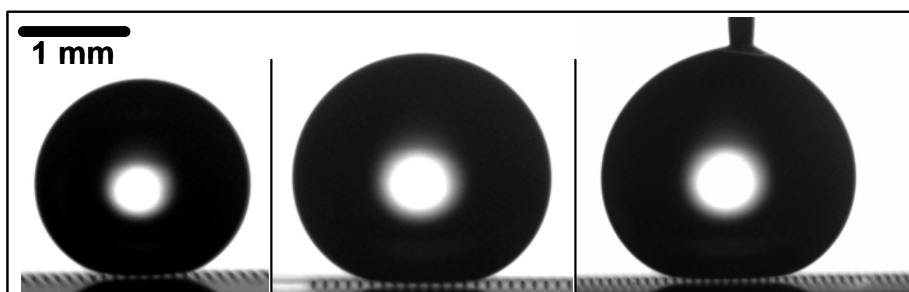


Fig. 4.7 Images of different volume drops ( $V = 3.5$ ,  $V = 5.5$  and  $V = 10.3 \mu\text{L}$ ) showing the stability of the *composite* metastable regime on the microstructured sample with  $p = 100 \mu\text{m}$ .

The flattening of big drops due to gravity changes the ratio  $S_{\text{base}}/S_{\text{ext}}$  with respect to the hemispherical drop, but maintains the drop in the *composite* regime, with high contact angle, even on the substrates showing the *composite* state that delimits the Cassie-Wenzel transition.

Fig. 4.8 shows water SCA measurements as a function of the pitch for the three defined geometrical arrangements: honeycomb “Hc” ( $A = 0.770$ ), square “Sq” ( $A = 1$ ) and hexagonal “Hex” ( $A = 1.547$ ).

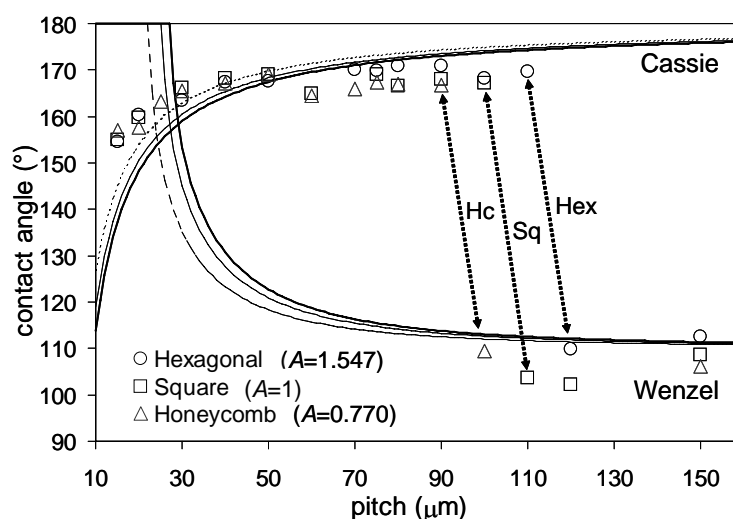


Fig. 4.8 *Geometrical disposition influence on SCAs.* Experimental SCAs measured on samples with three different geometrical arrangements (hexagonal,  $A = 1.547$ ; square,  $A = 1$ ; honeycomb,  $A = 0.770$ ) of cylindrical pillars ( $d = 10 \mu\text{m}$ ,  $h = 40 \mu\text{m}$ ) as a function of pitch for a water drop of  $\sim 3\text{-}\mu\text{L}$  volume are presented. The corresponding theoretical Cassie and Wenzel curves are also reported (Hex: black line; Sq: gray line; Hc: dashed line). Arrows indicate the Cassie-Wenzel transition for the different dispositions.

The transitions from the Cassie to Wenzel regimes are observed at slightly different pitches: first, for the honeycomb arrangement between 90 and 100  $\mu\text{m}$ , then for the square arrangement between 100 and 110  $\mu\text{m}$ , and finally for the hexagonal arrangement between 110 and 120  $\mu\text{m}$ . The corresponding energy barrier between the metastable *composite* state and the thermodynamically favored *wetted* state (Eq. 4.13) is reported in Fig. 4.9 as a function of the pitch, for the three disposition factors  $A$  under consideration, together with the observed experimental range for the transition. The experimental transitions are observed in the pitch order predicted by thermodynamics calculations, being the minima of the three energy barrier curves all in the region of the experimental transition range.

Presentation of these results as a function of the asperity surface density  $N$  (i.e.  $N = A/p^2$ ) (as it reported in Fig. 4.10) reveals that the different Cassie-Wenzel transitions evidenced in Fig. 4.8 fall into the same asperities surface density range.

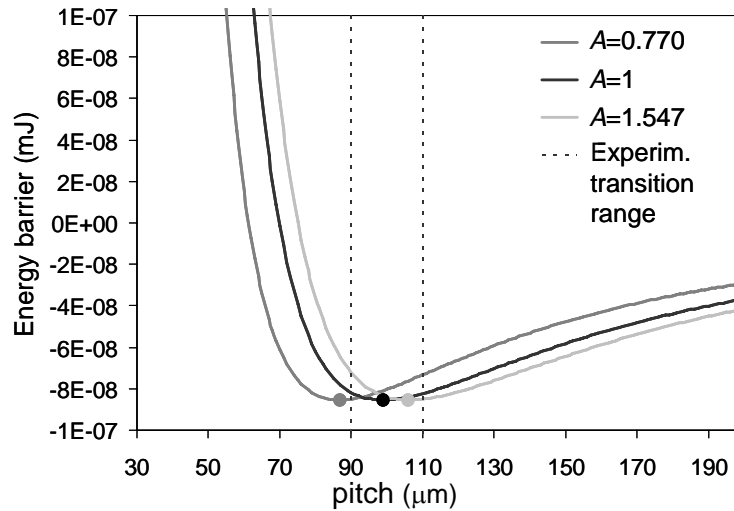


Fig. 4.9 *Energy barrier diagram for different disposition factor  $A$ , as a function of pitch. The energy barriers minima (full dots), derived from Eq. 4.13 for the different  $A$  values, result in agreement with the experimental observation. They fall in the right order, and in the region of the experimental Cassie-Wenzel transition, delimited by the two vertical dashed lines.*

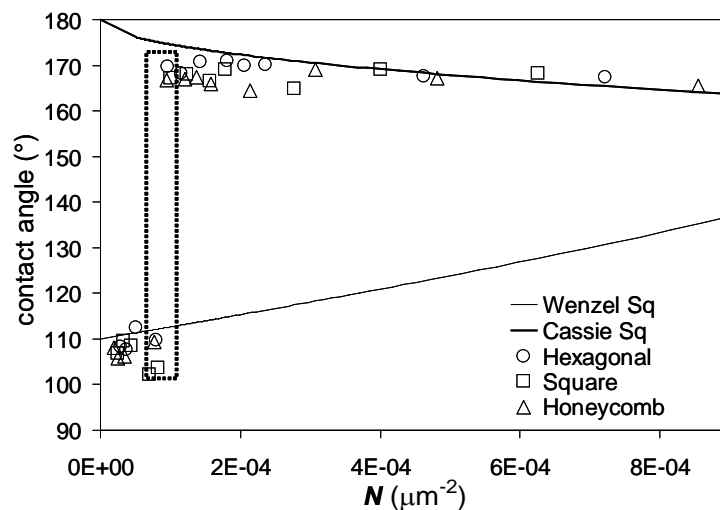


Fig. 4.10 *All the data obtained for the different dispositions are reported as a function of the pillars surface density ( $N = A/p^2$ ). The dashed rectangle evidences the very narrow range of  $N$  where all transitions fall (comprised between 0.77 and 1 pillars per  $(100 \times 100) \mu\text{m}^2$ ).*

This similarity in the  $N$  values at the experimental Cassie-Wenzel transition confirms that the drops are not sensitive to the distribution of micrometer obstacles (provided these obstacles are homogeneously and regularly distributed on the surface), and supports the validity of the axis-symmetric drop-shape assumption. Even though the drop may sit only on a limited number of pillars (calculations give between 5 and 6 pillars of 10- $\mu\text{m}$  diameter with pitch of 100  $\mu\text{m}$  under a 3- $\mu\text{L}$  drop with a contact angle of  $170^\circ$ ), no effect was observed on the static wetting regime (i.e. if *composite* or *wetted*) that potentially could be attributed to the different three-phase contact line distortions caused by different obstacles surface arrangements.

To summarize, both pitch and disposition factor influence the Cassie-Wenzel transition, in agreement with thermodynamic models. The different geometrical arrangements considered in this study are sufficiently regular and symmetric to avoid observable differences in the drop wetting behavior. Consequently, the Cassie-Wenzel transition can be analyzed in terms of asperity surface density  $N$ . In the case presented here (cylindrical pillars of 10- $\mu\text{m}$  diameter, 40- $\mu\text{m}$  height) the transition is observed for  $0.77 < N < 1$  pillar per  $(100 \times 100) \mu\text{m}^2$ .

### Influence of $d$ , cylindrical pillar diameter

The influence of pillar diameter in case of cylindrical obstacles is presented in Fig. 4.11.

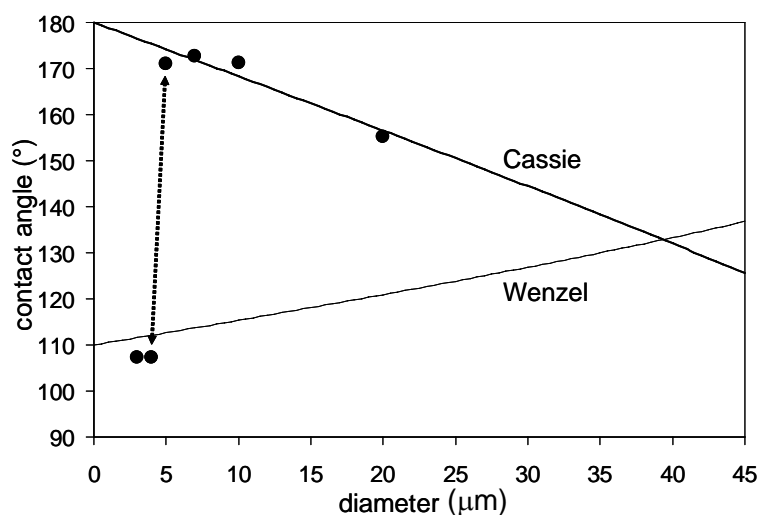


Fig. 4.11 *Diameter influence on SCAs.* Water SCAs of a  $\sim 3\text{-}\mu\text{L}$  drop on square dispositions ( $A = 1$ ) of cylindrical pillars as a function of pillar diameter (constant  $p = 50 \mu\text{m}$  and  $h = 20 \mu\text{m}$ ). Cassie and Wenzel theoretical curves are also reported. Wenzel regime corresponds to small diameters and Cassie regime to pillar diameters larger than  $4 \mu\text{m}$ . The experimental Cassie-Wenzel transition is marked by the dashed double arrow.

The samples series under consideration present square arrangements ( $A = 1$ ) of cylindrical pillars with constant height and pitch ( $h = 20 \mu\text{m}$ ,  $p = 50 \mu\text{m}$ ), and pillar diameter comprised in the range  $3 \mu\text{m} < d < 20 \mu\text{m}$ . Since all values are again close to one of the two curves, classic Cassie and Wenzel models confirm their validity. Also in this case the transition *composite-wetted* regime appears far away from the theoretical position (calculated for  $d = 40.3 \mu\text{m}$ ), therefore it can be affirmed that all the observed Cassie angles correspond to metastable *composite* states. In Fig. 4.12, representing the thermodynamic analysis of the system as a function of the diameter increase, the experimental Cassie-Wenzel transition (appearing between 4 and 5  $\mu\text{m}$ ) falls in the region close to the energy barrier minimum (calculated for  $d = 3.4 \mu\text{m}$ ).

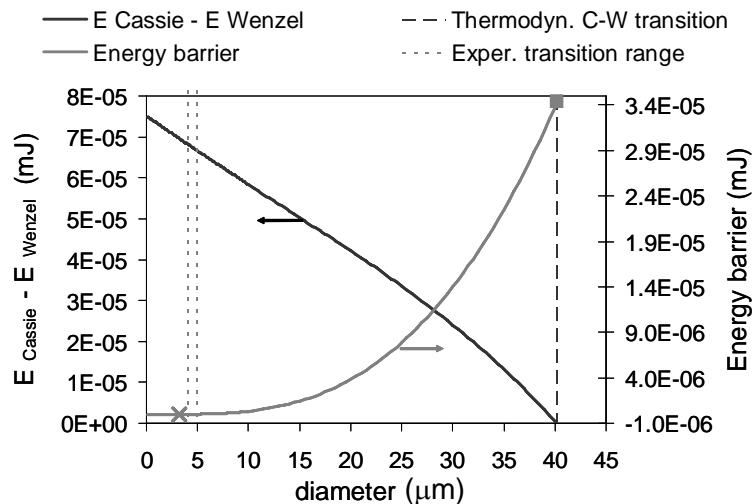


Fig. 4.12 *Diameter influence on system thermodynamic energy.* The black line (left scale) represents the energy difference between *composite* and *wetted* state as a function of the pillar diameter, whereas the gray line (right scale) the energy barrier to fill the asperities in the range where the Cassie regime is metastable (from Eq. 4.13). The symbol (■) represents the energy barrier at the Cassie-Wenzel equal energy point. Again the experimental transition (delimited by the two dashed vertical gray lines) occurs close to the calculated energy barrier minimum (X).

### Influence of $h$ , cylindrical pillar height

In Fig. 4.13, water SCA values are reported as a function of the pillar height, for a series of samples with square distribution ( $A = 1$ ) of 10- $\mu\text{m}$  diameter cylindrical pillars with constant pitch  $p = 30 \mu\text{m}$ , and height  $h$  comprised between 1 and 40  $\mu\text{m}$ . For this whole height range, the Wenzel *wetted* state is calculated to be the thermodynamic favored regime; however, almost all measurements show SCAs corresponding to metastable *composite* states.

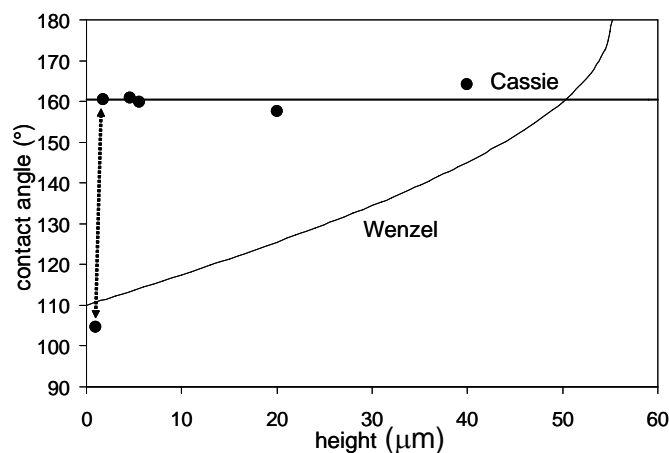


Fig. 4.13 *Height influence on SCAs.* Water SCAs of  $\sim 3\text{-}\mu\text{L}$  drops, and theoretical Cassie and Wenzel curves, for samples with square disposition ( $A = 1$ ) of cylindrical pillars as a function of pillar height (constant  $p = 30\ \mu\text{m}$  and  $d = 10\ \mu\text{m}$ ). The double arrow indicates the Cassie-Wenzel transition.

In particular, being the *composite* case independent of the pillar height, the Cassie curve results a straight line at about  $160^\circ$ . Thermodynamic estimation of the energy barrier to overcome the metastable *composite* states, and to reach the thermodynamically favored *wetted* states, shows that this energy decreases to zero with decreasing pillar height (see Fig. 4.14).

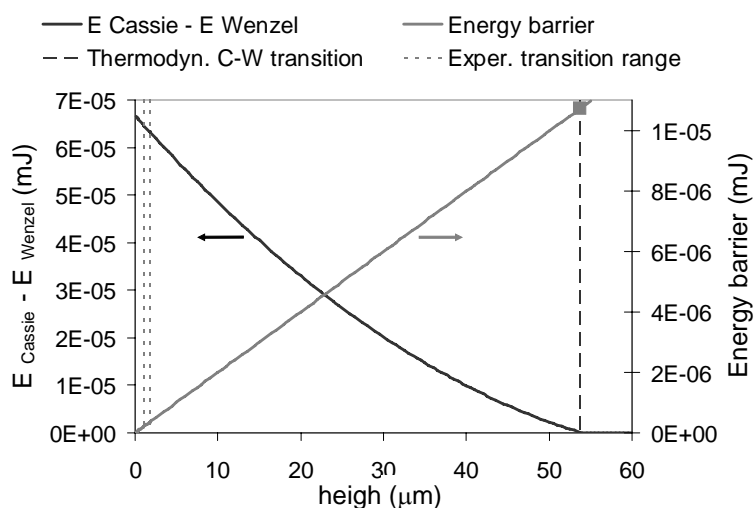


Fig. 4.14 *Height influence on system thermodynamic energy.* The energy barrier estimated (from Eq. 4.13) to pass from the Cassie metastable *composite* state to the Wenzel *wetted* state is reported as gray line (right scale), proving that the experimental transition occurs in a region where this energy is very low. The symbol (■) represents the energy barrier at the Cassie-Wenzel equal energy point.



The transition to the Wenzel regime is observed for the minimum considered asperity height ( $h = 1 \mu\text{m}$ ). However, this observed transition should be related to the unavoidable vibrations of the liquid-vapor menisci among the asperities at the macroscopic liquid-solid interface associated with the drop deposition. Due to such vibrations, the liquid can possibly touch the bottom of the asperities, thus generating the thermodynamically stable Wenzel state. To illustrate this, Fig. 4.15 shows a real scale image of the situation of a water drop in, and on top of, the asperities (Fig. 4.15-a and b, respectively). In such a figure, the distance between two consecutive obstacles, to be correlated with the maximum meniscus curvature, is the largest distance  $z$  for a regular square arrangement of obstacles, and is given by the expression  $z = \sqrt{2}p - d$ .

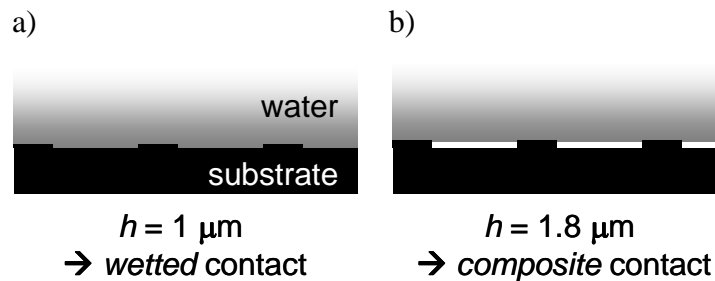


Fig. 4.15 A side schematic view of the contact between water and the structured surfaces at scale, for the two smallest considered heights ( $h = 1 \mu\text{m}$  and  $h = 1.8 \mu\text{m}$ ), showing the *wetted* and the *composite* regimes observed respectively for  $h = 1 \mu\text{m}$  and  $h = 1.8 \mu\text{m}$ . For the square arrangement, the largest distance  $z$  between two consecutive obstacles, to be correlated with the meniscus curvature, is given by  $z = \sqrt{2}p - d$ .

The *composite* state observed for a pillar height of  $1.8 \mu\text{m}$  (Fig. 4.15-b) shows that the meniscus in the cavities presents a radius of curvature larger than that calculated assuming a contact angle at the asperities edges equal to the advancing angle on the flat silanized surface ( $116^\circ$ ), as proposed by Extrand [55], and other authors [44][50]. As a matter of fact, a minimum pillar height of  $3.7 \mu\text{m}$  would be required in this case in order to keep the drop in the composite state (assuming a spherical meniscus shape). However, in Chapter 5 (“Influence of pillar height on Cassie-Wenzel transition” paragraph), experimental evidences will be shown to support the validity of Extrand’s assumption in the case of dynamic contact angle measurements.

### **Influence of L, top-surface pillar perimeter**

To investigate the influence of pillar top-surface perimeter, samples were prepared with square distribution of obstacles, with constant height ( $h = 40 \mu\text{m}$ ), and constant pillar top-

surface area ( $s = 78.5 \mu\text{m}^2$ , which is the area of a 10- $\mu\text{m}$  diameter cylindrical pillar) but with varying obstacle section shape, which results in different top-surface perimeters  $L$  (see Fig. 4.16).

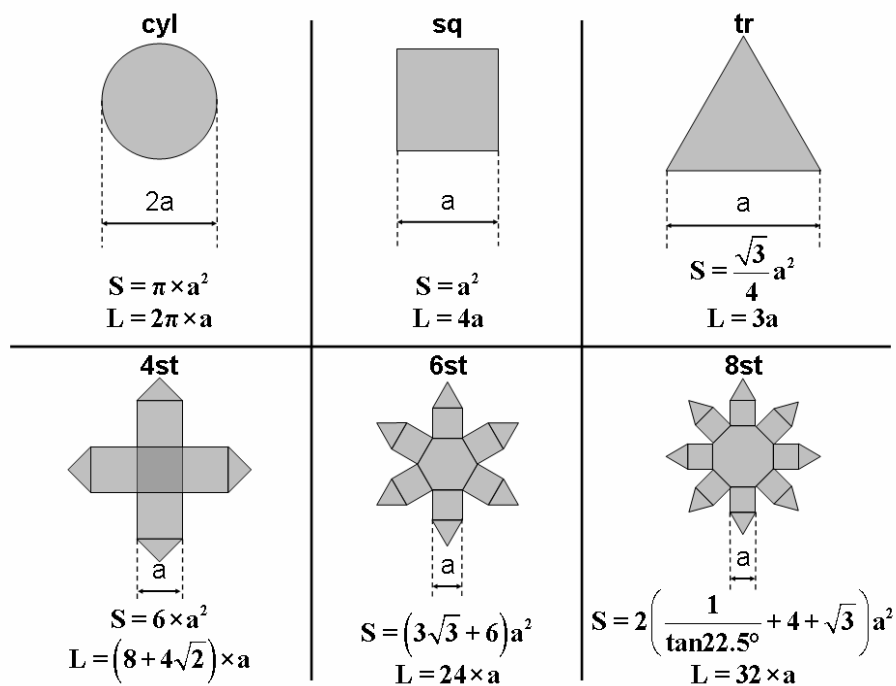


Fig. 4.16 *Different obstacle section perimeters for same top-surface area.* Schematic top-view of the six selected shapes of the pillar surface, with constant area  $S$  and different perimeters  $L$ . In the two rows, from left to right, the shape is circular, square, triangular, 4-edged star, 6-edged star, and 8-edged star. Each shapes can be associated with an unique term “ $a$ ” for deriving analytical expressions of both perimeter and area.

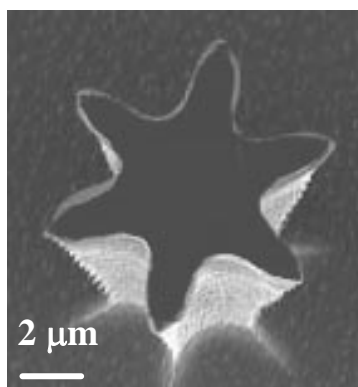


Fig. 4.17 As an example, a SEM image (tilt angle 15°) of a 6-edged star pillar is reported.

Maintaining a constant pillar surface while varying the pillar perimeter is necessary to rigorously determine whether the contact-line length and corrugation play a role in the

robustness of metastable *composite* states, a control that was unfortunately not carried out in previous studies documented in literature [37]. Fig. 4.17 shows the scanning electron microscope tilted ( $15^\circ$ ) image of the 6-edged star structure as an example. Three selected pitches,  $p = 100 \mu\text{m}$ ,  $110 \mu\text{m}$ , and  $120 \mu\text{m}$ , are chosen in the Cassie-Wenzel transition range observed for square distribution of cylindrical pillars (see Fig. 4.5), and the resulting SCAs are reported in Fig. 4.18 as a function of the perimeter length  $L$ .

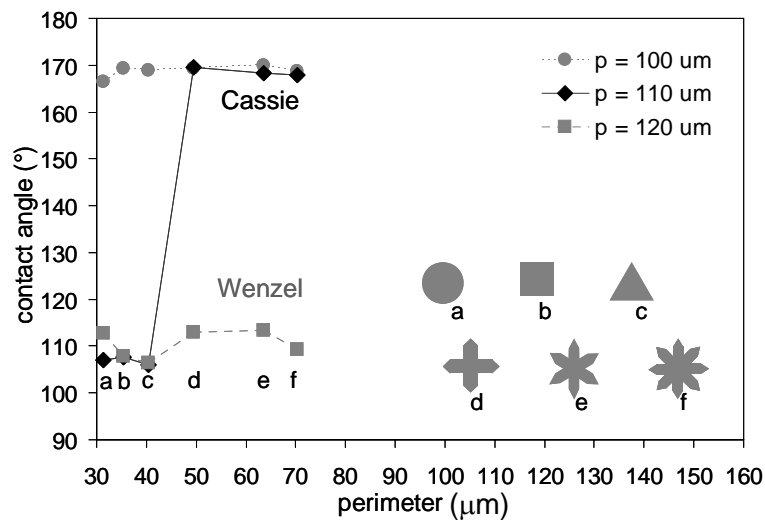


Fig. 4.18 Water SCAs of  $\sim 3\text{-}\mu\text{L}$  drop obtained on substrates with square distribution ( $A = 1$ ) of pillars with same surface area and height ( $s = 78.5 \times 10^{-12} \text{ m}^2$ ,  $h = 40 \mu\text{m}$ ), and different section shapes, as a function of the top-surface perimeter  $L$ . Results are presented for three different pitches  $p = 100 \mu\text{m}$ ,  $110 \mu\text{m}$ ,  $120 \mu\text{m}$ , which all belong to the pitch region where the Cassie-Wenzel transition occurs when the square distribution of cylindrical pillars with identical  $S$  and  $h$  is studied as a function of the pitch (see Fig. 4.5).

For  $p = 100 \mu\text{m}$ , all contact angle values correspond to the metastable *composite* regime, as expected from Fig. 4.5., whereas for  $p = 120 \mu\text{m}$ , all drops are observed in the *wetted* thermodynamically favored state. Only for the intermediate  $p = 110 \mu\text{m}$ , a transition between the metastable Cassie regime into the Wenzel regime is observed between the triangular shape to the 4-edged star shape. This results demonstrates that the increase of the contact line length and corrugation associated with the asperity top-surface perimeter increase, has the effect to increase the extent of the *composite* metastable regime.

The experimental transition range, delimited by two gray dashed lines in the energy analysis of Fig. 4.19 for  $p = 110 \mu\text{m}$ , corresponds again to a low value of the estimated energy barrier with increasing perimeter, to pass from the Cassie metastable *composite* state to the

thermodynamically favored Wenzel *wetted* state.

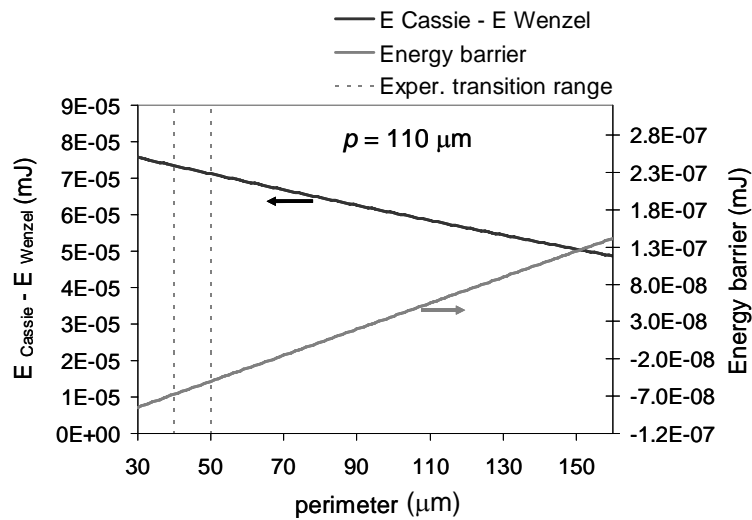


Fig. 4.19 *Obstacle top-surface perimeter influence on system thermodynamic energy for  $p = 110 \mu\text{m}$ . The curve of the energy barrier to pass from the Cassie metastable state to the thermodynamically favored Wenzel state is in agreement with the experimental tendency. We can observe that the energy barrier increases with increasing the obstacle perimeter.*

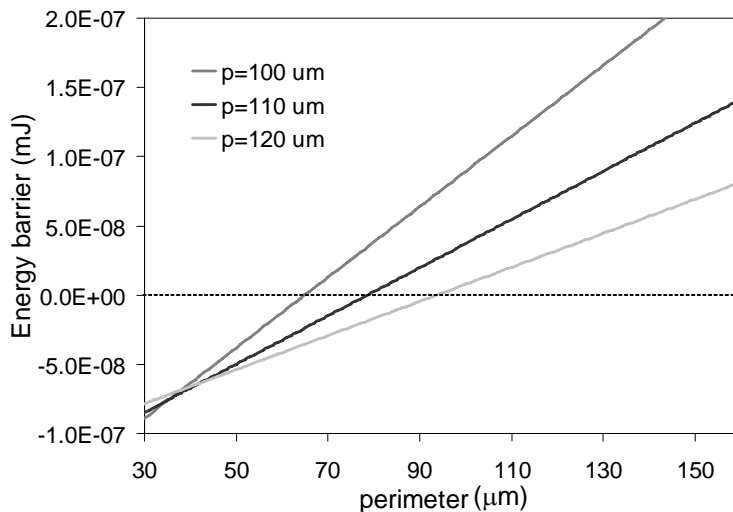


Fig. 4.20 *Calculation of the energy barriers for the three selected pitches as a function of the obstacle perimeter, showing that the barrier energy is lower for lower pitch value.*

The energy barrier calculation for the three considered pitches as a function of the perimeter (Fig. 4.20) shows that the Cassie-Wenzel transition should occur at a smaller perimeter for a smaller pitch and at a higher perimeter for a larger pitch. However, it has to be pointed out that the experimental Cassie-wenzel transition occurs at the change of the pillar

top-surface shape from a convex to a concave structure. Although the presented thermodynamic interpretation seems in agreement with the experimental results without considering this aspect, a possible influence on the Cassie-Wenzel transition position of the contact line shape variation cannot be excluded a priori. Further investigation in this direction would be very useful.

It can nevertheless be concluded that the shown experimental results support the idea that increasing the complexity of the pillar shape enhances the robustness of *composite* metastable states. The implication of the mentioned contact line length and corrugation influence on such a phenomenon will be discussed in more details in Chapter 5.

### Influence of pillar absolute size

The influence of obstacle absolute size, keeping  $f$  and  $r$  parameters constant, was also studied. Five series of samples were prepared varying simultaneously diameter and height of cylindrical pillars in square distribution, using the relations:  $d = i$  and height  $h = 2i$ , for  $i = 3, 5, 10, 14,$  and  $20 \mu\text{m}$ . Each samples series, one for every  $i$  value, consisting of eight different pitches, was selected to have the same series of  $r$  and  $f$  parameters, using the following relations:  $f = \frac{A\pi}{4}\left(\frac{d}{p}\right)^2$ , and  $r = 1 + 2A\pi\left(\frac{d}{p}\right)^2$ . Fig. 4.21 reports a scheme that explains the criterion adopted to prepare these samples, referred to as “scaling criterion”.

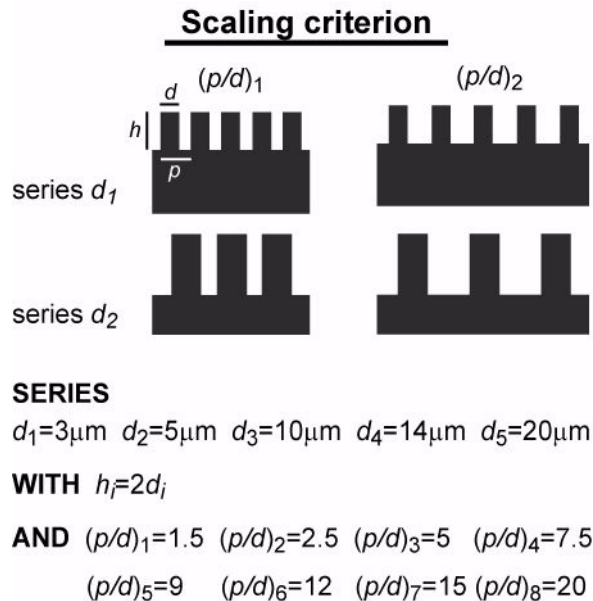


Fig. 4.21 “Scaling criterion”. Scheme illustrating the criterion adopted to prepare the samples with different pillars absolute size in the micrometer range.

Keeping the  $f$  and  $r$  roughness factors constant means that Cassie and Wenzel theoretical models predict exactly the same series of contact angle values for all the five samples series as a function of  $p/d$ , and therefore the identical energy value for the Cassie and Wenzel intersection point, given by the expression  $\left(\frac{p}{d}\right)_{th} = \sqrt{\frac{A\pi(1 - 7\cos\theta_{flat})}{4(1 + \cos\theta_{flat})}}$ , from Eq. 4.12.

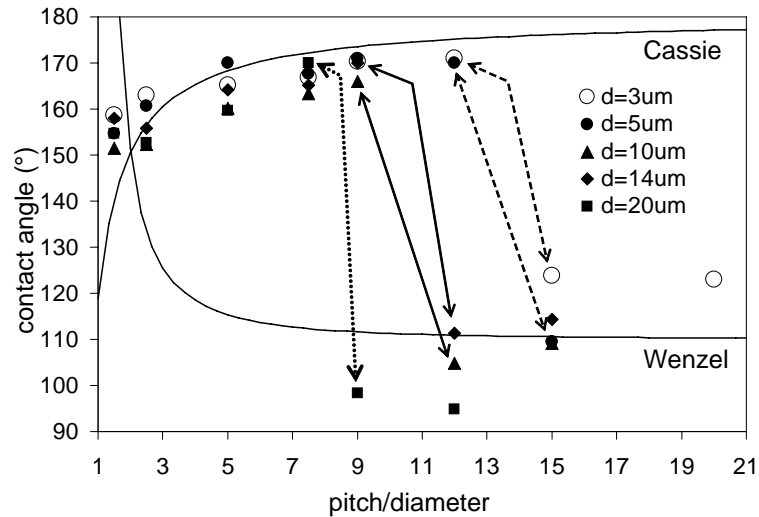


Fig. 4.22 SCA measurements of  $\sim 3\text{-}\mu\text{L}$  drop as a function of  $p/d$  for five different pillar diameters ( $3\ \mu\text{m} < d < 20\ \mu\text{m}$ ), keeping constant  $h = 2d$  and varying  $p$ . Cassie and Wenzel theoretical curves are also reported. Arrows show the Cassie-Wenzel transition position observed for the different samples series. The larger the diameter, the lower the  $p/d$  value at which the Cassie-Wenzel transition occurs.

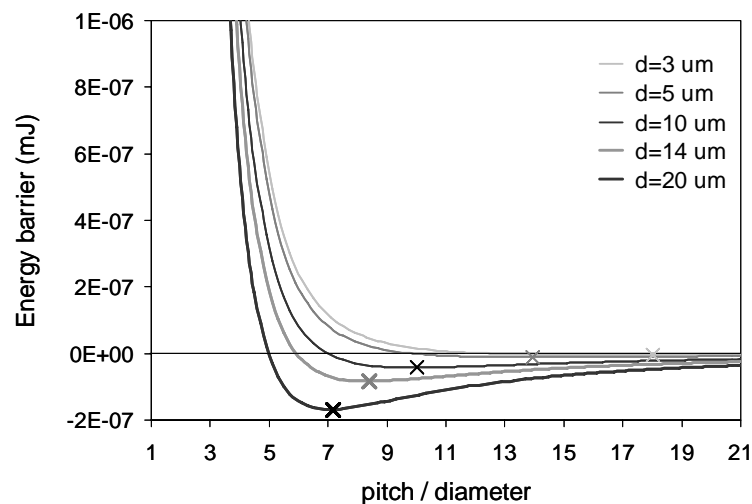


Fig. 4.23 Energy barriers calculated for the five samples series as a function of the  $p/d$  ratio. The energy barrier minimum falls at smaller  $p/d$  when  $d$  is higher, and vice versa, which is in agreement with experimental results. The minima of the energy barriers are marked by crosses.

Fig. 4.22 presents the experimental SCAs, as well as Cassie and Wenzel theoretical curves. The Cassie and Wenzel curves fit correctly the data, and again, transitions from *composite* to *wetted* regimes are observed at pitch/diameter values much larger than the equal energy state at the Cassie-Wenzel intersection. Concerning the Cassie-Wenzel transition, it can be observed that the smaller the pillar diameter, the higher the  $p/d$  value at which it occurs, and vice versa. Calculation of the energy barrier according to Eq. 4.13 shows a good correlation with these data, as all the energy barrier minima approximately correspond to the experimental transition regions (see Fig. 4.23). This constitutes a valuable proof that, for identical  $r$  and  $f$  values, reducing the pillar size in the micrometer range increases the extent of the metastable *composite* state.

### Influence of $f$ , Cassie roughness parameter

Summarizing all the experimental SCA values of this work in Fig. 4.24 as a function of the Cassie roughness factor  $f$  (i.e. the surface fraction of the liquid-solid contact at the drop-substrate interface, from Eq. 4.2) reveals that the transition between the metastable Cassie regime and the Wenzel regime always occurs for low and similar values of  $f$ , all comprised between 0.0035 and 0.0140 (apart from the transition as a function of  $h$ , which mostly depends on another phenomenon, i.e. meniscus curvature due to drop vibration, as discussed earlier).

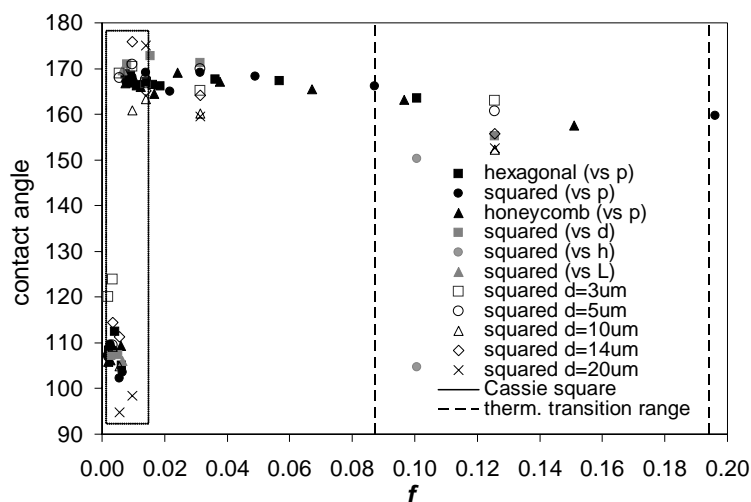


Fig. 4.24 Water SCAs values as a function of Cassie roughness parameter  $f$ . Summary of all results presented in the previous graphs. Cassie theoretical curve is also reported for the series with square distribution of 10- $\mu\text{m}$  diameter pillars. All the experimental transitions take place in the range (delimited by the dashed rectangle)  $0.0035 < f < 0.0140$ , for values much smaller than those thermodynamically predicted, all lying in the range  $0.0873 < f < 0.1939$ , represented in the graph by the two vertical dashed lines.

This means that metastable *composite* drops can sit on 99.6% of air, or, otherwise said, that only 0.4% of the macroscopic drop-solid interface holds the drop in a superhydrophobic state!

The calculated thermodynamic transition between Cassie and Wenzel states for the surface geometries realized in this work lies in the range of  $f$  between 0.0873 and 0.1939 (vertical dashed lines in Fig. 4.24), corresponding to a solid-liquid interface fraction at the drop-substrate contact surface between 8.7 and 19.4%, consequently far away from the observed transitions, and comprised in a much larger  $f$  range.

Dynamic contact angle measurements performed on the same samples series considered in this chapter will be presented in Chapter 5 and Chapter 6, depending on the adopted measurement configuration, and interesting considerations especially concerning the extent and robustness of the metastable *composite* regime will be suggested.

## 4.4 Conclusions

In this chapter, superhydrophobic surfaces with a periodic controlled flat-top roughness in the micrometer range were considered, and the influences of six different geometrical parameters (minimum distance between pillars, pillar geometric distribution mode, cylindrical pillar diameter, pillar height, pillar shape, and absolute pillar size) were investigated by water SCA measurements, at room temperature.

All the measured SCA values (one series for each considered geometrical parameter) were in good agreement with the behavior predicted by a simple thermodynamic interpretation, based on the surface free energy minimization of the considered drop-substrate system. In particular, a transition between the Cassie and the Wenzel regime was experimentally evidenced for a well-defined range of each geometrical parameter. It was shown that when millimeter water drops were softly deposited on the prepared surfaces, the transition did not correspond to the thermodynamic one (i.e. to the point where the Cassie-*composite* and the Wenzel-*wetted* regime present identical contact angle values, and consequently the same energy level), but to a point where the system has enough energy to overcome the energy barrier between its initial metastable *composite* state and the thermodynamically favored *wetted* regime.



Although the details of the Cassie-Wenzel transition remain unknown, its position correlates nicely with a calculation of the energy required to fill the asperities, keeping the Cassie angle constant.



---

## 5 Superhydrophobicity: Adv- and Rec-CA investigations with a negligible extra-pressure

*This chapter presents the results of water advancing and receding contact angle (in the title referred to as “Adv- and Rec-CA” for brevity) measurements performed on microstructured hydrophobic substrates consisting of perfluorosilanzed regularly distributed flat-top pillars, as a function of different geometrical roughness parameters. These dynamic contact angle measurements are conducted exerting a negligible extra-pressure on the system. The Cassie-Wenzel dynamic transition position evidenced for each roughness parameter is discussed in relation to the corresponding static transition (see Chapter 4). The contact angle hysteresis results are shown and discussed in terms of the associated wetting regime. Arguments concerning the influence of the three-phase contact line features, such as its length, fragmentation and corrugation, are proposed with a discussion regarding the results obtained from the study of the Cassie-Wenzel transition position and the contact angle hysteresis as a function of the asperity absolute size. The water dynamic contact angle results obtained on a series of nanostructured and perfluorosilanzed samples allow determination of the asperity size range where superhydrophobicity appears and vanishes, and the most suitable size for designing superhydrophobic surfaces of good quality<sup>1</sup>.*

### 5.1 Measuring dynamic contact angles with a negligible extra-pressure

Advancing and receding contact angle measurements were performed using the same apparatus as indicated in Chapter 4 (paragraph 4.2). Here, a stainless steel needle (500- $\mu\text{m}$  external diameter) is kept at  $\sim 1$  mm from the sample surface. A water drop was formed at its apex by turning a micrometric screw directly connected to the syringe piston. Further turning increased the drop size to a maximum of 7  $\mu\text{L}$ , and turning in the opposite direction again decreased the drop size, both processes being executed at speeds comprised between 0.6 and

1. A scientific article presenting the results discussed in this chapter is in preparation.

0.8  $\mu\text{L}/\text{sec}$ . When the drop-substrate contact occurred, a video started to record drop variation during the complete dynamic process (acquisition rate of 25 frames/sec). The contact angle that the drop forms during liquid supplying, from the moment when the drop-substrate contact base starts to increase, represents the *advancing* angle. Conversely, the contact angle formed during liquid withdrawing, from the moment when the drop base starts to decrease, represents the *receding* angle. All the *advancing* and *receding* angle values reported in this chapter correspond to the average of at least five measurements performed on at least five frames recorded during drop volume increase and decrease, respectively. Fig. 5.1 shows a sequence of images selected from a video of a typical dynamic contact angle measurement process. From image 2 of the sequence, it can be noted that a certain extra-pressure is exerted on the system by this method: in fact, the liquid drop is somehow squeezed between the substrate and the needle apex. The pressure exerted on the curved liquid-air interface of the squeezed drop is the same as that exerted on the substrate in this initial phase of the drop volume increasing process. For Laplace, such a pressure is quantifiable by considering the radius of curvature of the liquid-air interface  $x$ , and the surface tension of the liquid  $\gamma_{LV}$ , and substituting in the equation  $\Delta P = 2\gamma_{LV}/x$ . In this case, such an equation will be expressed in the equivalent form  $\Delta P = 2\gamma_{LV}|\cos\theta|/x$ , where  $|\cos\theta|$  is the corrective term for considering the specific contact angle formed by the drop at the substrate at the moment when it is squeezed [47]. In this case,  $x$  corresponds to half of the distance between the needle apex and the substrate.

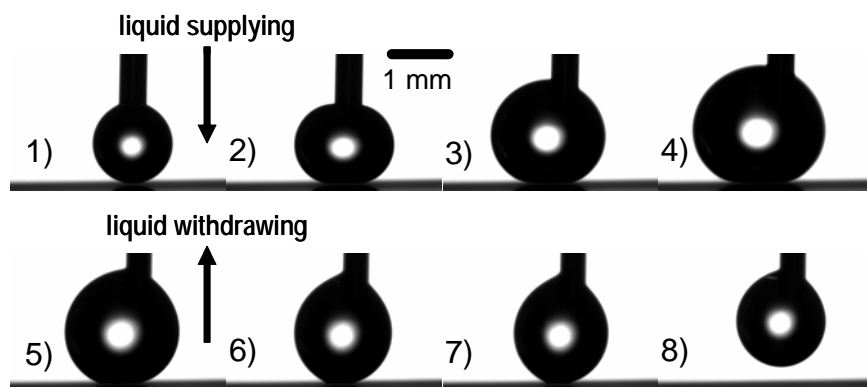


Fig. 5.1 *Dynamic contact angle measurements exerting a negligible extra-pressure on the drop-substrate system. Image sequence selected from a typical video recorded for advancing and receding contact angle measurements by the sessile drop method (typically 200 frames taken with an acquisition rate of 25 frames/sec). The drop volume total variation related to a typical dynamic measurement corresponds to  $\sim 6\text{-}7 \mu\text{L}$ .*

By considering  $x \sim 0.5$  mm, and an overestimated contact angle of  $180^\circ$  for image 2 - Fig. 5.1, the related extra-pressure is overestimated by  $\sim 300$  Pa (corresponding to  $\sim 3$  cm of water). Such a pressure can be considered negligible in this systematic dynamic study, since no significant difference was evidenced in comparing the Cassie-Wenzel transition positions, recorded for each considered geometrical parameter by dynamic measurements, to those recorded by static measurements (further comments on this aspect are presented in the following paragraph). In conclusion, during dynamic measurements, it must be borne in mind that the liquid supplying and withdrawing, even if performed in a quasi-stationary regime (i.e. with a very low volume variation rate), are always associated with a perturbation of the system. These perturbations induce wetting transition from metastable *composite* states to *wetted* states more and more easily when the energy barriers between the states are lower (see references [47][49][50][51][53][70][72][93]).

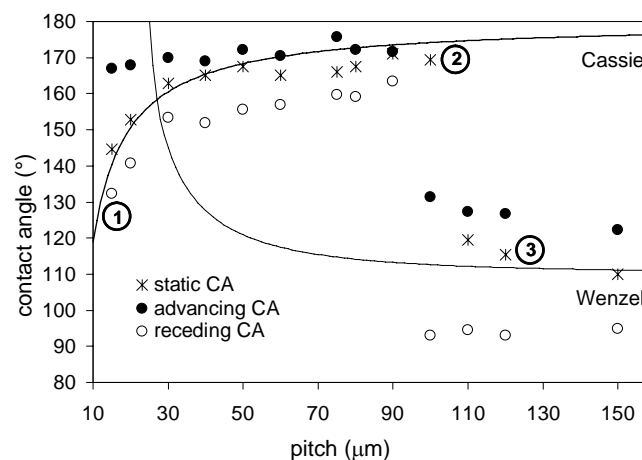
## 5.2 Dynamic contact angle results

“SCA” hereafter designates “static contact angle”; “DCA” “dynamic contact angle”; “ACA” “advancing contact angle”; “RCA” “receding contact angle”; and “CAH” “contact angle hysteresis”.

### Influence of pillar spacing on Cassie-Wenzel transition

The results of water ACA and RCA measurements performed on microstructured perfluorinated silicon surfaces, with periodical distribution of identical flat-top obstacles differing in pitch size (with  $p$  comprised between  $15 \mu\text{m}$  and  $150 \mu\text{m}$ ) are presented in Fig. 5.2.

a)



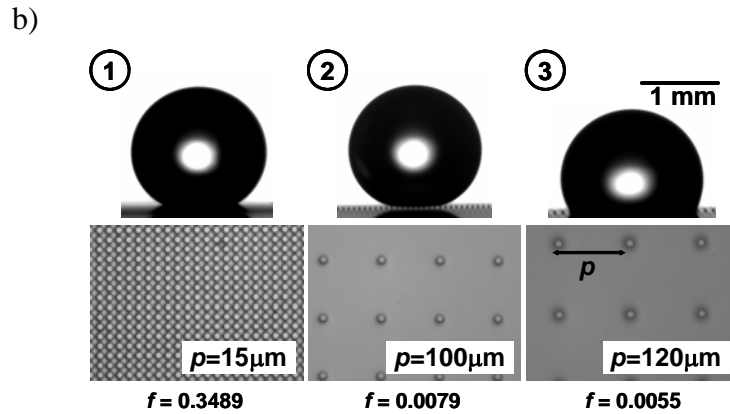


Fig. 5.2 *Pitch influence on DCAs.* a) Water ACA and RCA values measured on samples with square disposition of cylindrical pillars ( $d = 10 \mu\text{m}$ ,  $h = 40 \mu\text{m}$ ) with different pitch, and comparison with the related SCA values, and with Wenzel and Cassie models. b) Images of  $\sim 3\text{-}\mu\text{l}$  water static drops in contact with surfaces presenting three different pitches (1, 2, 3 correspond to  $p = 15, 100, 120 \mu\text{m}$ , respectively). The values of the  $f$  Cassie roughness factor for each surface are also indicated.

For details concerning adopted methods of silicon microstructuring and perfluorosilanzation see Appendix 1 and Chapter 3 respectively. The SCA values (already presented in Chapter 4, Fig. 4.5) are also reported for comparison.

Cassie and Wenzel curves, calculated considering the water SCA on the flat silanized  $\text{SiO}_2$  surface ( $\theta_{flat} = 110^\circ$ ), are reported on the same graph as continuous lines. The measured static values and the values calculated by the two models result in good agreement. As expected, all the static values are comprised between the corresponding DCAs. *Composite* states are observed for a much wider pitch than that of the thermodynamic transition point between the two regimes, represented by the intersection between the two curves. The energy analysis of the position where the static Cassie-Wenzel transition effectively occurs is reported in Chapter 4, where a rough estimation of the energy barrier that metastable *composite* Cassie states have to overcome to be transformed into Wenzel *wetted* states is in agreement with the experimental results. Static and dynamic transitions from the Cassie to Wenzel state appear within a narrow range of pitch. The last observed Cassie state increasing the pitch is found at  $p = 10d$  and  $p = 9d$ , respectively, for static and dynamic measurements. This represents a further validation of the model proposed in Chapter 4, since the estimated extra-pressure of  $\sim 300 \text{ Pa}$ , associated with the dynamic measurements technique adopted in this work, is sufficient to induce the Cassie-Wenzel transition only for the static *composite* state observed at minimum asperities surface density (i.e.  $p = 100 \mu\text{m}$ ). Subsequently, in this chapter, an interpretation of the possible shift direction observed by comparing static and dynamic Cassie-Wenzel

transition positions, as a function of a precise roughness parameter, will be formulated and associated with the relative robustness of the related *composite* states. Contrary to what is proposed by other authors [35][44][51][55], the drop gravity effect is excluded as possible significant factor in determining the transition from the *composite* Cassie to the *wetted* Wenzel state. Static and dynamic contact angle experiments, repeated varying the water drop volumes in the range from  $\sim 1 \mu\text{l}$  up to  $\sim 12 \mu\text{l}$  on the two substrates limiting the Cassie-Wenzel experimental transition, showed the same *composite* or *wetted* wetting regime. If the drop volume is increased, the water-air interface shape deviates from a sphere cup according to the Laplace equation, due to the gravity effect contribution. For very large volumes, drops are flattened in the upper part, and the equation

$$k = 2a \sin \frac{\theta}{2} \quad (5.1)$$

where  $a = \sqrt{\gamma_{LV}/(\rho g)}$  represents the capillary length, and  $\theta$  the contact angle that the drop forms with the considered surface, gives the maximum drop thickness of large drops (see reference [80] and references therein). Being the capillary length for water  $\sim 2.7 \text{ mm}$  (at  $20^\circ\text{C}$ ,  $1 \text{ atm.}$ ),  $k \sim 5.4 \text{ mm}$  corresponds to the maximum possible thickness for a big water drop with a maximum ideal contact angle of  $180^\circ$ . The associated maximum pressure acting on a surface, due to the gravitational energy of a water drop deposited on it, is estimated as being  $\sim 50 \text{ Pa}$ , substituting  $k_{\text{max}} \sim 5.4 \text{ mm}$  in  $P = \rho g k$ . Such a value is far lower than  $P = 300 \text{ Pa}$ , i.e. the pressure associated with the initial phase of the adopted DCA measurement technique, previously defined as negligible in determining the transition from the *composite* to the *wetted* state (see Paragraph 5.1). This confirms the good stability of the observed metastable *composite* states in the considered pillar size range, even at high pitches, and thus the Cassie-Wenzel transition phenomenon may be interpreted as being mainly influenced by variations of the system surface free energy and three-phase contact effects (the former associated with the thermodynamic considerations presented in Chapter 4, and the latter associated with aspects that will be discussed later in this chapter - “Influence of pillar absolute size on Cassie-Wenzel transition” section of this paragraph).

Concerning the hysteresis trend, two main regions of  $\Delta\theta$  are evidenced in Fig. 5.3 by the two dashed lines, corresponding to the two possible *composite* and *wetted* regimes. Basically, there are two substantially different phenomena. In the *composite* states part ( $p \leq 90 \mu\text{m}$ ), the minimum measured hysteresis is  $8^\circ$ , and the rapid  $\Delta\theta$  diminution when the pitch is increased

corresponds to an enhancement of the so-called “self-cleaning properties” of the surfaces, for which the ideal hysteresis limit value is  $0^\circ$ . The low hysteresis values recorded for such *composite* drops on surfaces with wide pitches is associated with a practically spontaneous drop rolling on the same surfaces, just slightly tilted.

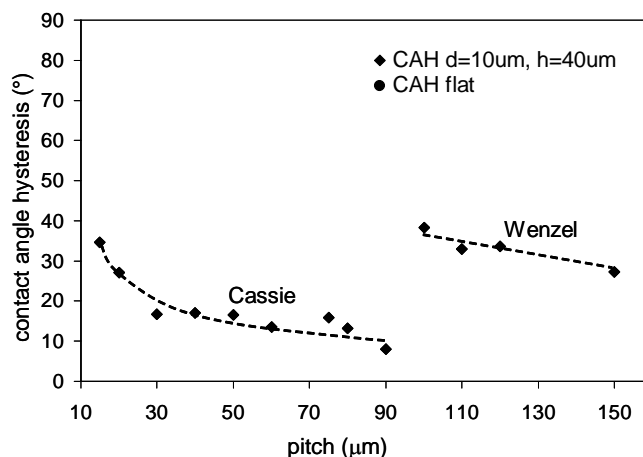


Fig. 5.3 CAH values (i.e. the difference between ACA and RCA) related to results shown in Fig. 5.2. The value on the perfluorosilanzed flat substrate is also reported for comparison. The dashed lines serve as visual guides.

This phenomenon can be represented as involving both the solid-liquid contact surface at the substrate-drop interface and three-phase contact line. During the demonstrated “drop rolling” [96] on a regularly structured surface, they can be assumed to change position but remain constant in area and length respectively, since during the rolling process the drop contact angles can be considered constant. The practically spontaneous drop displacement (i.e. for  $\sim 0^\circ$  substrate tilt angle), observed independently of the drop volume for Cassie drops deposited on the structured surfaces with wider pitch, can be ascribed to the low energy barrier between the neighboring positions assumed by the drop on such a surface. The “total pinning” phenomenon that opposes the motion of the rolling drop is smaller for surfaces with larger pitch since the related number of pillars in contact with the drop is lower. In this case, both the total solid-liquid contact area at the drop-substrate interface and the total three-phase contact line length decrease. In other words, when the pitch is increased, the number of obstacles in contact with *composite* drops of the same volume is lower, and the energy barrier to the movement of the related smaller total contact area and shorter contact line is lower.

Rough estimations of the “total contact line” length  $CL_{\text{tot}}$ , and the related number of pillars  $N_{\text{tot}}$  (or “total contact line fragments”) per unit planar surface of the structured



substrate, are calculated and reported in Fig. 5.12-a for square distributions ( $A = 1$ ) of pillars with three different diameters ( $d = 3\mu\text{m}$ ,  $5\mu\text{m}$ ,  $10\mu\text{m}$ ), as a function of the pitch in the region where *composite* states were experimentally observed (see the section “Influence of pillar absolute size on Cassie-Wenzel transition” for detailed definition and calculation of the  $CL_{\text{tot}}$  and  $N_{\text{tot}}$  parameters).

Different observations can be made concerning the hysteresis trend observed for  $p \geq 100\mu\text{m}$ , i.e. in the region of the Wenzel regime. Here the hysteresis phenomenon involves only an external three-phase contact line since water wets asperities completely. The recorded hysteresis diminution is again due to a decrease in contact line length, but in contrast to the *composite* regime, here the three-phase contact line is continuous. During the liquid withdrawing from the drop, it is pinned to the asperities, and obliged to follow their whole contour in the three directions. Energy barriers between consecutive configurations during the drop volume variation are higher, and for comparable speeds of supplying and withdrawing, the liquid pinning is more significant for surfaces with lower pitch, which present a larger number of obstacles per unit area. The pitch increase induces a slow hysteresis decrease, and ideally, for pitches tending towards the diameter of the deposited drop, water drops should behave as on flat surfaces (where hysteresis measures  $\sim 12^\circ$  - see Chapter 3). With these experiments, the  $f$  value range, comprised between 0.0065 and 0.0097 (corresponding to  $p = 90$  and  $100\mu\text{m}$ , respectively), has been associated with the Cassie state that presents the minimum hysteresis for surfaces with regular distribution of cylindrical flat-top  $10\text{-}\mu\text{m}$  diameter pillars, and identified with both the static and dynamic Cassie-Wenzel transitions. In Fig. 5.2-b the optical microscope lateral images of water drops are related to the top-view microscope images of the corresponding pillar-like surfaces for selected pitches. The immediately visible differences in the surface density of the asperities is underlined by the values of the related  $f$  Cassie roughness factors. Image 2 of Fig. 5.2-b represents a  $\sim 3\text{-}\mu\text{l}$  water drop suspended on a surface composed more than 99% of air! It should be emphasized here that the best self-cleaning properties (i.e. minimum hysteresis values) experimentally observed are associated with metastable *composite* states at the limit of the minimum asperity surface density where *composite* states are allowed, and which, because of this, are predisposed to easier transformation into the corresponding Wenzel state (i.e. for which the energy barrier that has to be overcome for the Cassie-Wenzel transformation is minimum - see Chapter 4).

### Influence of pillar diameter on Cassie-Wenzel transition

The influence of the pillar diameter on the DCA investigations in the presence of a negligible extra-pressure is shown in Fig. 5.4, together with the SCA values, for a samples series composed of a square distribution ( $A = 1$ ) of cylindrical pillars, 20- $\mu\text{m}$  height, with pitch  $p = 50 \mu\text{m}$ , and diameter comprised between 3  $\mu\text{m}$  and 20  $\mu\text{m}$ .

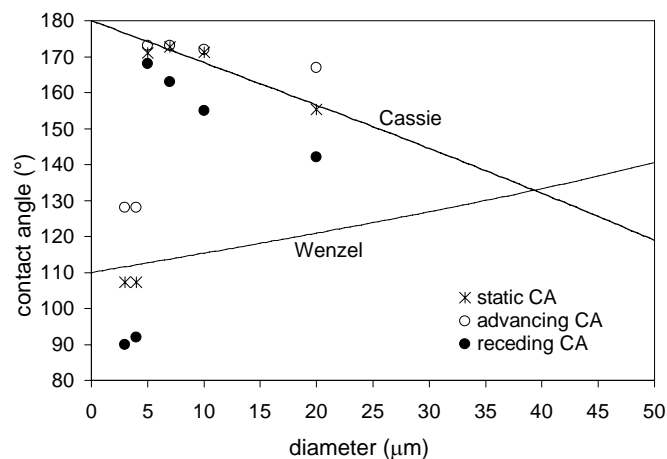


Fig. 5.4 Diameter influence on DCAs. SCA and DCA values measured for water drops deposited on samples with square dispositions ( $A = 1$ ) of cylindrical pillars ( $h = 20 \mu\text{m}$ ,  $p = 50 \mu\text{m}$ ) with different diameters, and comparison with Wenzel and Cassie models (decreasing and increasing continuous curves, respectively).

Again, the metastability range of the static Cassie state is confirmed by the DCA measurement technique adopted. In particular, the experimental position of the Cassie-Wenzel transition exhibited by both static and dynamic measurements is the same, corresponding to a range delimited by the values 4 and 5  $\mu\text{m}$ . This result signifies that in all considered cases the energy associated with an extra-pressure of  $\sim 300 \text{ Pa}$  was insufficient to overcome the energy barrier necessary to induce the Cassie-Wenzel transition. Even the 5- $\mu\text{m}$ -diameter pillar substrate, corresponding to the first *composite* state found in the direction of the diameter increase, and associated with the considered minimum energy barrier between Cassie and Wenzel states, requires a pressure higher than  $\sim 300 \text{ Pa}$  to induce the transition.

Fig. 5.5 shows the contact angle hysteresis results derived from Fig. 5.4. In this case also, the evident change in the CAH value as a function of the pillar diameter increase can be associated with the change from *wetted* to *composite* in the wetting regime. In particular, the two different hysteresis tendencies related to the two different regimes in the considered diameter range give rise to some interesting observations. While for the *wetted* regime a

decrease in the hysteresis value is observed when the pillar diameter is increased, for the *composite* regime an increase is observed.

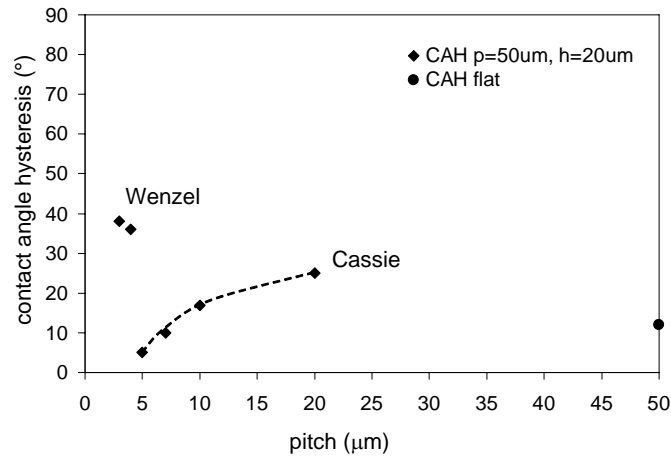


Fig. 5.5 CAH values related to DCA results of Fig. 5.4. The value on the flat substrate is also reported for comparison. The dashed line serves as a visual guide.

In the first case, the three-phase contact line can be imagined continuous and moving on a 3-D surface. On top of the pillars it presents a larger curvature radius for larger diameter. As mentioned in Chapter 2 (see Eq. 2.16 in “Contact line tension effect” section), a lower discrepancy from the Wenzel calculated contact angle is theoretically justified if the contact line curvature is larger [136]. In practice, a larger contact line curvature radius can be associated with a lower pinning of the contact line, and consequently its easier motion during dynamic measurements. In the case of *composite* regimes, the arguments are different. Here the three-phase contact line is discontinuous and moves on a 2-D surface. Since the samples considered in this study present the same pitch, the contact line fragmentation can be considered constant, but the difference in pillar diameter implies a longer contact line for a larger diameter. A *composite* state related to a longer contact line can be associated with a more significant pinning phenomenon at asperity edges. An increment of pinning during DCA measurements causes an increase in the related CAH values. The observations made subsequently, under “Influence of pillar absolute size on Cassie-Wenzel transition”, will complete and clarify the basis for the proposed interpretation to hysteresis variation as a function of pillar diameter. Finally, it can be noted that the CAHs of *composite* states cannot increase indefinitely by increasing the diameter. For a diameter close to pitch width, the hysteresis value should presumably be close to the value on the flat substrate.

## Influence of pillar height on Cassie-Wenzel transition

Some authors [44][49][50][55] have clearly mentioned obstacle height as being one of the fundamental parameters that must be optimized to obtain robust *composite* superhydrophobic substrates. Despite the fact that no experimental evidence exists describing liquid penetration among the asperities of a rough surface due to an extra-pressure acting on the liquid drop, initially suspended in the *composite* regime, and that the Cassie-Wenzel transition mechanism is still not understood, the concept that the greater the asperity height, the more robust the *composite* state remains intuitive. This originates from the assumption that the irreversible collapse of the *composite* drop into the *wetted* regime can be considered the consequence of the contact between the liquid and the bottom surfaces of the asperities. However, here the influence of the asperity height on the dynamic wetting properties of microstructured surfaces is studied in the presence of a negligible extra-pressure acting on the drop-substrate system (as described in Paragraph 5.1).

A series of samples presenting a square distribution ( $A = 1$ ) of flat-top cylindrical pillars of identical diameter and pitch ( $d = 10 \mu\text{m}$ ,  $p = 30 \mu\text{m}$ ) but different height ( $h$  ranging from  $1 \mu\text{m}$  to  $40 \mu\text{m}$ ) were considered. In particular, the selected  $p = 30 \mu\text{m}$  lies in the region where surfaces with square distribution of  $10\text{-}\mu\text{m}$  diameter pillars should present the Wenzel regime as the thermodynamically favored state (see Cassie and Wenzel theoretical curves in Fig. 5.2). The Cassie *composite* states possibly observed are thermodynamically metastable (see Chapter 4).

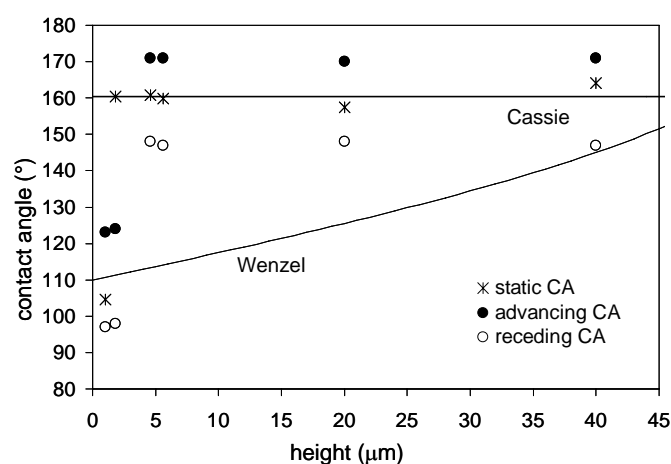


Fig. 5.6 *Height influence on DCAs.* SCA and DCA values measured for water drops deposited on samples with square disposition of cylindrical pillars ( $d = 10 \mu\text{m}$ ,  $p = 30 \mu\text{m}$ ) of different height, and comparison with Wenzel and Cassie models (decreasing and increasing continuous curves, respectively).

In Fig. 5.6 the experimental water SCAs, ACAs and RCAs are reported as a function of pillar height, together with the Cassie and Wenzel theoretical curves calculated for  $\theta_{\text{flat}} = 110^\circ$ . The dynamic Cassie-Wenzel transition falls at a slightly greater height than the static transition. This again validates the theoretical model proposed in Chapter 4, being the exerted extra-pressure sufficient to shift the transition for the least stable metastable states as evidenced by static measurements. The dynamic measurements show a *wetted* regime for the two lowest considered asperity heights of 1  $\mu\text{m}$  and 1.8  $\mu\text{m}$ , while *composite* states are observed for  $h = 4.6 \mu\text{m}$ . The pressure of  $\sim 300 \text{ Pa}$ , associated with the DCA measurements, as limit effect can provoke a deformation of the meniscus between consecutive asperities until its curvature at the asperity edge forms a contact angle equal to the advancing contact angle on the flat surface ( $\theta_{\text{adv flat}} = 116^\circ$ ), with a related maximum penetration depth  $z \sim 3.7 \mu\text{m}$  (given by the relation  $z = \sqrt{2p - d}$ ). This interpretation is confirmed by the observation of the *wetted* state on the two considered substrates with  $h \leq 3.7 \mu\text{m}$  (i.e.  $h = 1 \mu\text{m}$  and  $1.8 \mu\text{m}$ ) and the *composite* states for  $h \geq 3.7 \mu\text{m}$ . On the substrate with  $h = 4.6 \mu\text{m}$ , the maximum meniscus penetration  $z = 3.7 \mu\text{m}$  would in fact not be sufficient to provoke the liquid-solid contact at the asperity base level, causing the *wetted* contact. This is why on samples with  $h \geq 3.7 \mu\text{m}$ , drops maintain the *composite* states even during dynamic measurements.

On the basis of such results, we can firstly exclude any partial liquid penetration among the asperities associated with both static *composite* and dynamic *composite* states where no significant extra-pressure is applied. As shown in Chapter 4, hypothetical states associated with partial liquid penetration among the asperities are never energetically favored. Secondly, the flatness of the meniscus between two consecutive obstacles associated with static drops in *composite* contact with rough surfaces can be confirmed, as suggested in Chapter 4.

The images shown in Fig. 5.7, recorded using an environmental scanning electron microscope (ESEM) during a water condensation process, support this interpretation, although related to a surface with a very small pitch ( $p = 15 \mu\text{m}$ ). Thus, the flatness of the menisci in Fig. 5.7 could be interpreted as an effect of a consistent line-tension contribution, due to the visible deviation from a sphere portion of the liquid-air interface, especially in the solid-liquid contact region. The differences between the ACAs and RCAs in Fig. 5.6, i.e. the hysteresis values, are reported in Fig. 5.8, again as a function of the pillar height. All values corresponding to *composite* states belong to the same horizontal line, a clear demonstration

that the “non-forced” dynamic properties of drops in the *composite* states are independent of the height of the asperities on which they sit.

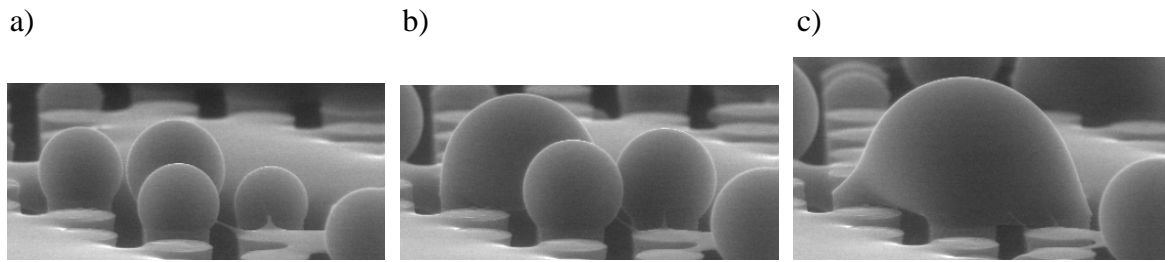


Fig. 5.7 Environmental scanning electron microscope images recorded during observation of a water condensation process on a rough surface with square disposition of 10- $\mu\text{m}$  diameter pillars and  $h = 40 \mu\text{m}$ ,  $p = 15 \mu\text{m}$ . The a) b) c) sequence represents the same small water drops during their growth process. In a) they lie on top-surfaces of single obstacles; in b) and c) they collapse into bigger *composite* drops, suspended partially on top-pillar surfaces and partially on flat liquid-gas menisci.

As for the values related to the only two observed *wetted* cases, it can reasonably be affirmed that they are aligned only because the difference in height of the pillars on the two related substrates is not great enough to show significant differences in the actual substrate area (i.e. in the Wenzel roughness factor  $r$ ), and consequently in the contact angles.

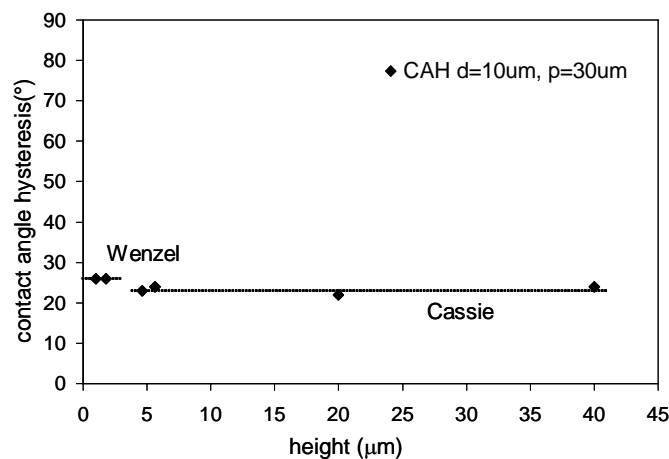


Fig. 5.8 Hysteresis values related to the DCA results shown in Fig. 5.6. The dashed lines serve as visual guides.

For the *wetted* regime, however, the contact angle hysteresis related to the asperity height increase is expected to augment. While the advancing contact angle should remain practically constant, the receding angle should decrease due to the augmented pinning phenomenon of the liquid among the taller asperities.

### Influence of pillar absolute size on Cassie-Wenzel transition

Several series of samples, each with a square disposition of cylindrical pillars with a specific diameter  $d$  and height  $h = 2d$ , are prepared in order to study the influence of asperity absolute size on the position of the Cassie-Wenzel transition. Five series of samples are prepared for five selected diameters (i.e.  $d = 3, 5, 10, 14,$  and  $20 \mu\text{m}$ ), each series composed of eight different pitches, the latter selected using the relations  $f = \frac{A\pi}{4} \left(\frac{d}{p}\right)^2$  and  $r = 1 + 2A\pi \left(\frac{d}{p}\right)^2$  in order to obtain the same series of  $r$  and  $f$  roughness factors.

Fig 5.9 shows a scheme explaining the criterion adopted to prepare these samples, referred to as “*scaling criterion*”, with details concerning pillar diameter, height and pitch of the prepared rough substrates.

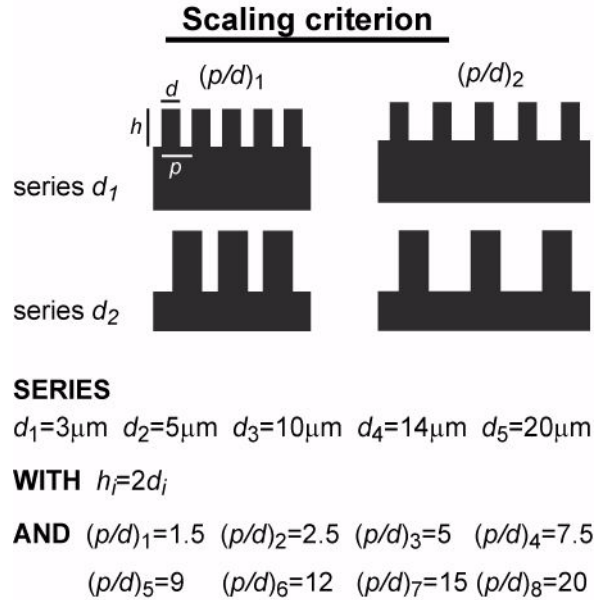


Fig. 5.9 “*Scaling criterion*”. Scheme illustrating the criterion adopted to prepare samples with different pillar absolute sizes in the micrometric range.

Both roughness factors ( $r$  and  $f$ ) were kept constant to enable Cassie and Wenzel theoretical models to predict precisely the same series of contact angle values for all five series. In Fig. 5.10 the experimental values of the  $p/d$  ratio where the Cassie-Wenzel transition takes place are reported as a function of pillar diameter, for both static and dynamic regimes. In particular, for each diameter, two  $p/d$  values are reported: one corresponding to “the last Cassie state”, and a second corresponding to “the first Wenzel state”, both observed in the direction of the pitch increase. Thus, full and empty symbols (circles for the static and squares for the

dynamic regimes) represent the limit where the Cassie-Wenzel transition has been observed, for static and dynamic measurements respectively.

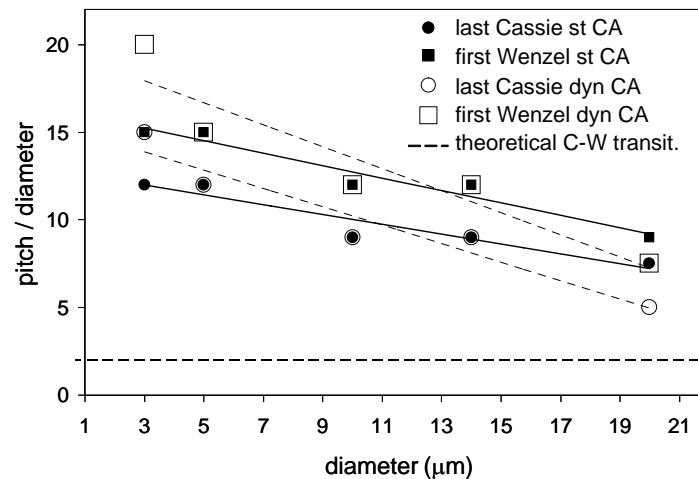


Fig. 5.10 Values of the  $p/d$  ratio delimiting the static and dynamic Cassie-Wenzel transition positions for different diameters ( $3\mu\text{m} \leq d \leq 20\mu\text{m}$ ). Linear trend-lines are reported simply to underline the differences in slope between static and dynamic wetting properties. The horizontal dashed line indicates the theoretical  $p/d$  value of the Cassie-Wenzel transition, identical for all the considered sample series.

The first observation is that in the considered micrometer range ( $3\mu\text{m} \leq d \leq 20\mu\text{m}$ ), reducing the absolute size of the model obstacle causes an improvement in both static and dynamic superhydrophobic properties, since the static and dynamic Cassie-Wenzel transition gaps fall at smaller surface asperity density (i.e. larger  $p/d$  ratio) than that predicted by theory. This is expressed by the negative slope of all the linear trend-lines added to the experimental values in Fig. 5.10, in contrast to the theoretical static transition point, unique for all considered series, corresponding to the intersection point between the Cassie and Wenzel curves [35] (see also “Theoretical background” paragraph in Chapter 4) and represented in Fig. 5.10 by the dashed horizontal line. The second main observation is that the trend-line associated with DCA measurements presents a more negative slope than the corresponding SCA line. In fact, in the studied range of  $d$ , the static and dynamic Cassie-Wenzel transitions are observed for the same  $p/d$  values (full and empty symbols are concentric) with the exception of the two extremes of the considered diameter size interval, i.e.  $d = 3\mu\text{m}$  and  $d = 20\mu\text{m}$ . For the largest diameter ( $d = 20\mu\text{m}$ ) the dynamic Cassie-Wenzel transition falls at smaller pitch than the static one; inversely, for the smallest diameter ( $d = 3\mu\text{m}$ ), it falls at larger pitch. The vertical shift in  $p/d$  observed comparing static and dynamic transition positions for



substrates with the same pillar size indicates a difference in the robustness of the metastable *composite* states delimiting the experimental Cassie-Wenzel transition. During dynamic measurements, although performed in a *quasi-stationary* regime, the less robust the system the greater the effect of the perturbations. On the surface with 3- $\mu\text{m}$  diameter pillars and  $p = 15d$ , the metastable *composite* regime is more robust than on the surface with 20- $\mu\text{m}$  diameter pillars and  $p = 7.5d$ , assuming that the perturbations induced by the dynamic measurements are comparable in both cases. This confirms the previous results (shown and discussed in Chapter 4) concerning SCA investigations on microstructured substrates. Moreover, the dynamic results presented here support the idea of an increase in stability and robustness of the *composite* states associated with reduced asperity size.

These experimental results represent a first step towards answering the essential question of defining the most convenient asperity size, corresponding to metastable *composite* superhydrophobic states of higher robustness.

Attempting to interpret the SCA and DCA results from a more phenomenological point of view leads us to focus more closely on the contact line, and the individual weight of its specific features, such as its length, fragmentation and corrugation. In particular, contact line can be defined differently, depending on the considered *composite* regime, whether static or dynamic. On the one hand, static *composite* drops involve a contact line that can be considered determined by the sum of the top-surface perimeter of all the pillars in contact with the drop at the drop-substrate interface, all of them participating in suspending the drop in the Cassie state. This contact line is referred to as stationary “total contact line”. On the other hand, dynamic *composite* drops, i.e. related to advancing and receding contact angle measurements, involve a contact line composed of the top-surface perimeter of only the pillars belonging to the perimeter of the drop-substrate interface, i.e. the external pillars. To be precise, it corresponds to the sum of the external fragments of the external pillar perimeters. This definition is based on the no-slip boundary condition of fluid mechanics, which, considering a liquid flow in contact with a solid surface, associates a zero velocity with the liquid molecules at the surface. Consequently, the movement of a water drop on a surface can be associated only with the motion of the water molecules belonging to the more external contact line. This is why this contact line is referred to as dynamic “external contact line”.

Fig. 5.11 shows the schematic representation of the contact line in both static and dynamic cases (i.e. “total” and “external” contact line definition).

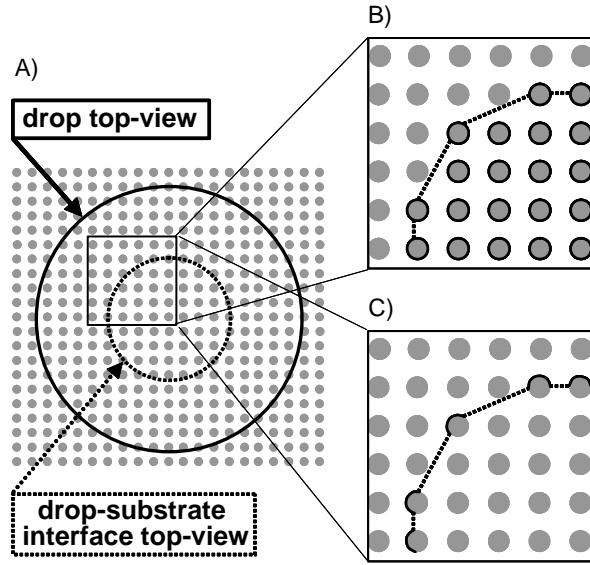


Fig. 5.11 Schematic representation of the contact line for a *composite* drop on a flat-top pillar-like periodically structured surface. A) Drop top-view; B) zoom of a portion of the “total” contact line at the drop-substrate interface, in the case of a static *composite* drop; C) zoom of the portion of the “external” contact line at the drop-substrate interface, in the case of a dynamic *composite* drop.

Based on such assumptions, we can approximately estimate the fragmentation and length of the contact line for one planar square millimeter of the structured substrate, in the two “total” and “external” configurations. The following are considered:

$$N_{\text{tot}} = \frac{A}{p^2} \quad (5.2)$$

$$CL_{\text{tot}} = L N_{\text{tot}} = L \frac{A}{p^2} \quad (5.3)$$

$$N_{\text{ext}} = \frac{A}{p} \quad (5.4)$$

$$CL_{\text{ext}} = \frac{L}{2} N_{\text{ext}} = \frac{LA}{2p} \quad (5.5)$$

where  $N_{\text{tot}}$  represents an approximate estimation of the number of pillars per unit area at the drop-substrate interface surface,  $CL_{\text{tot}}$  the corresponding “total” contact line length,  $N_{\text{ext}}$  the number of pillars at the drop-substrate interface perimeter, and  $CL_{\text{ext}}$  the corresponding “external” contact line length. Thus,  $N_{\text{tot}}$  and  $N_{\text{ext}}$  are equivalent to the number of contact line fragments for the “total” and the “external” contact lines, respectively.

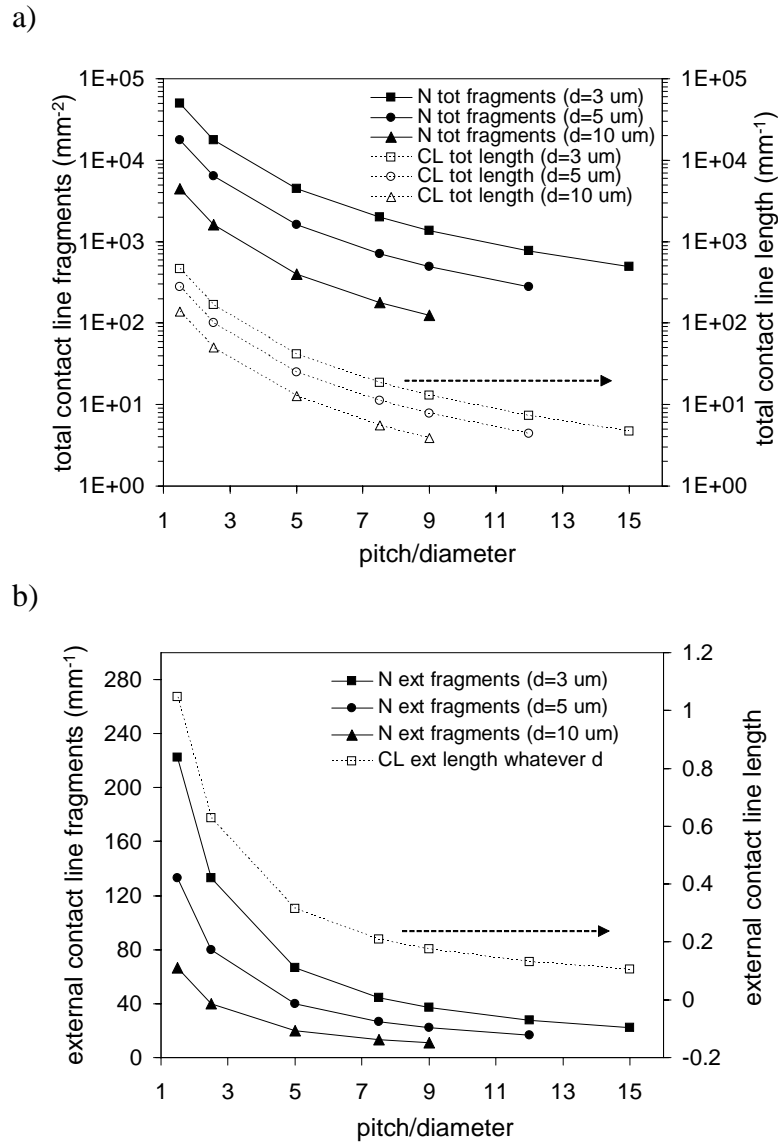


Fig. 5.12 *Contact line length and fragmentation.* Estimation of the contact line's main features with respect to the unit area ( $mm^2$ ), as function of the p/d ratio, for a *composite* drop in contact with microstructured surfaces where flat-top pillars of three different diameters ( $d = 3, 5, 10 \mu m$ ) are distributed in square arrangement ( $A=1$ ). a) "Total" contact line fragments  $N_{tot}$  and related total length  $CL_{tot}$ . b) "External" contact line fragments  $N_{ext}$  and related length  $CL_{ext}$ . It should be noted that for the "total contact line", both fragmentation and length increase when pillar diameter is decreased, as opposed to the "external contact line", which increases in fragmentation but stays constant in length, independently of pillar diameter.

In Fig. 5.12, fragmentation and length values are reported as a function of the p/d ratio, calculated respectively for the "total" and "external" contact lines ( $N_{tot}$  and  $CL_{tot}$  in Fig. 5.12-a, and  $N_{ext}$  and  $CL_{ext}$  in Fig. 5.12-b), for all the substrates with 3-, 5-, 10- $\mu m$  diameter pillars where water drops have assumed the Cassie state. Such estimations are of course based on several quite significant assumptions, mainly affecting the evaluation of the "external" contact

line features ( $N_{\text{ext}}$  and  $CL_{\text{ext}}$ ). These are: 1) the circularity of the macroscopic drop-substrate interface, rather than an irregular polygon whose sides in most cases are longer than the simple pitch; 2) the fact that the typical fragment of the contact line has been considered equivalent to half the pillar top-surface perimeter. Despite the approximate nature of the proposed calculations, the obtained results appear to be sufficiently well founded to permit a qualitative discussion of the previously shown experimental results. For such a discussion, the graphs in Fig. 5.10 and Fig. 5.12-a-b, together with the experimental results summarized in Table 1, have to be considered. In the latter, the observed “last Cassie” and “first Wenzel” states delimiting the Cassie-Wenzel transition are reported in terms of pitch  $p$ ,  $p/d$  ratio and  $f$  roughness parameter, for both static and dynamic measurements.

d	Static measurements						Dynamic measurements						
	p LC	p FW	p/d LC	p/d FW	f LC	f FW	p LC	p FW	p/d LC	p/d FW	f LC	f FW	LC $\Delta\theta$
3	36	45	12	15	0.0055	0.0035	45	60	15	20	0.0035	0.0020	2
5	60	75	12	15	0.0055	0.0035	60	75	12	15	0.0055	0.0035	4
10	90	120	9	12	0.0097	0.0055	90	120	9	12	0.0097	0.0055	4
14	126	168	9	12	0.0097	0.0055	126	168	9	12	0.0097	0.0055	10
20	150	180	7.5	9	0.0140	0.0097	100	150	5	7.5	0.0317	0.014	15

Table 5.1 Cassie-Wenzel transition positions evidenced by the “scaling experiments” for different pillar sizes, in both static and dynamic cases.

The  $p$ ,  $p/d$  and  $f$  values delimiting the Cassie-Wenzel transition region are reported for each considered sample series (i.e. one for each pillar diameter  $d$ ). “LC” and “FW” designate “last Cassie state” and “first Wenzel state” respectively, observed by measuring the contact angle as function of pitch increase. “LC  $\Delta\theta$ ” designates the hysteresis of the last Cassie state.

As already discussed, the negative slopes of all trend-lines shown in Fig. 5.10 exemplify the main observation made above regarding the increased extent of the superhydrophobic *composite* regime that occurs when asperity size is reduced, for both static and dynamic cases. This means that for smaller model asperities, a lower fraction  $f$  of solid-liquid contact at the drop-substrate interface is able to support the drop in the *composite* state. Referring to Fig. 5.12-a, regarding in particular the *composite* static regime, it may be noted that for a specific  $p/d$  ratio value, (i.e., same  $f$  value) the “total contact line” is estimated as being longer and more fragmented for smaller asperity sizes. For example, for  $p/d = 7.5$ , passing from a surface with

square distribution of 3- $\mu\text{m}$  diameter pillars to one with 10- $\mu\text{m}$  diameter pillars, fragment number per unit area  $N_{\text{tot}}$  and contact line length per unit area  $CL_{\text{tot}}$  vary considerably, ranging from  $N_{\text{tot}} \sim 1975 \text{ mm}^{-2}$  to  $\sim 177 \text{ mm}^{-2}$ , and from  $CL_{\text{tot}} \sim 19 \text{ mm}^{-1}$  to  $\sim 6 \text{ mm}^{-1}$  respectively.

With regard to the enhanced robustness of *composite* states obtained by decreasing asperity size, represented in Fig. 5.10 by the more negative slope of the lines associated with the dynamic measurements, reference is made to Fig. 5.12-b. A general increase in the “external contact line” fragment number  $N_{\text{ext}}$  can again be associated with a decrease in pillar diameter at any precise  $p/d$  ratio value, but in contrast to the static case, estimation of contact line length  $CL_{\text{ext}}$  for different pillar diameters produces a unique curve, i.e. the same series of values for the same series of  $p/d$  ratios. In particular, focusing on the three different  $p/d$  values, associated with the last dynamic Cassie states observed in the direction of the pitch increase for the three different diameters considered (i.e.  $d = 3, 5, 10 \mu\text{m}$  corresponding respectively to  $p/d = 9, 12, 15$ ), it can be noted that the “external contact line” decreases in length  $CL_{\text{ext}}$  but increases in fragment number  $N_{\text{ext}}$ . In other words, by reducing model asperity size, *composite* states suspended on a shorter but more fragmented contact line are obtained. Despite the significant level of approximation relating to the proposed estimations of “external contact line” fragmentation and length, especially overestimated in the case of large pitches (where drops sit on a small number of pillars), it may be concluded that the fragmentation of the contact line at the drop-substrate interface (which is clearly associated with a similarly fragmented liquid-solid contact surface) should be the most relevant factor influencing the relative stability of the dynamic *composite* states observed at the minimum allowed asperity surface density (i.e. for larger  $p/d$  values). For asperities of smaller pillar diameter, the last dynamic *composite* state observed in the direction of the pitch increase is related to a possibly shorter but especially more fragmented external contact line, and consequently a shorter length of each contact line fragment. Such contact line characteristics should facilitate its motion because 1) a shorter contact line would be related to a lower total line tension, and 2) a more fragmented contact line would present lower energy barriers between its consecutive positions.

The  $f$  value corresponding to the last dynamic *composite* state recorded for the minimum considered pillar diameter  $d = 3 \mu\text{m}$  (i.e.  $f \sim 0.0035$ , in Table 1) represents the lowest  $f$  value ever reported for flat-top structured surfaces able to suspend dynamic *composite* drops and associated with an extremely low hysteresis value ( $\Delta\theta = 2^\circ$ , in Table 1).

Regarding the hysteresis phenomenon related to variation of asperity absolute size, reference can be made to Fig. 5.13, where the hysteresis values for all the *composite* states observed during the “scaling experiments” are reported.

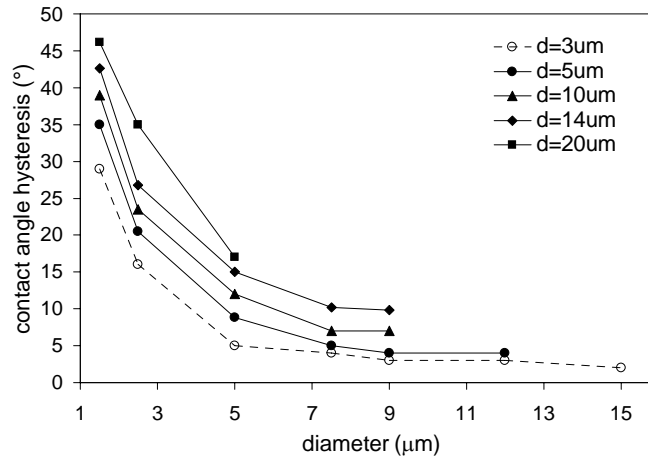


Fig. 5.13 *Scaling effect on hysteresis of composite states.* The hysteresis values recorded for all the *composite* states observed with the “scaling experiments” are reported as a function of  $p/d$  ratio. It should be noted that when the size of the model obstacle is reduced, *composite* states are observed for larger  $p/d$  values, and related hysteresis values decrease.

The tendency for hysteresis to diminish more rapidly with asperity absolute size and pitch increase is evident and is further proof of the influence of contact line fragmentation on the extent and robustness increase of metastable *composite* states observed when the asperity size is decreased.

If the measured contact angle hysteresis values are plotted as a function of estimated number of fragments  $N_{\text{ext}}$  and length  $CL_{\text{ext}}$  of the external contact line for the observed *composite* states, the graphs shown in Fig. 5.14 (a and b) are obtained.

Both graphs validate the remarks previously made concerning the fundamental influence of contact line fragmentation on improved superhydrophobic properties (associated with a decrease in CAH), observed when asperity absolute size is reduced.

In Fig. 5.14-a, comparison of the minima hysteresis values obtained for all the reported sample series (one for each pillar diameter) shows that the absolute minimum corresponds to the surface with the maximum number of external contact line fragments per unit surface  $N_{\text{ext}}$ . On the other hand, Fig. 5.14-b shows that for each sample series, the related hysteresis minimum is lower for a shorter external contact line length  $CL_{\text{ext}}$ .

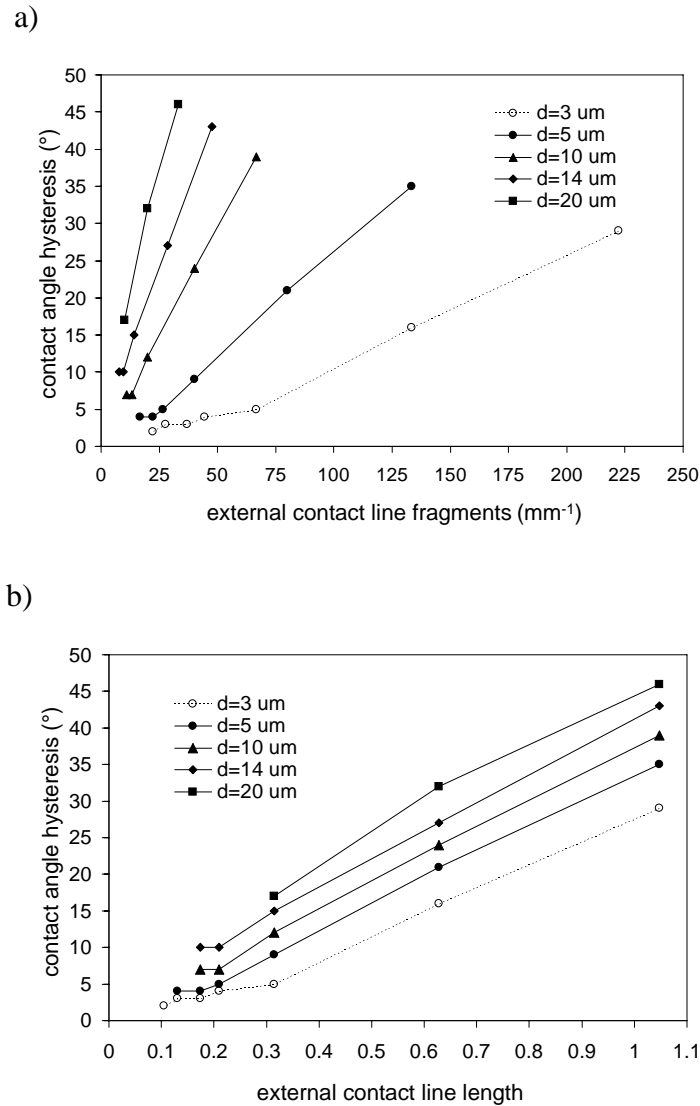


Fig. 5.14 CAH values of *composite* states observed in scaling experiments, as a function of estimated number of fragments  $N_{\text{ext}}$  (a), and length  $CL_{\text{ext}}$  (b) of the “external contact line”.

Summarizing, it can be concluded that for the same “external” contact line length (Fig. 5.14-b), the decreased hysteresis observed when asperity size is reduced is caused by an increase in its fragmentation (Fig. 5.14-a) and the related reduction of each individual fragment length. In other words, reducing the size of the model asperity allows metastable *composite* states to be achieved for smaller  $f$  values, and in parallel decreases the related hysteresis values.

Based on the experimental results already presented and discussed, the principle of improved superhydrophobicity associated with the decrease in asperity absolute size can certainly be considered valid for surfaces with a roughness in a micrometric range.

In this context, the questions that spontaneously arise are: 1) Can  $f$  values corresponding to *composite* states be significantly reduced below 0.0035 by further “shrinking” of the model obstacle? 2) If so, how does the tendency displayed in Fig. 5.10 evolve when model obstacle size is reduced? 3) At which lower and upper asperity size limits does significant superhydrophobicity occur?

New series of appropriate experiments would obviously be helpful in answering these questions, but based on the presented results on microstructured substrates, and with the help of new results obtained on nanostructured substrates, possible answers are suggested in the next section.

### **Superhydrophobicity: a macroscopic property of micro- and nano-meter structures**

With regard to the asperity size upper limit at which superhydrophobicity occurs, Fig. 5.10 may be reconsidered, and an extension of the ideal straight line between the two continuous lines representing the static Cassie-Wenzel transition may be imagined, until it intersects the  $x$  axes (in the graph corresponding to  $p/d = 1$ ). Such an intersection point can be interpreted with good approximation as the asperity size upper limit where the term superhydrophobicity, as used until now (i.e. associated with rough surfaces with contact angle larger than  $150^\circ$  and low hysteresis), no longer has any sense. Such intersection would in fact correspond to the rough surface where asperity size equals the spacing between consecutive asperities, and consequently where only the *wetted* regime is possible.

These arguments are in good agreement with the experimental results of Oner and McCarthy [37], Yoshimitsu et al. [44], and Nakae et al. [34]. The proposition of Oner and McCarthy to consider  $32\ \mu\text{m}$  as the maximum length scale of roughness imparting superhydrophobicity for surfaces consisting of periodically distributed posts is especially confirmed here. Their experiments performed varying the asperity size  $x$  between 2 and  $128\ \mu\text{m}$ , keeping constant the spacing  $p = 2x$  between consecutive asperities, and height  $h = 40\ \mu\text{m}$ , show the Cassie-Wenzel transition comprised between 32- and  $64\text{-}\mu\text{m}$  asperity size, and the *wetted* regime related to  $64\text{-}\mu\text{m}$  side asperities characterized by a much lower ACA than that observed for smaller asperity sizes, and a much higher CAH value.

Regarding the asperity size lower limit where superhydrophobicity should vanish, two cases should be distinguished: one associating the minimum asperity size suspending



*composite* drops with an  $f$  roughness factor comparable to that evidenced by this work in the micrometric range, and another associating the minimum asperity size with the absolute minimum  $f$  corresponding to *composite* drops. Returning to Table 1, and the  $f$  values delimiting the observed Cassie-Wenzel transitions for different pillar size in the micrometric range: as already emphasized, the minimum  $f$  value of  $\sim 0.0035$ , still associated with *composite* states for square distribution of 3- $\mu\text{m}$  diameter pillars, corresponds to an actual solid-liquid contact at the macroscopic drop-substrate interface equal to 0.6%! Is it really reasonable to hypothesize that such a value can be further reduced by reducing the size of asperities? More concretely: for example, to reduce  $f$  by an order of magnitude (i.e. 0.0004), 100-nm diameter pillars (i.e. pillars 10 times smaller than those considered in this work) should be spaced of approximately 40 times their pillar size. This seems quite improbable, and the preliminary static and DCA results on nanostructured surfaces (prepared by the method described in reference [195]) confirm this (see Fig. 5.15).

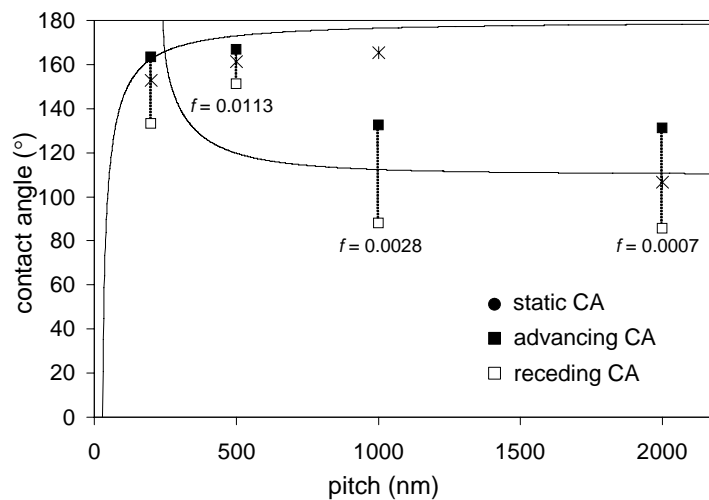


Fig. 5.15 *Pitch influence on nanostructured surfaces.* SCA and DCA values measured on samples with square disposition ( $A = 1$ ) of square pillars (side = 60 nm,  $h = 600$  nm) as a function of pitch, and comparison with Wenzel and Cassie models (decreasing and increasing curve, respectively). Values of  $f$  are reported for pitches where static and dynamic Cassie-Wenzel transitions are observed. The dashed vertical lines show hysteresis values.

The  $f$  range corresponding to the dynamic Cassie-Wenzel transition evidenced for square disposition ( $A = 1$ ) of square pillars with  $\sim 60$ -nm side,  $\sim 600$ -nm height (see Fig. 5.16, where as examples, SEM images of two substrates at different pitch are reported), is delimited from the values  $f_{\text{last Cassie}} = 0.011$  and  $f_{\text{first Wenzel}} = 0.0028$ . This  $f$  range, although quite broad (due to the limited number of considered pitches  $p = 200, 500, 1000, 2000$  nm), and although

obtained on surfaces not precisely fulfilling all the requirements of the previously presented “scaling experiment”, excludes that a further significant asperity size “shrinking” can be associated with a limit *composite f* value lower than 0.0035, evidenced by the experiments in the micrometric range.

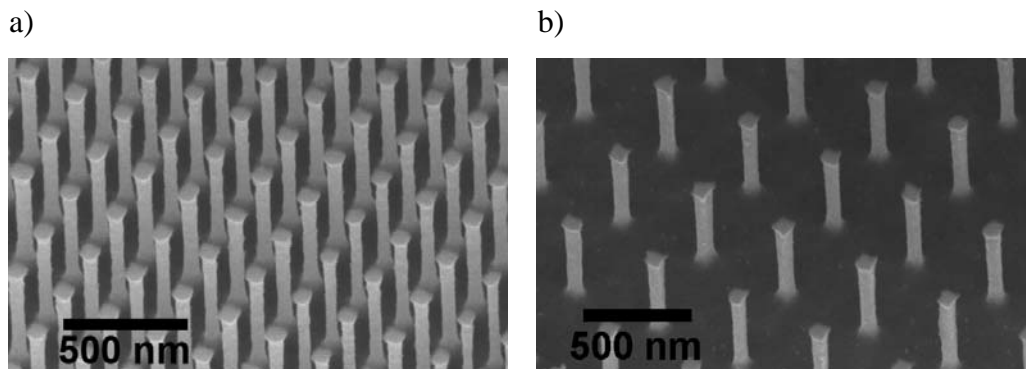


Fig. 5.16 *Nanostructured substrates.* Tilted scanning electron microscopy images ( $38.5^\circ$  tilt angle) of two nanostructured substrates where square pillars of  $\sim 60$ -nm width,  $\sim 600$ -nm height, are distributed in square arrangement: a) substrate at pitch  $\sim 200$  nm; b) substrate at pitch  $\sim 500$  nm.

Looking at Fig. 5.15, it should be noted that the Cassie-Wenzel transition observed for dynamic measurements falls at a shorter pitch than that for the static measurements, in contrast to the results obtained for the series with cylindrical pillars of  $3\text{-}\mu\text{m}$  diameter. This result is assumed to be due to the very low energy barrier between the metastable Cassie state associated with  $p = 1000$  nm and the favored Wenzel state. The unavoidable perturbation associated with the dynamic measurement process is effective in obtaining the thermodynamically stable *wetted* state. This observation is also supported by the thermodynamic model presented in Chapter 4 applied to this case.

In Fig. 5.17, the energy barriers between the Cassie and Wenzel states estimated by the developed model (see Chapter 4 for details) are represented as a function of the  $p/d$  ratio, for the sample series with square distribution of cylindrical pillars with  $10\text{-}\mu\text{m}$  diameter and  $20\text{-}\mu\text{m}$  height (considered as reference in the micrometer range), and compared to the series of nanostructured samples described above. It is immediately clear that the experimental transition ranges for the two sample series, delimited by the two pairs of vertical lines, fall very close, while the minima related to the theoretical transition in the two cases (represented by the crosses) are significantly far apart. In particular, in contrast to the good agreement between theoretical prediction (black cross) and experiments (black vertical dashed lines) in the micrometric range, for the nanostructures the experimental transition is observed for a much

smaller  $p/d$  value (gray vertical dashed lines) than the value where the energy barrier minimum falls (gray cross).

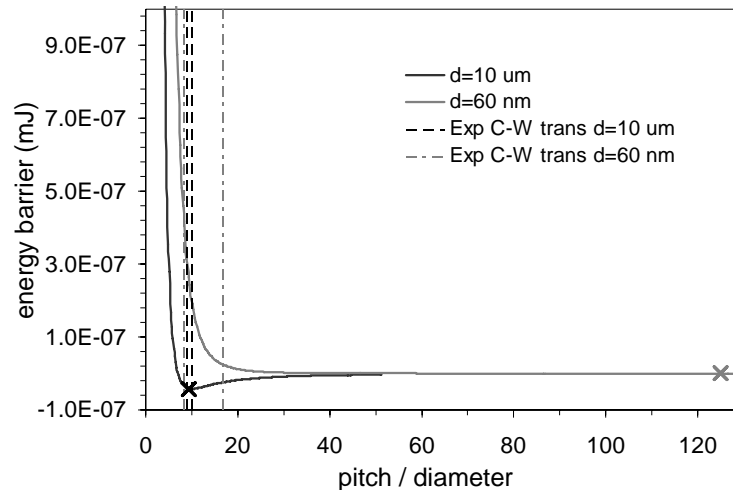


Fig. 5.17 Energy barrier for two selected sample series: one corresponding to square surface distribution of cylindrical pillars with 10- $\mu\text{m}$  diameter (20- $\mu\text{m}$  height), and the second corresponding to square surface distribution of square posts with 60-nm side (600-nm height), as a function of the pitch/diameter ratio. The minima of the two theoretical curves are represented by the crosses, and the two pairs of vertical lines delimit the ranges of the observed experimental C-W transitions.

This supports the idea that the micrometer range is definitely the one presenting the maximum extent of the *composite* Cassie states (i.e. *composite* states at lower  $f$  values), and consequently, the most convenient for designing superhydrophobic surfaces.

Recent literature shows that surfaces with periodic [6][196] or random [76][197]-[199] nanometer roughness present *composite* superhydrophobic states. But none of these contributions present any systematic study that shows either how dense nanometric asperities have to be in order to steadily support water drops in the *composite* state, or the limit of asperity surface density where the Cassie-Wenzel transition occurs. It is not surprising that the rough surfaces considered in such contributions all present *composite* superhydrophobic wetting properties, since the  $f$  value roughly estimated for all cases is never lower than 0.01. The low hysteresis measured on such surfaces, and the stability of the observed *composite* states, would simply be the effects of increased contact line fragmentation.

### Influence of pillar top-surface perimeter on Cassie-Wenzel transition

In order to systematically investigate the influence of contact line length and corrugation on the Cassie-Wenzel transition position, DCA measurements were performed on series of samples with square distribution ( $A = 1$ ) of obstacles, constant height and asperity top-surface area ( $h = 40 \mu\text{m}$  and  $s = 78.5 \mu\text{m}^2$ , that is the same as of 10- $\mu\text{m}$  diameter cylindrical post) but different obstacle section shape, and thus different top-surface perimeter  $L$  (Fig. 5.18).

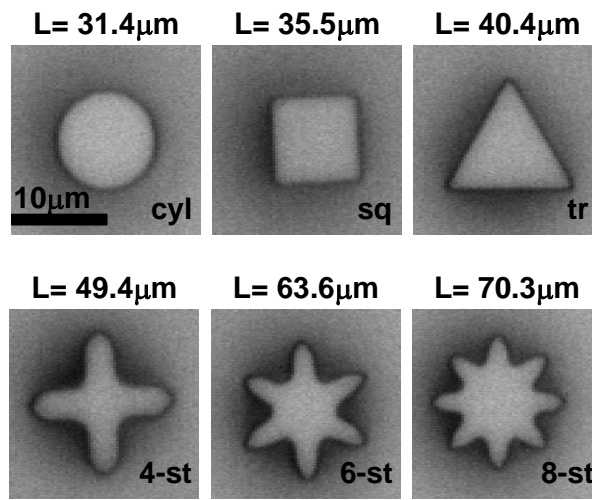


Fig. 5.18 Optical microscope images of the different top-pillar surface shapes (i.e. circle, square, triangle, 4-edged star, 6-edged star, 8-edged star), with corresponding perimeter lengths  $L$  ( $h = 40 \mu\text{m}$ ).

The first series of DCA measurements was performed on 18 samples, corresponding to the selected six obstacle shapes, for three different pitches ( $p = 100 \mu\text{m}$ ,  $110 \mu\text{m}$ , and  $120 \mu\text{m}$ ), chosen around the Cassie-Wenzel transition range observed for square distribution of cylindrical pillars (see Fig. 4.5). Since all measurements showed *wetted* states, Fig. 5.19 simply reports the static and DCA values related to the series with the smallest pitch ( $p = 100 \mu\text{m}$ ), and only the static values related to the series with the intermediate pitch ( $p = 110 \mu\text{m}$ ), the one where SCA measurements presented the Cassie-Wenzel transition (see Fig. 4.18).

To discuss the results of Fig. 5.19, Fig. 5.2 must be recalled, where SCA and DCA values are reported as a function of pitch for square distributions of 10- $\mu\text{m}$  diameter cylinders. In such a case, the exerted extra-pressure of  $\sim 300 \text{ Pa}$  proved sufficient to show the metastability of the last observed static Cassie state, i.e. the one with pitch  $p = 100 \mu\text{m}$ . This is why it is not surprising that all dynamic measurements performed on differently shaped pillars with pitch  $p \geq 100 \mu\text{m}$  similarly evidenced only *wetted* states.

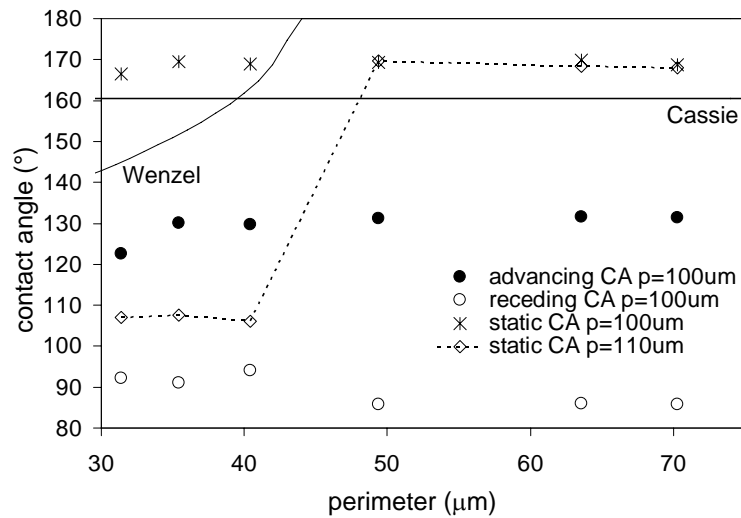


Fig. 5.19 Influence of the obstacle top-surface perimeter on DCAs. Contact angle values measured on square distribution ( $A = 1$ ) of obstacles presenting the same top-surface area ( $s = 78,5 \mu\text{m}^2$ ), the same height ( $h = 40 \mu\text{m}$ ), but different top-surface perimeter  $L$ . SCA and DCA values are reported for pitch  $p = 100 \mu\text{m}$ , while only SCA values are reported for  $p = 110 \mu\text{m}$ .

In particular, since no significant difference was shown by dynamic measurements on different pitch series, only the dynamic results related to the smallest pitch are reported. The latter correspond to the pitch where all SCA values as a function of  $L$  showed *composite* states. Such values are reported in Fig. 5.19 for comparison with the corresponding dynamic *wetted* cases, and to the SCA values related to the pitch  $p = 110 \mu\text{m}$ , which is the one where the static Cassie-Wenzel transition was observed.

In line with the presentation of the results obtained for all previously considered cases, the CAH values corresponding to the advancing and RCAs in Fig. 5.19 are represented in Fig. 5.20. Such results again demonstrate that the hysteresis of Wenzel *wetted* states depend on the actual area of the considered rough surfaces. Increasing the perimeter of the obstacle top-surface, keeping constant the top-surface area, increases Wenzel roughness ratio  $r$ , by an increased contribution of the obstacle's lateral surface to the total area of the rough surface.

As already mentioned when discussing the hysteresis tendency observed as a function of the pitch increase (see Fig. 5.3), the liquid pinning at the asperities, associated with the motion of a drop in the *wetted* state, is more significant compared to the *composite* regimes, since it involves a continuous “external three-phase contact line”, which has to follow the whole contour of all the asperities in the three space directions.

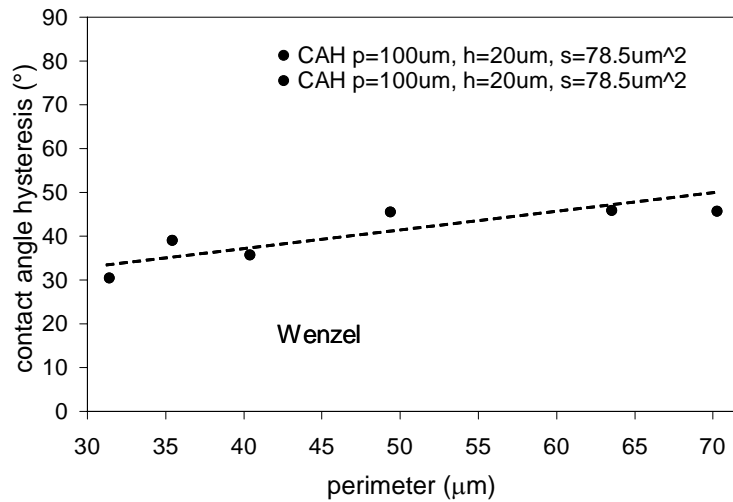


Fig. 5.20 Hysteresis values related to the sample series with different obstacle top-surface perimeter  $L$  and pitch  $p = 100 \mu\text{m}$  (from Fig. 5.18).

The hysteresis increase recorded with the perimeter increase for drops in the *wetted* state presumably derives from the increase in contact line length and corrugation, which can be considered a direct consequence of the increased contribution to the actual surface area of the augmented obstacle lateral surface area.

The second series of experiments involves dynamic measurements performed on two series of samples, corresponding to two pitches ( $p = 30 \mu\text{m}$  and  $70 \mu\text{m}$ ) belonging to the region where static and dynamic measurements on square disposition of  $10\text{-}\mu\text{m}$  diameter cylinders present the *composite* states. In this case, there are only four considered obstacle top-surface shapes (i.e. cyl, tr, 6-edged star, 8-edged star).

The following were expected to be recorded: 1) a significant hysteresis increase, caused by increasing the asperity top-surface perimeter, due to an augmented pinning especially during the water withdrawing process for the related contact line corrugation increment (based on the interpretations proposed by Oner and McCarthy [37]); and 2) an hysteresis decrease, caused by increasing the spacing between consecutive pillars, based on what had hitherto been observed for cylindrical pillars (Fig. 5.3 and Fig. 5.13).

Conversely to what was expected, the measured DCAs (reported in Fig. 5.21 as a function of obstacle top-surface perimeter) do not display any really significant tendency. In fact, only the expected hysteresis decrease with the pitch increase was observed (in Fig. 5.21 the hysteresis curve related to  $p = 70 \mu\text{m}$  is always lower than that related to  $p = 30 \mu\text{m}$ ).

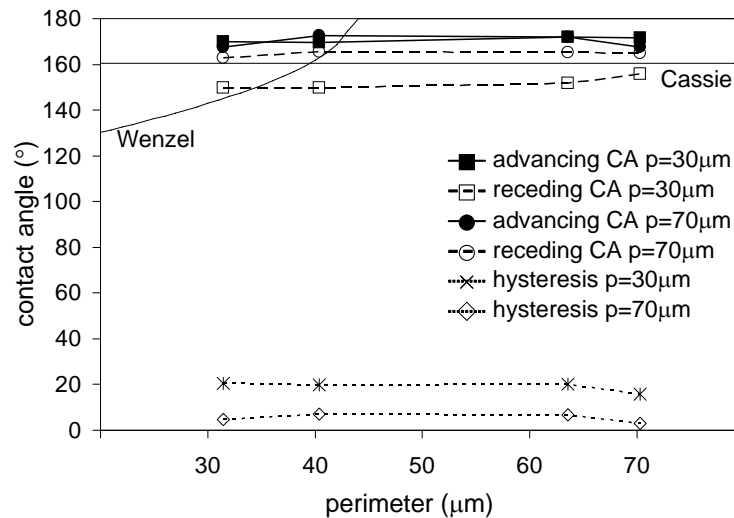


Fig. 5.21 Water ACA and RCA values plotted as a function of different obstacle top-surface perimeters for two different pitches ( $p = 30$  and  $70 \mu\text{m}$ ). The hysteresis values are also reported (lower part of graph). All points represent drops in *composite* state, as can be derived by the reported theoretical Cassie and Wenzel curves.

On the other hand, the slightly decreasing hysteresis recorded for both pitches, increasing the asperity top-surface perimeter, actually contradicts the supposed tendency. The analyzed structured surfaces present the same constant asperity top-surface and same level of fragmentation for the same pitch, but different contact line corrugations and different lengths for each fragment. The small differences in contact angle values, measured on substrates with the same pitch but different asperity perimeter, suggest that the contact line length of each specific fragment, and its corrugation, are second-order effects on the wetting properties of structured surfaces. These probably result in differences comprised in the error usually associated with contact angle measurements. The aim here was not to observe possible shifts in the Cassie-Wenzel transition position, but significant tendencies in contact angle values. In fact, the presented dynamic results show the effective secondary importance of the analyzed parameter, in contrast to the SCA measurements presented in Chapter 4, where a significant influence of the contact line fragment length and corrugation on the static Cassie-Wenzel transition position is documented.

### 5.3 Conclusions

In this chapter, wetting properties of superhydrophobic surfaces with a periodic controlled roughness in the micrometer range are studied as a function of different geometrical roughness parameters, by water SCA, ACA and RCA measurements, in the presence of a negligible extra-pressure acting on the drop-substrate system.

Comparison of the positions of the Cassie-Wenzel transition (i.e. transition from the *composite* state to the *wetted* Wenzel state) shown by SCA and DCA measurements confirms the validity of the model developed in Chapter 4 proposed for predicting the transition observed by the static measurements. In particular, all the observed dynamic transitions fall at a value of the selected geometrical parameter that either coincides with or is slightly different from that corresponding to the static transition. This shows how the  $\sim 300$  Pa exerted on the drop-substrate system by the adopted dynamic measurement technique can in some cases be sufficient to transform the static metastable *composite* state at lower stability into the corresponding favored *wetted* state.

The CAH values have also been discussed, analyzing the associated experimental *wetted* or *composite* states in relation to the studied geometrical parameter.

Dynamic wetting measurements as a function of asperity height confirmed the very large radius of curvature of the liquid-air menisci among the asperities for *composite* drops, proposed in Chapter 4, together with the assumption of no partial liquid penetration. They also the idea of discussing the experimental occurrence of *composite* states, and their transition to *wetted* states, preferably in terms of the contact surface at the drop-substrate interface, and especially of the related two dimensional contact line, since no significant external force is active on the considered drop-substrate system.

The static and dynamic wetting studies, performed as a function of absolute asperity size, clearly showed that reducing the size of the model obstacle firstly improves the extent of superhydrophobic *composite* states, allowing them to be obtained for smaller  $f$  factors, and secondly increases their robustness, shifting the dynamic Cassie-Wenzel transition to an even lower  $f$  value than the static transition. The proposed qualitative interpretation of such results, and of the deduced hysteresis tendencies, mainly considers the effects of different three-phase contact line features, such as its length and fragmentation. In particular, 1) the reduced contact line length and its augmented fragmentation are indicated as the most important factors in determining the extent at low  $f$  values of stationary Cassie states, decreasing pillar size; 2) the



increased fragmentation for smaller asperities is referred to as the essential factor in reducing the associated hysteresis, improving the related dynamic superhydrophobic, self-cleaning properties of rough surfaces.

Length and corrugation of the single fragment are shown to be parameters of second-order effect on dynamic *composite* superhydrophobic phenomena, by the dynamic wetting measurements performed on structured surfaces differing only in the length and shape of the asperity top-surface perimeter, keeping constant its area and asperity surface density.

Based on of preliminary wetting results obtained on superhydrophobic nanostructured substrates (briefly described in the text), the minimum  $f$  value of 0.0035, associated with *composite* states recorded for square distribution of 3- $\mu\text{m}$  diameter pillars, is proposed as the absolute minimum  $f$  factor at which the *composite* Cassie regime presents its maximum extent. Additionally, this suggests that, for surfaces consisting of periodically distributed pillars, the length scale comprised between several hundred nanometers and one micrometer can be considered as the most suitable asperity size imparting superhydrophobicity.



---

## 6 Superhydrophobicity: Adv- and Rec-CA investigations with a NON-negligible extra-pressure

*This chapter presents the results of advancing and receding contact angle (in the title referred to as “Adv- and Rec-CA” for brevity) measurements performed on structured hydrophobic substrates, consisting of perfluorosilanized regularly distributed flat-top pillars, for selected samples series. These dynamic contact angle measurements are conducted exerting a NON-negligible extra-pressure on the drop-substrate system. The obtained results are compared to those presented in Chapter 5 (where the exerted extra-pressure was negligible), and the validity of the classic Wenzel and Cassie models for predicting the wetting properties of hydrophobic rough surfaces is again demonstrated. Static and dynamic contact angle investigations are performed on the reference microstructured sample series (square distribution of 10- $\mu\text{m}$  diameter pillars, 40- $\mu\text{m}$  height, varying pitch) also using a wetting liquid (n-hexadecane), rather than water. The obtained results are presented in terms of the classic theories, and some interesting elements of discussion are suggested<sup>1</sup>.*

### 6.1 Measuring dynamic contact angles with a NON-negligible extra-pressure

The apparatus is the same as that described as in Chapter 4 and used for all contact angle investigations in this work. The main difference with respect to the method adopted in Chapter 5 (i.e. with a negligible extra-pressure acting on the drop-substrate system) is the distance between the substrate and the needle apex, before and during the complete process of drop volume increase and decrease, necessary for measuring advancing and receding contact angles (i.e. the “dynamic contact angles”, as referred above). In this case, the stainless steel needle (500- $\mu\text{m}$  external diameter) is kept at a distance of  $\sim 100 \mu\text{m}$  from the sample surface (see Fig. 6.1), instead of  $\sim 1 \text{ mm}$  (see Fig. 6.2). Also in this case, the water drop is formed at the needle apex by turning the micrometric screw directly connected to the syringe piston. The drop size

1. A scientific article presenting the results discussed in this chapter is in preparation.

is increased to a maximum of 7  $\mu\text{L}$  by further turning the screw, while turning in the opposite direction decreases drop size again. Both processes are carried out manually, and the estimated speed is comprised between 0.6 and 0.8  $\mu\text{L}/\text{sec}$ . In this case, the video begins with the sequence preceding that where the drop-substrate contact occurs. As soon as the drop is formed, each frame where the drop volume increases corresponds to the advancing contact angle, while the contact angle formed during the liquid withdrawing, from the moment when the drop base starts to decrease, represents the receding angle. All the advancing and receding contact angle values reported in this chapter correspond to the average of at least five measurements performed on at least five frames recorded during the drop volume increase and decrease, respectively. Contrary to the method referred to in Chapter 5, here the initial phase of the drop formation at the needle apex is the really crucial point of the whole process. As shown in image 2 of Fig. 6.1, the first phase of the liquid supplying with the needle close to the substrate has the effect of squeezing the small drop between needle and substrate.

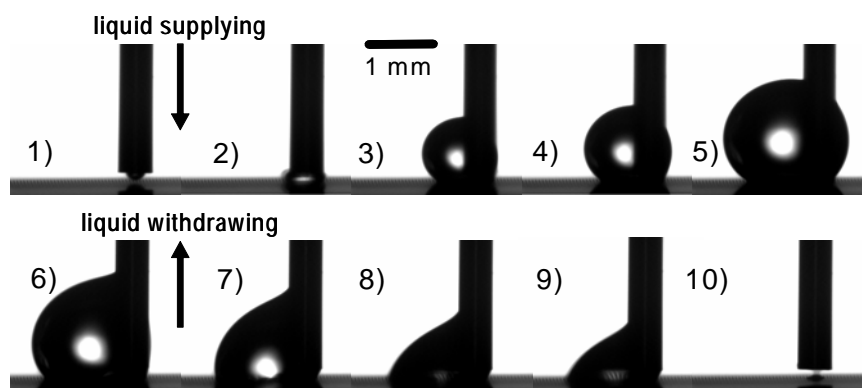


Fig. 6.1 *Dynamic measurements “with a NON-negligible extra-pressure” exerted on drop-substrate system. Image sequence selected from a typical video of advancing and receding contact angle measurements performed using the sessile drop method. Each video is usually composed of 200 frames taken with at an acquisition rate of 25 frames/sec). The selected configuration presents a needle-substrate distance  $\sim 100 \mu\text{m}$ . The images relate to a square distribution of cylindrical pillars with  $d = 10 \mu\text{m}$ ,  $h = 40 \mu\text{m}$ ,  $p = 50 \mu\text{m}$ .*

As already proposed in Chapter 5, the extra-pressure applied on the system at the moment of the drop-substrate contact can be approximately estimated by the Laplace equation  $\Delta P = 2\gamma_{LV}|\cos\theta'|/x$ , where  $|\cos\theta'|$  is the contact angle formed by the drop at this moment, and  $x$  is half the distance between needle apex and substrate [47]. With a needle-substrate distance of  $\sim 100 \mu\text{m}$ , and an overestimated contact angle of  $180^\circ$ , an overestimated extra-pressure of  $\sim 3 \text{ kPa}$  is obtained (corresponding to  $\sim 30 \text{ cm}$  of water). As will be discussed when

the experimental results obtained by this method are presented, such a pressure can definitely be considered “NON-negligible”, since it is sufficient to show significant differences in relation to static measurements, and dynamic measurements “with a negligible extra-pressure” (see Fig. 6.2).

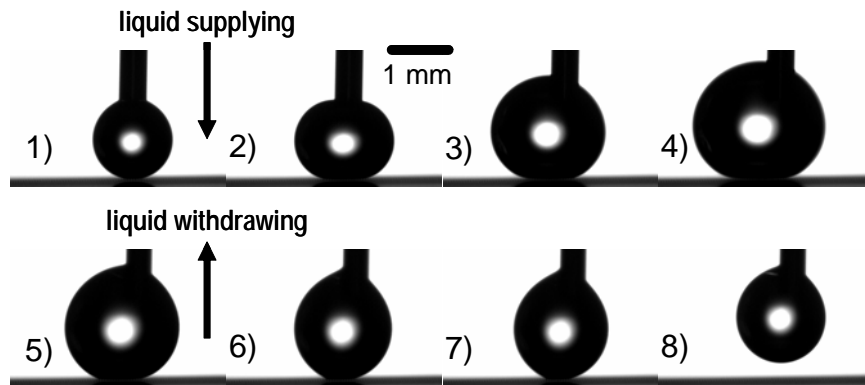


Fig. 6.2 *Dynamic measurements “with a negligible extra-pressure” exerted on drop-substrate system. The only difference in relation to the case in Fig. 6.1 is the needle-substrate distance of  $\sim 1$  mm. The image relates to the same substrate as that in Fig. 6.1*

Fig. 6.2 (see Chapter 5) is shown here once again for easy comparison of the two dynamic contact angle measurement methods used in this systematic study. Performing the measurements in both configurations on each substrate allowed the experimental identification of all substrates where the Cassie regime is metastable, i.e. the range of the considered roughness parameters where both *composite* and *wetted* regimes are observable depending on the extra-pressure applied.

## 6.2 Introduction

Several researchers have dealt with the question of defining the robustness of superhydrophobic composite states, as shown by their recent publications [47][50][51][55][93][95][200]. In such contributions, they focus on the Cassie-Wenzel transition, and propose criteria for defining its features as a function of the surface’s geometrical roughness characteristics. However, the experimental validation of such methods still seems inadequate. The model recently developed by Extrand [95] is based on the assumption, already proposed several decades ago [18], that for surfaces to suspend liquids (and exhibit super-repellency) the liquid surface tension acting around the perimeter of the asperities must create a “suspension pressure” greater than, or equal to, any downward directed hydrostatic pressure. As in his

previous contributions [42][55], he focuses on the role of the contact line linear fraction lying on the asperity edges. In conclusion he suggests that the most effective way of minimizing suspension pressure is the simultaneous decrease of asperity size and spacing. The practical cases indicated do not however correspond to really effective experimental proof.

Zheng [200] on the other hand presents the results of numerical simulation of the Cassie-Wenzel transition process when driven by a hydraulic pressure increase. He proposes a simple form of the maximum pressure sustainable from a pillar-like surface as a function of the geometrical characteristics of the rough surface. His method is compared only with the experimental results of Yoshimitsu [44], and to explain the unusual contact angle of  $138^\circ$  observed by Yoshimitsu on pillar-like surfaces with  $50\text{-}\mu\text{m}$  pillar width,  $100\text{-}\mu\text{m}$  spacing, and  $10\text{-}\mu\text{m}$  height (obtained by dicing flat silicon wafers), he introduces the hypothesis of a *mixed wetted* mode. Despite the limited experimental proof provided, his approach seems interesting, and the assumption of the *mixed wetted* mode especially could be useful for better understanding the effect of double roughness structures, such as those observed in nature.

In the following paragraphs no theoretical digression for quantifying the pressure necessary to induce the Cassie-Wenzel transition will be proposed, and the validity of the two approaches described above will not be discussed further. Instead, extensive experimental results will be described in order to prove the fundamental validity of the principle clearly expressed for the first time by Bico and Quere [92] five years ago (see Chapter 4, “Theoretical background” paragraph). Such a principle, later supported by other authors [50], identifies the intersection point between the Cassie and Wenzel curves, plotted as a function of  $\cos\theta_{\text{flat}}$  (or similarly, as a function of one geometrical roughness parameter), as the only position of the thermodynamically predictable transition between the two regimes possible on a rough substrate. In this context, the results presented in the next paragraphs will all support the validity of the thermodynamic interpretation proposed in Chapter 4, and will clearly confirm the reliability of the classic Wenzel and Cassie models.

### 6.3 Dynamic contact angle results

Note: “SCA” hereafter designates “static contact angle”; “DCA” “dynamic contact angle”; “ACA” “advancing contact angle”; “RCA” “receding contact angle”; and “CAH” “contact angle hysteresis”.

ACA and RCA measurements applying a NON-negligible extra-pressure on the drop-substrate system were performed on two series of perfluorosilanized microstructured silicon substrates differing, in asperity size and aspect ratio in the micrometer range. For details of the adopted methods of microstructuring and perfluorosilanization, see Appendix 1 and Chapter 3 respectively. The first sample series consists of 13 samples with square distribution of 10- $\mu\text{m}$  diameter pillars, of 40- $\mu\text{m}$  height (i.e.  $h = 4d$ ), and pitch varying between 15  $\mu\text{m}$  and 150  $\mu\text{m}$ ; the second sample series consists of 10 samples with square distribution of 4- $\mu\text{m}$  diameter pillars, of 40- $\mu\text{m}$  height (i.e.  $h = 10d$ ), and pitch varying between 6  $\mu\text{m}$  and 52  $\mu\text{m}$ . Through the selected sample series, it has been possible to study and compare the influence on wetting properties of microstructured hydrophobic surfaces (especially on the Cassie-Wenzel transition position) of several geometrical parameters simultaneously. These parameters are the spacing between consecutive pillars (pitch), pillar diameter, pillar height, and asperity absolute size.

### Sample series with 10- $\mu\text{m}$ diameter pillars ( $h = 4d$ )

Fig. 6.3 shows ACA and RCA values measured by applying a NON-negligible extra-pressure ( $\sim 3$  kPa) on substrates presenting 10- $\mu\text{m}$  diameter cylindrical pillars, of 40- $\mu\text{m}$  height, and pitch varying between 1.5  $\mu\text{m}$  and 150  $\mu\text{m}$ .

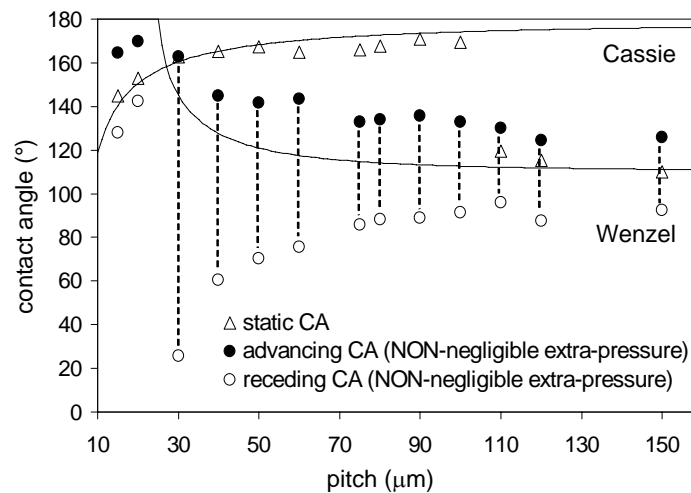


Fig. 6.3 *DCA values obtained by exerting a NON-negligible extra-pressure on drop-substrate system, as a function of pitch. The considered samples consist of square arrangements of 10- $\mu\text{m}$  diameter cylindrical pillars, of 40- $\mu\text{m}$  height. SCA values measured with  $\sim 3\text{-}\mu\text{L}$  volume drops are also reported to illustrate the metastability region of the Cassie composite regime.*

As highlighted by the dashed vertical lines, the CAH values change suddenly, passing from  $\sim 25^\circ$ , on pitches smaller than that corresponding to the Cassie and Wenzel curve intersection, to a value as high as  $\sim 120^\circ$ , for the first considered larger pitch. This phenomenon indicates that the  $\sim 3$  kPa applied during the initial measurement phase enables the energy barrier to be overcome between the metastable Cassie state and favored Wenzel state on the sample with  $30\text{-}\mu\text{m}$  pitch, i.e. the first pitch larger than that corresponding to the Cassie-Wenzel equal energy point. The very small RCA recorded on such a substrate represents clear proof that the Wenzel regime has been attained. The liquid that has penetrated among the asperities meets strong resistance to the retracting process, due to the increased pinning at asperity edges of the continuous contact line during its retraction movement in the three directions. To demonstrate the particular “liquid trapping” phenomenon observed on the substrate with  $p = 30\ \mu\text{m}$  (designated “super-wetted” state), the different phases of the corresponding CAH measurements performed with an extra-pressure of  $\sim 3$  kPa are reported in Fig. 6.4. From the very low RCA identified in image 11, and especially the liquid trace remaining on the substrate at the end of the process in the region delimiting the drop-substrate contact area (image 12), it can reasonably be deduced that the drop is in the *wetted* regime.

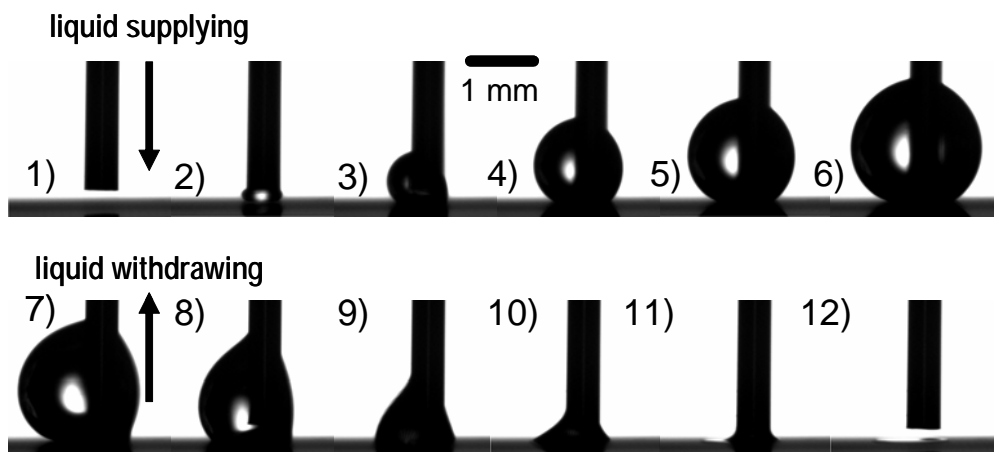


Fig. 6.4 “Super-wetted” state. Image sequence representing hysteresis measured on sample with  $p = 30\ \mu\text{m}$ , in the configuration “with a NON-negligible extra-pressure”. The *wetted* regime is proved by the very small RCA (image 10), and by the liquid trace resting on the substrate at the end of the process.

In Fig. 6.5, the DCA results obtained by applying  $\sim 300$  Pa are shown again to facilitate the comparison between the case of a “negligible” extra-pressure and results obtained by applying a “NON-negligible” extra-pressure. In Fig. 6.3 and Fig. 6.5, it can be noted that the



first two pairs of values, corresponding to the ACA and RCA on the first two samples of the series ( $p = 15 \mu\text{m}$  and  $20 \mu\text{m}$ ), are coincident in the two graphs, proof that in both cases the same *composite* wetting regime exists.

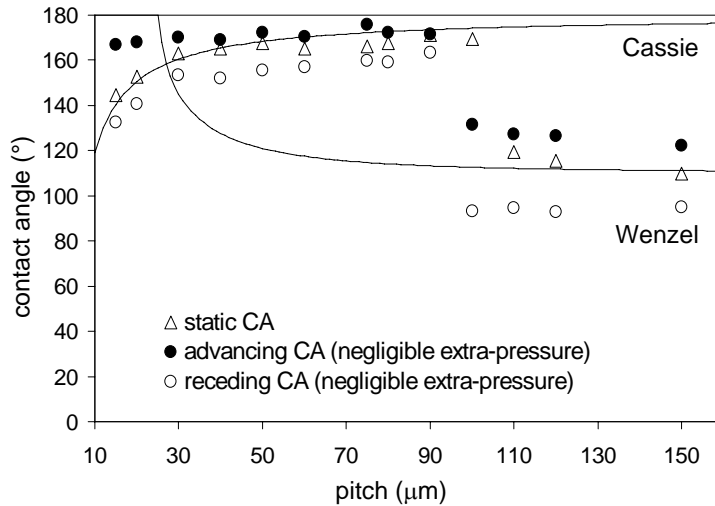


Fig. 6.5 *DCA measurements performed exerting a negligible extra-pressure on drop-substrate system, as a function of pitch. The considered samples are the same as those in Fig. 6.3 (square arrangements of 10- $\mu\text{m}$  diameter cylindrical pillars, of 40  $\mu\text{m}$  height). SCA values, measured with drops of  $\sim 3\text{-}\mu\text{L}$  volume, are also reported, to illustrate that, contrary to Fig. 6.3, this measurement configuration shows no significant difference in relation to the static Cassie-Wenzel transition position.*

Despite the fact that the solid-liquid interface at the drop base cannot be observed in detail, it is reasonable to assume the drop in the *composite* regime, since ACA and RCA values are nicely disposed around the Cassie curve. Millimeter- size drops of a volume up to  $\sim 10 \mu\text{L}$  have been seen to stick on these surfaces even for a  $90^\circ$  tilt angle. This signifies that such surfaces cannot be defined as “self-cleaning”. The liquid pinning at the edges of the asperity top-surfaces is still significant due to the long contact line associated with small pitches, i.e. high asperity surface densities (see estimations of  $CL_{\text{tot}}$  “total contact line length” as a function of pitch for *composite* states in Chapter 5).

For a larger pitch than corresponding to the point where Cassie and Wenzel states present equal energy, the two graphs differ significantly. In particular, in Fig. 6.3, the *composite* regime persists for a pitch  $p = 9d$ , while in Fig. 6.5, for pitches larger than  $27 \mu\text{m}$ , corresponding to  $p \geq 3d$  (i.e. the Cassie-Wenzel intersection point), the only regime observed is the *wetted* one. Especially, in the whole pitch range between  $27 \mu\text{m}$  and  $150 \mu\text{m}$ , ACA values are in good agreement with the Wenzel curve trend, while RCA values are far lower, particularly in the

first part (i.e. the region of higher asperity surface density). Assuming that the adopted liquid withdrawing speed can also influence the above described liquid trapping phenomenon, the measured CAH tendency suggests two considerations. Firstly, it is proof of the constant liquid withdrawing speed maintained during all measurements. Secondly, by decreasing such a speed indefinitely, it should be possible to record RCAs that follow the theoretical Wenzel curve, possibly shifting below it by a slowly decreasing number of degrees, when the pitch is increased.

To summarize, DCA measurements performed with a NON-negligible extra-pressure, applied by positioning the needle apex close to the substrate before any liquid supplying phase, permitted identification of the region corresponding to the thermodynamically predictable Cassie-Wenzel transition. For pitches smaller than those corresponding to the intersection between Cassie and Wenzel curves, CAH values measured “with” and “without” forcing the drop in the asperities are practically coincident. For these samples, no water penetrates into the cavities. For pitches larger than those corresponding to the intersection between the Cassie and Wenzel curves, the significant discrepancy between CAH values recorded in the two possible configurations corresponds to the two different regimes: high CAH for the *wetted* regime, and very low CAH for the *composite* regime. For the two smallest pitches, the constant and low hysteresis values prove that the extra-pressure exerted in the “needle close to substrate” configuration is not sufficient to cause liquid penetration among the asperities. Such an extra-pressure permits liquid intrusion among the asperities however for all the metastable *composite* states observed for pitches larger than those corresponding to the thermodynamic transition point. For pitches larger than  $p = 9d$ , independent of the distance between needle apex and substrate (i.e. independent of the exerted extra-pressure), only the *wetted* regime is observed.

The results described so far can be represented by reporting the CAH values obtained in both measurement configurations as a function of pitch, as in Fig. 6.6, referred to as the “hysteresis loop”. In this graph, the region of pitches where *composite* states are metastable is clearly shown. For pitch  $p \leq 3d$ , the two curves are coincident and demonstrate that the *composite* state is that experimentally and theoretically favoured. For  $p \geq 9d$  the two curves are again coincident and represent *wetted* states that are experimentally and thermodynamically favored. In the pitch range comprised between  $3d$  and  $9d$  the two curves separate, the lower representing *composite* states experimentally favored but thermodynamically unstable, observable with a negligible extra-pressure exerted on the system, and the upper representing

wetted states experimentally and thermodynamically favored, observable with a NON-negligible extra-pressure exerted on the system.

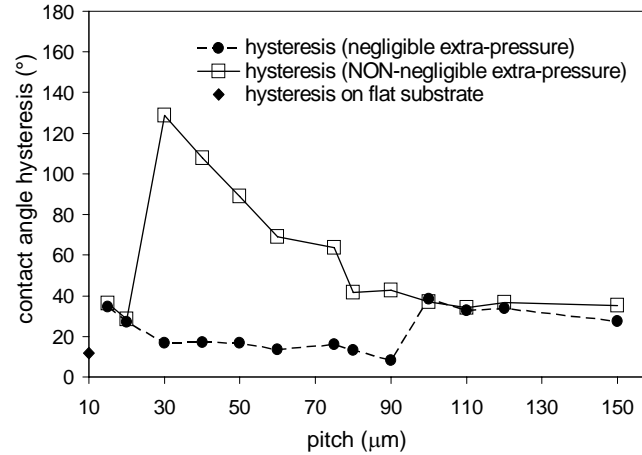


Fig. 6.6 *Contact angle “hysteresis loop”*. Summary of water CAH values recorded for square distributions of 10- $\mu\text{m}$  diameter cylindrical pillars, of 40- $\mu\text{m}$  height, with pitch varying between 15 and 150  $\mu\text{m}$ , as a function of pitch, for the two considered DCA measurement configurations.

### Sample series with 4- $\mu\text{m}$ diameter pillars ( $h = 10d$ )

Fig. 6.7 shows the experimental results obtained from DCA measurements applying a NON-negligible extra-pressure ( $\sim 3$  kPa) related to substrates consisting of square distributions of 4- $\mu\text{m}$  diameter cylindrical pillars, of 40- $\mu\text{m}$  height, and pitch varying between 6  $\mu\text{m}$  and 52  $\mu\text{m}$ . Whereas for 10- $\mu\text{m}$  diameter pillars, of 40- $\mu\text{m}$  height (see Fig. 6.3), the metastable Cassie state region corresponds to pitch  $p \geq 3d$ , in the case of 4- $\mu\text{m}$  diameter pillars it corresponds to pitch  $p \geq 4.25d$ , due to the relative increase in pillar height (here  $h = 10d$ , instead of  $h = 4d$ , as was the case in Fig. 6.3). The abrupt change in CAH values observed at the Cassie-Wenzel intersection point, represented by the dashed vertical line reported only for  $p \geq 4.25d$ , proves that the thermodynamically predictable Cassie-Wenzel transition can also be revealed experimentally.

Fig. 6.8 again shows the results obtained exerting a negligible extra-pressure on the same sample series to illustrate the differences between the two measurement configurations. Also in this case of a pillar relative height increase, a pressure of  $\sim 3$  kPa permits the experimental localization of the thermodynamic Cassie-Wenzel transition.

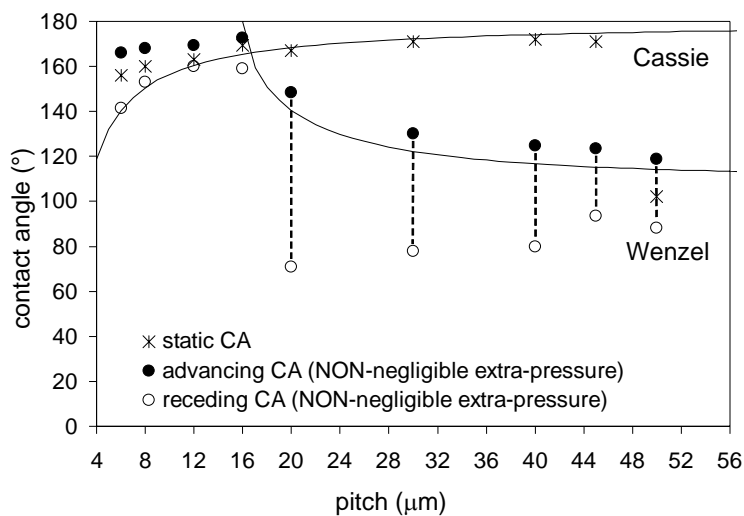


Fig. 6.7 *DCA measurements performed exerting a NON-negligible extra-pressure on 4- $\mu\text{m}$  diameter pillars. The considered samples consist of square arrangements of 4- $\mu\text{m}$  diameter cylindrical pillars, of 40- $\mu\text{m}$  height, with pitch varying between 6  $\mu\text{m}$  and 52  $\mu\text{m}$ . Cassie and Wenzel theoretical curves are reported, together with SCA values measured for drops of  $\sim 3\text{-}\mu\text{L}$  volume, to illustrate the metastability region of the Cassie composite regime.*

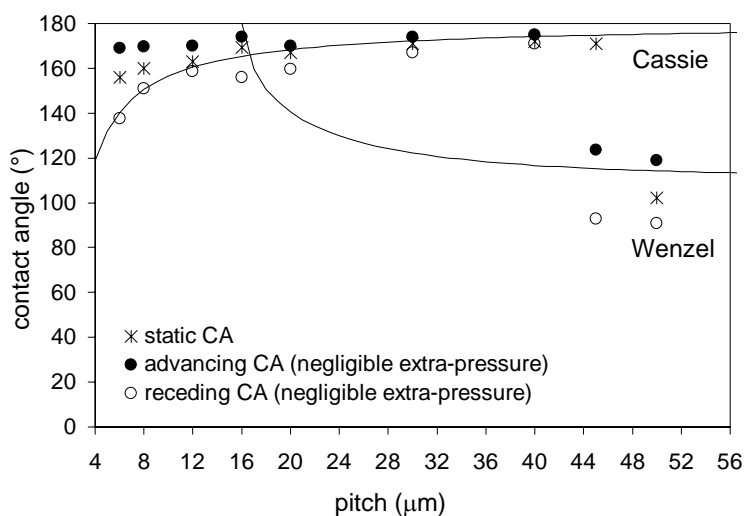


Fig. 6.8 *DCA measurements performed exerting a negligible extra-pressure on 4- $\mu\text{m}$  diameter pillars. The considered samples are the same as in Fig. 6.5 (square arrangements of 10- $\mu\text{m}$  diameter cylindrical pillars, of 40  $\mu\text{m}$  height). SCA values measured with drops of  $\sim 3\text{-}\mu\text{L}$  volume are reported, to emphasize the fact that, in contrast to Fig. 6.5, this measurement configuration does not significantly differ from the static case.*

## 6.4 Super OIL-repellent microstructured substrates

The sample series of 10- $\mu\text{m}$  diameter cylindrical pillars, of 40- $\mu\text{m}$  height, with pitch varying between 15  $\mu\text{m}$  and 150  $\mu\text{m}$ , and distributed in square arrangements, was used for testing wetting properties with respect to a liquid with different chemical and physical properties than water (i.e. lower surface tension, due to its non-polarity and the absence of hydrogen bonds). The chosen liquid is *n*-hexadecane ( $\text{C}_{16}\text{H}_{34}$ ), the linear hydrocarbon chain of 16 completely hydrogen-saturated carbon atoms. On perfluorinated, naturally oxidized silicon surfaces, this liquid presents an SCA, ACA and RCA of  $65^\circ$ ,  $69^\circ$ , and  $60^\circ$ , respectively. Again, the wetting property characterization of the whole sample series was made using SCA and DCA measurements, the latter performed in both pressure configurations.

The results obtained by the DCA measurements exerting a negligible extra-pressure, compared to the related SCA values, are presented in Fig. 6.9. First, the surprisingly significant extent of the experimental *composite* regime can be noted (see image 2 in Fig. 6.9-b, corresponding to pitch  $p = 40 \mu\text{m}$ ), and the decreasing CAH value associated with the pitch increase. This latter aspect indicates that the observations made in Chapter 5 concerning the influence that contact line length and fragmentation can have on the pinning related to hysteresis phenomena observed for water on rough surfaces are also valid for “wetting liquids”.

Since the Cassie contact angle curve is always higher than the Wenzel curve, for wetting liquids the Cassie *composite* states must correspond to higher thermodynamic energy. This is represented in Fig. 6.10 by the monotonically decreasing curve associated with the difference between the energies of the Cassie and Wenzel states, calculated using the approach presented in Chapter 4 (Eqs. 4.4 and 4.6). In the same figure, the gray curve represents the energy barrier between a possible metastable Cassie state and the corresponding Wenzel stable state, calculated using the method described in Chapter 4 (Eq. 4.13). For this thermodynamic calculation, a “drop-substrate” system consisting of a 2- $\mu\text{L}$  *n*-hexadecane drop, and a 3-mm radius circular area of a perfluorinated silicon microstructured substrate was considered. The related interfacial energy values are  $\gamma_{LV} = 27.5 \times 10^{-12} \text{ mJ}/\mu\text{m}^2$ ,  $\gamma_{SV} = 13 \times 10^{-12} \text{ mJ}/\mu\text{m}^2$  (i.e. the critical surface energy of the developed perfluorosilane coating estimated by the Zisman plot -see Chapter 3-), and  $\gamma_{SV} = 1.4 \times 10^{-12} \text{ mJ}/\mu\text{m}^2$  (derived by Young’s equation with  $\theta_{\text{flat}} = 65^\circ$ ).

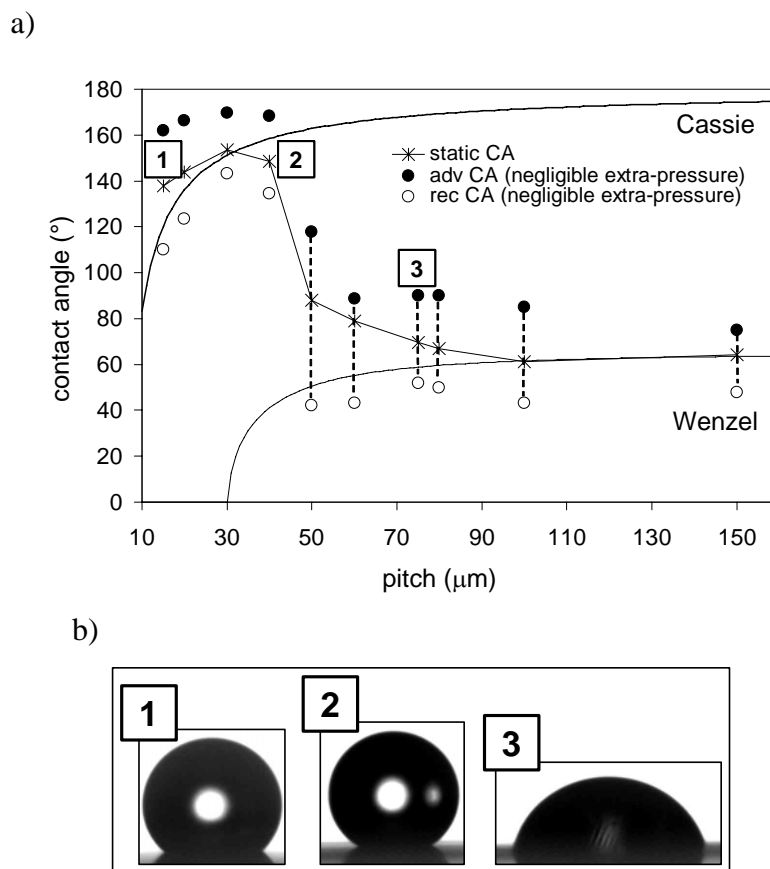


Fig. 6.9 *Oil-drop behavior on hydrophobic microstructured substrates. n-Hexadecane ACA and RCA values measured in the configuration “with a negligible extra-pressure” on square arrangements of 10-μm diameter pillars, of 40-μm height, with pitch varying between 15 and 150 μm. Vertical dashed lines, representing CAH values, are reported for wetted states only. SCA values, measured with drops of ~ 2-μL volume, are reported to show that this measurement configuration localizes the Cassie-Wenzel transition in the same region of static measurements. Cassie and Wenzel theoretical curves are traced, considering  $\theta_{\text{flat}}=65^\circ$ . In (b) side view images of *n*-hexadecane drops are reported that correspond to the substrate indicated by 1, 2, 3 in (a).*

For liquids that on the flat surface form contact angles lower than  $90^\circ$  (i.e. wetting liquids), the energy barrier estimated considering the energy necessary to fill the asperities, keeping the Cassie angle constant, represents a monotonically increasing curve. In particular, the range corresponding to the experimental Cassie-Wenzel transition appears in the region where the energy barrier curve approaches zero. The transition should occur when the energy barrier between the metastable Cassie state and the Wenzel thermodynamically favored state is lower than the drop energy, associated, for example, with the drop vibrations. In the interpretation proposed in Chapter 4, drop vibrations would constitute the main reason for the Cassie-Wenzel transition observed in equilibrium conditions (such as those corresponding to static and dynamic measurements with a negligible extra-pressure).

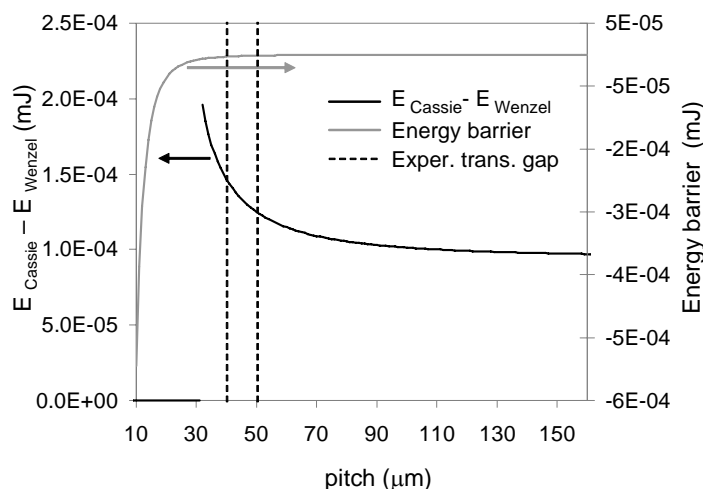


Fig. 6.10 Pitch influence on thermodynamic analysis of system composed by a 2- $\mu\text{L}$  oil-drop on a perfluorosilanzed microstructured substrate. The black line (left scale) represents the energy difference between Cassie and Wenzel states as a function of pitch, and the gray line (right scale) represents the energy barrier estimated as the energy necessary to fill the asperities keeping the Cassie angle constant. The experimental transition range is also reported by black dashed lines.

The order of magnitude of the energy barrier estimated for pitch  $p = 45 \mu\text{m}$  (i.e. a pitch arbitrarily considered in the middle of the experimental transition range) is  $10^{-6}$  mJ. Such a value can be associated with the kinetic energy of a 2- $\mu\text{L}$  hexadecane drop falling freely from a distance of 130  $\mu\text{m}$ , and seems acceptable as possible extra-energy associated with the SCA measurements (see Chapter 4). Although the quantitative reliability of this estimation still remains to be rigorously proven, the proposed arguments can be accepted as a first attempt to intuitively describe the Cassie-Wenzel transition mechanism.

Although the classic Wenzel and Cassie models do not predict any thermodynamically stable *composite* state for wetting liquids, the possibility of experimentally observing metastable *composite* states is unquestionable. Moreover, the coincidence of the Cassie-Wenzel transition position determined by static and dynamic measurements respectively is further proof that metastable *composite* states on microstructured perfluorosilanzed surfaces are also possible for wetting liquid, such as hexadecane. Additionally, the experimental *composite* states found for pitch  $p \leq 40 \mu\text{m}$  are proved to be resistant to an extra-pressure of  $\sim 300$  Pa.

In Fig. 6.11, the hexadecane SCA values are compared to the results of DCA measurements obtained by applying an extra-pressure of  $\sim 3$  kPa, which, in all the cases

previously considered of water drops on microstructured perfluorosilanzed substrates, has always been sufficiently significant to reveal the Cassie-Wenzel transition in the region defined by thermodynamic analysis.

As expected, all samples present drops in the *wetted* state, and the vertical dashed lines traced to represent hysteresis variation as a function of pitch increase clearly confirm this. In particular, especially for smaller pitches, the experimental CAH is very large ( $\sim 120^\circ$ ) due to very low RCA and the nonetheless relatively high ACA.

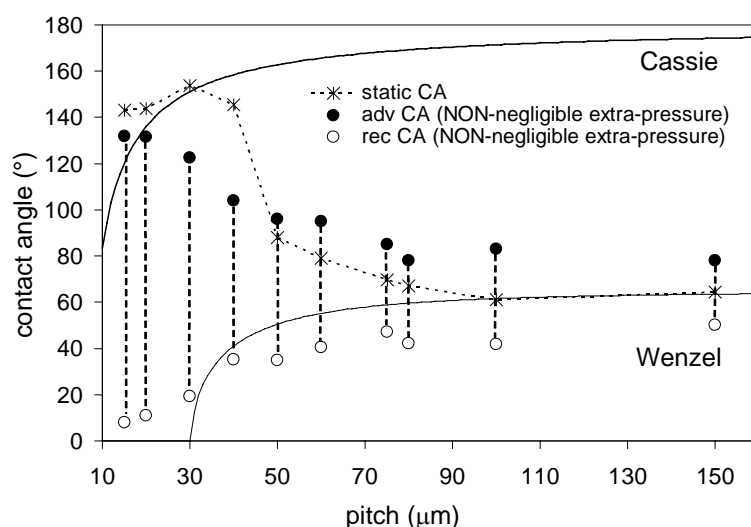


Fig. 6.11 *Oil-drop behavior on hydrophobic microstructured substrates. n-Hexadecane ACA and RCA values measured exerting “a NON-negligible extra-pressure” on the samples series with square distributions of 10- $\mu\text{m}$  diameter pillars, of 40- $\mu\text{m}$  height and pitch varying between 15 and 150  $\mu\text{m}$ . SCA values are also reported for drops of  $\sim 2\text{-}\mu\text{L}$  volume. Vertical dashed lines representing CAH values measured in this configuration show that all considered cases correspond to drops in the *wetted* regime.*

However, in contrast to Fig. 6.9, ACA values for pitch  $p \leq 40\mu\text{m}$  are lower than SCA values. This confirms the complete wetting of such substrates, and the different regime associated with SCA measured on them (i.e. *composite* regime).

An interesting aspect regarding the results presented in Fig. 6.11 is the way they vary when the pitch is varied. The curves that would ideally connect all ACAs and RCAs respectively, apart from being a clear sign of the *wetted* regime on all considered samples, present a tendency that cannot be associated with any of the classic laws, at least for pitch  $p \leq 75\mu\text{m}$ . In particular, in the pitch range comprised between 10 and 30  $\mu\text{m}$ , where Wenzel law predicts apparent contact angle of  $0^\circ$ , on the one hand the ACAs are very high, close to the value predicted by Cassie law, and on the other hand the RCAs are very low, close to  $0^\circ$ . When



the pitch is increased, for both the ACA and the RCA, experimental results slowly approach the Wenzel curve, and delimit a range around it that seems “normal” only for pitch  $p \geq 75\mu\text{m}$ . As already proposed when discussing the results obtained on the same sample series using water, such tendencies are probably due to the effect of the imposed liquid supplying and withdrawing speeds. The hypothesis of a partial liquid penetration among the asperities, often proposed in literature as a possible explanation for contact angle values not predictable by Cassie or Wenzel models, or by improved theories, seems less probable, at least for the flat-top microstructures considered in this work.

Summarizing, the experimental results presented in Fig. 6.9 and Fig. 6.11 suggest that, since the *wetted* regime is the only thermodynamically stable one for wetting liquids, whatever the asperity surface density on microstructured substrate, a relatively small extra-pressure (in the order of a few kPa) should always suffice to achieve the *wetted* Wenzel state.

## 6.5 Conclusions

In this chapter it has been shown that, for substrates structured in the micrometer range, a relatively low extra-pressure of  $\sim 3$  kPa is sufficient to experimentally confirm the position of the Cassie-Wenzel transition predicted by thermodynamics, i.e. at the level of the Cassie-Wenzel curve intersection. It has been possible to validate such a prediction by experiments carried out on two sample series with different asperity size and different asperity aspect ratio. This suggests that the generally accepted principle [50][51][55][95] relating “higher asperities to more stable *composite* states” derives rather from the increased extent of the thermodynamically stable *composite* regime. In fact, in graphs of Cassie and Wenzel angles as a function of pitch, a larger asperity height implies a shift at larger pitch of the intersection between the two curves, extending the region where *composite* states are thermodynamically stable (at small pitch) and reducing the region where they are metastable.

Considering these results, together with those presented in Chapter 5 (where an extra-pressure approximately 10 times smaller than that applied here confirmed the Cassie-Wenzel transition position found by static measurements, and predicted by the simple approach developed in Chapter 4 -see Eq.4.13-), it seems reasonable to assume that to induce the Cassie-Wenzel transition for pitches smaller than that corresponding to the thermodynamic Cassie-Wenzel transition, a much larger pressure than the highest used in this work, probably even

several orders of magnitude larger, would be necessary. For this purpose, further systematic DCA investigations, varying the exerted extra-pressure over a much larger pressure range would be appropriate.

Systematic experimental investigations concerning the static and dynamic wetting properties of microstructured substrates respect to a so-called “wetting liquid” (such as *n*-hexadecane) have been reported for the first time. All the presented results confirm the hypothesis that for wetting liquids it does not seem possible to show *composite* states on microstructured substrates with sufficient robustness for eventual practical applications, since even the relatively low extra-pressure of  $\sim 3$  kPa (corresponding to  $\sim 30$  cm of water) is sufficient to push the liquid drop among the asperities for all the considered substrates, in accordance with thermodynamic arguments.

To conclude, the adopted dynamic measurement techniques permitted the experimental identification of the asperity surface density range where *composite*-Cassie state are metastable for both non-wetting and wetting liquids.

---

# 7 Conclusions

## 7.1 Results summary

At the beginning of this thesis work, attention was drawn to certain outstanding questions relating to the understanding of superhydrophobicity phenomena, such as:

- 1) Is it possible to formulate a criterion for predicting which kind of wetting regime (*composite* or *wetted*) will occur on a selected rough surface?
- 3) What influence do the main roughness parameters have on the Cassie-Wenzel transition?
- 2) How stable are *composite* metastable states?
- 4) What is the effect of the three-phase contact line on stationary and dynamic wetting phenomena?
- 5) What is the ideal roughness size and shape of a robust superhydrophobic surface?
- 6) What is the asperity absolute size range delimiting the field where superhydrophobicity appears and vanishes?

During this work, systematic experimental results describing the static and dynamic wetting properties of hydrophobic microstructured substrates, presenting regular distributions of flat-top obstacles with different geometrical characteristics (such as distance between consecutive obstacles, obstacle typical size, obstacle height, obstacle top-surface shape, etc.) have been produced. Analysis of the obtained experimental results has allowed theoretical and phenomenological arguments to be proposed to answer the above-mentioned questions.

The general validity of Cassie and Wenzel theoretical models in predicting the contact angle on a surface of known flat-top roughness has been demonstrated for all the considered roughness parameters. In the hypothesis of liquid drops several orders of magnitude larger than the typical asperity dimension, the measured macroscopic contact angle was always close to one of the two values calculated by the classic laws. In particular, the thermodynamic analysis developed on the basis of system surface energy minimization has been shown to be an

efficient tool for predicting which model will describe the considered drop-substrate system. The validity of the proposed thermodynamic interpretations has been confirmed by water and hexadecane dynamic contact angle measurements performed in two different configurations, i.e. with a “negligible” and with a “NON-negligible” extra-pressure exerted on the drop-substrate system (corresponding to pressures of  $\sim 300$  Pa and  $\sim 3$  kPa, respectively). Depending on the method adopted to create contact between the liquid and the rough surface, the system can in fact present one of the following wetting regimes: Cassie thermodynamically stable, Wenzel thermodynamically stable, or Cassie metastable. For each geometrical roughness parameter, the different regions related to each possible wetting state have been clearly delimited. In particular, the *composite* metastable states (i.e. those of practical interest for their very high contact angle, with a very low contact angle hysteresis) present a stability that varies as a function of each roughness parameter such as the energy barrier calculated as the difference between the energy of the *composite* Cassie state suspended at the asperities’ top-surfaces and the energy of the hypothetical *composite* state with the same Cassie contact angle, but with the space between the asperities almost completely filled by the liquid. For non-wetting liquids (i.e.  $\theta_{\text{flat}} > 90^\circ$ ), thermodynamically favored *composite* states of a certain robustness (i.e. resisting extra-pressures of up to 3 kPa) are predicted and experimentally observed. For wetting liquids (i.e.  $\theta_{\text{flat}} < 90^\circ$ ), although some *composite* states are observable at an extra-pressure of 300 Pa, a pressure of  $\sim 3$  kPa suffices to reach the Wenzel *wetted* state for all the considered cases, confirming the theoretical prediction that wetting liquids do not admit any thermodynamically favored *composite* state.

Studying the effect of asperity absolute size and top-surface perimeter on water static and dynamic contact angles, especially in relation to the Cassie-Wenzel transition position and contact angle hysteresis value allowed the effect of each contact line feature (i.e. its length, fragmentation, corrugation) on superhydrophobic phenomena to be distinguished. In particular, the results obtained by varying the obstacle top-surface shape demonstrated that contact line length and corrugations are second-order factors, whereas the increase in extent and stability of the *composite* metastable state, experimentally observed with a decrease in asperity absolute size, could be interpreted as being mainly due to the effect of contact line fragmentation.

These last experiments in the microscale range, with those investigating the water contact angle on nanostructured substrates as a function of the spacing between consecutive pillars,

constituted the consistent experimental basis allowing the possible asperity size limits where superhydrophobicity appears and vanishes, with the most suitable size within this range, to be suggested. For rough substrates, a maximum asperity size of  $\sim 50 \mu\text{m}$  was finally indicated that where superhydrophobicity of a certain practical interest can be observed, and some tens of nanometers was considered the minimum size. Below 10 nm, the roughness of molecular dimension is approached, where *composite* states like those observed on microstructured substrates have never been reported. In the range delimited above, a size scale comprised between several hundred nanometers and one micron has been proposed as the optimum asperity size for designing superhydrophobic surfaces of good quality, since it is in the region of this value that the maximum extent of the *composite* regime associated with a good stability has been observed.

The asperity height, which in principle does not influence the thermodynamic energy of Cassie states (since the Cassie roughness factor  $f$  is independent of  $h$ ), has a considerable practical impact on the energy barrier between such a state and the associated Wenzel state (since it strongly influences the Wenzel roughness parameter  $r$ ). This is clearly shown, for instance, in the shift of the theoretical Cassie-Wenzel transition position observed by varying the asperity height  $h$  in the contact angle prediction as a function of the pitch. For taller asperities a larger region of stability of *composite* states is obtained, and vice versa. In general, it seems intuitive to consider that taller asperities should maintain a drop in the *composite* state under the action of external forces more efficiently, even in the region of metastability, as in the presence of a hypothetical state of partial liquid penetration among the asperities due to the action of an external force. However, it can be affirmed that none of the experiments performed in this work with extra-pressures in the order of several kPa maximum have ever led to the assumption that this situation was possible. The Cassie-Wenzel transition has been interpreted as a phenomenon occurring at the top-surface of the asperities, probably due to drop vibrations. For this reason, it is suggested that the asperity height must be slightly greater than the maximum liquid penetration among the asperities due to the maximum menisci curvature at the asperities' surfaces. Such a maximum menisci curvature would be attained only in dynamic situations, when the contact angle at the asperity edges equals the advancing contact angle on a flat surface.

### 7.2 Future work

Strictly in relation to the theoretical discussion presented in this work, it would be interesting to investigate to what extent the rough approximation of the energy barrier value between the metastable *composite* Cassie state and the stable *wetted* Wenzel state, demonstrated here to be qualitatively good, is also quantitatively correct. For this purpose, the use of a powerful computational method that minimizes drop energy [201] with fewer assumptions, and more realistic parameters, could be considered.

The maximum extra-pressure of  $\sim 3$  kPa considered here has shown the validity of classic models for predicting the region of thermodynamic stability and metastability of both wetting regimes. However, no systematic investigation has been performed that might suggest a relation between the Cassie-Wenzel transition and a quantified extra-pressure necessary to induce it. As mentioned, in the region of metastability of Wenzel states, such an extra-pressure could be imagined as at least several orders of magnitude greater than the  $\sim 3$  kPa used in this work. It would be interesting to conduct experiments where water drops of different volumes are launched at high speed onto the structured surfaces. Estimation of the pressure involved at impact, together with detailed analysis of drop deformations due to impact, possibly combining high speed video acquisitions with recently developed methods for contact angle determination of drops of any shape [202], would permit the study of the Cassie-Wenzel transition position as a function of the applied force, in relation to specific geometrical parameters. This would be a situation where varying asperity height over a wide scale range, and for different asperity surface densities (i.e. different pitches) would be really useful for elucidating the influence of asperity height on the robustness of the *composite* stable and metastable state. Such experimental evidence would constitute a fundamental step towards the concrete possibility of the practical exploitation of superhydrophobic surfaces.

More detailed investigations concerning the optimum asperity size where superhydrophobicity presents the best qualities would be possible by “shrinking” asperity size within a scale ranging from  $3 \mu\text{m}$  to the minimum size permitted by available structuring techniques. In this context, special studies devoted to finding new experimental results supporting the interpretation proposed in this work regarding height influence on superhydrophobicity would be valuable.

As indicated in the title of this work, and emphasized on many occasions throughout the text, the roughness typology considered here consists of discrete flat-top surface asperities. Such a rough surface is the one most studied from both the theoretical and experimental points of view, since it is easier to model and produce it. This means that a systematic experimental study performed on a roughness other than the periodical distributions of flat-top discrete asperities is lacking. Possible interesting roughness typologies for in future studies could be: a) those corresponding to the negative version of the structures studied here, i.e. grids presenting a periodical distribution of cavities, differently shaped (e.g. honeycomb structures, or square holes); or b) those showing rounded or conical roughness top-surfaces. As far as the grids are concerned, a study of structures presenting the same  $r$  and  $f$  parameters considered by the systematic “scaling criterion” adopted in this work could be imagined, and the results obtained for both kinds of structures with respect to the Cassie-Wenzel transition and hysteresis values could be compared to illustrate the effect of contact line continuity and discontinuity. As for structures presenting rounded shapes, the systematic study of their wetting properties would have a significant immediate impact especially with a view to possible applications. A suitable method for producing such structures could be the hot-embossing of polymers. This would be a convenient replication technique due to its relatively low cost (especially if compared to those used for silicon microstructuring), and it would also be the most appropriate one for the production of polymeric microfluidics devices for labs-on-chips, or general biological applications. Another interesting roughness typology that would have to be studied in a more systematic way, from both the experimental and theoretical points of view, would be that of hierarchical structures, similar to those observed in nature on certain plant leaves. Although their modeling would involve significant difficulties, they seem to be the most promising structures nowadays with really good superhydrophobic properties [54][74][145][146].

Last but not least, in order to complete the overview of wetting properties on rough surfaces, contact angle investigations carried out by systematically varying the temperature of the system and the liquid would be helpful. The variation of surface energy due to changes in the thermodynamic conditions of the system, when chemistry is constant, should imply variations in the transition position that may not be experimentally detectable. However, measurements made using different liquids and liquid mixtures should show not only differences in the Cassie-Wenzel transition position, but also significant discrepancies in relation to the classic laws. Unlike what was demonstrated in this thesis work for water, when

## 7 Conclusions

---

the probe liquid chemistry is changed, factors such as gravity, capillarity, and liquid molecule size may not in fact be negligible.



---

# APPENDIX 1: Silicon microstructuring

*In this appendix, the procedures adopted to prepare the microstructured silicon substrates studied in this thesis work are described. All samples have been fabricated by the author at the Center of Micro- and Nano-Technology (CMI) of EPFL, in a clean room (class 100) equipped with modern and powerful machines for micro- and nano-fabrication processing.*

## **Silicon as reference substrate**

Silicon has been chosen as reference substrate material for two main reasons: a) for profiting of the standard microstructuring techniques, which have been developed and improved in the last decades thanks to the progress in semiconductor and IC industry and research; b) for the property of the silicon surface to be easily chemically modified by silanization.

Silicon substrates, kept in normal atmosphere, are naturally oxidized. Their surface present an amorphous silicon oxide layer of about 1.5-2 nm thickness.

## **Periodically microstructured silicon substrates**

One side polished silicon test wafers (4 inch diameter, <100> oriented, P/N doped, 525  $\mu\text{m}$  thick), covered with a native layer of  $\text{SiO}_2$  were supplied by the CMI.

From the silicon wafer as it is delivered, to the  $\sim 1 \text{ cm}^2$  area microstructured samples, ready for the perfluorosilanization step, several standard photolithography processes have to be performed.

The masks design has been carried out using L-Edit, a computer program for the conception of integrated circuits.

In the mask design the geometrical parameters of the desired final roughness have been fixed, except the asperity height, which depends on the selected reactive ion etching process (RIE), and its duration.

---

The photolithography processes in the clean room begin after that the operator has converted the design file (CIF or GDSII format), in the format of the Direct Laser Writer that will be used for transferring the design onto the silicon substrate.

The complete clean room procedure to get the structured wafer is composed by the following steps:

- 1) Activation of the native silicon oxide layer at the wafer surface by HDMS.
- 2) Wafer photoresist coating.
- 3) Direct laser writing for transferring the mask design on the wafer.
  - Optical microscope observation
- 4) Development of the laser exposed photoresist.
  - Optical microscope observation
- 5) Dry silicon etching.
  - Optical microscope observation.
  - Profilometer investigation.
  - Eventual scanning electron microscope observation.
- 6) Photoresist stripping.
  - Final optical and scanning electron microscope observations.

Some details concerning each step are presented below.

1) The activation of the native silicon oxide layer by the exposure to HexaMethylDiSilazane (H.M.D.S.) vapor in an oven YES III (5 minutes @  $T = 150^\circ$ ) is useful to enhance the adhesion of polymers (such as positive photoresists) before the spin-coating process on Si or SiO<sub>2</sub> substrates.

2) The wafer photoresist coating is performed in a Rite Track 88 Series (Automatic Coater and Developer Tracks). This process allows an uniform and reproducible deposition of photosensitive materials (Shipley Microposit S1800 series) necessary for the following design transfer step.

3) The direct laser writing process transfers the computer predefined design on the photoresist coated wafer. The used apparatus (Heidelberg DWL200) is a high resolution laser lithography system, equipped with a Krypton Ion Laser at 413 nm wavelength, which allows to transfer features with about 1 micrometer precision.

---

4) The irradiated resist is developed in the Rite Track 88 Series, in order to dissolve the photoresist that has not been exposed to the laser beam during the writing process.

5) The deep dry reactive ion etching is the most delicate and fundamental step, since it is that devoted to the structuring of the silicon substrate. It is performed in an Alcatel 601E Plasma etcher, with fluorine based reagents, applying different standard processes for different times, depending on the spacing between consecutive obstacles and the desired height of the structures. This has allowed to obtain regular distributions of the same obstacle with different surface density and aspect ratio “pillar diameter / pillar height”  $d/h \sim 1/4$ , with  $d$  varying in the range between  $3 \mu\text{m}$  and  $20 \mu\text{m}$ .

6) The resist stripping phase is performed in a Coillard wet bench, using a positive photoresist remover (Microposit Remover 1165).

A final step of oxygen plasma exposure in a Branson IPC 2000 system guarantees the removal of any possible photoresist residues, and prepare the substrate to the following phase of hydration and hydrophobic perfluorosilane layer deposition (described in details in Chapter 3).

---

---

## APPENDIX 2: Tests of Extrand’s model on the experimental Cassie-Wenzel transition

*In this appendix, the model proposed by Extrand for predicting when a structured surface presents composite superhydrophobicity is described, and the way it applies to the experimental results presented in Chapter 4 is discussed.*

### Extrand’s model

Alternatively to the thermodynamic approach presented in Chapter 4 (“Theoretical background” paragraph), another model to predict whether a drop, deposited on a structured surface, assumes a Cassie or a Wenzel state was proposed by Extrand [55]. As already reported in Chapter 2, he suggested two criteria that have to be fulfilled to obtain a *composite* regime on a pillar structured surface: the first referred to as “contact line density criterion”, based on the assumption that the contact line at the asperities perimeter has the potentiality to suspend the drop, and the second one referred to as “asperity height criterion”, assuming a curvature of the liquid-air interfaces in the roughness. The first criterion allows the derivation of a critical value of the contact line density  $\Lambda_c$  for the case where the drop weight (“body forces”) balances the “surface forces” along the contact line, and the second one suggests that the asperities have to be sufficiently tall to avoid that the liquid protruding among them does not contact the underlying solid surface.

Defining the contact line density (i.e. the asperity perimeter per surface area) by the relation  $\Lambda = AL/p^2$ , its minimum value is expressed by the equation

$$\Lambda_c = -\rho g V_{\text{drop}}^{1/3} (1-k) \left\{ \frac{\left[ \left( \tan \frac{\theta_{\text{adv}}}{2} \right) \left( 3 + \left( \tan \frac{\theta_{\text{adv}}}{2} \right)^2 \right)^{2/3} \right]}{(36\pi)^{1/3} \gamma_{\text{LV}} \cos \theta_{\text{advflat}}} \right\} \quad (7.1)$$

with

$$k = f \left[ \frac{96(1 - \cos \theta_{\text{adv}})}{2 + \cos \theta_{\text{adv}}} \right]^{1/3} \left[ \left( \tan \frac{\theta_{\text{adv}}}{2} \right) \left( 3 + \left( \tan \frac{\theta_{\text{adv}}}{2} \right)^2 \right) \right]^{-2/3} \quad (7.2)$$

where  $f$  is the fraction of liquid-solid contact area within the interface,  $\rho$  is the liquid density,  $g$  is the gravity acceleration,  $\theta_{adv}$  is the advancing contact angle on the rough surface under consideration, and  $\theta_{adv\ flat}$  is the advancing contact angle on the corresponding flat surface.

On the other side, the minimum critical height of the pillar is given by the expression

$$h_c = b \tan\left(\frac{\theta_{advflat} - \pi/2}{2}\right) \quad (7.3)$$

where  $2b$  is the maximum distance between neighboring pillars. Eqs. 7.1 and 7.2 represent the two formal expressions of Extrand's criteria.

### Comparison with static contact angle results shown in Chapter 4

In Table 1, the results obtained by the static contact angle measurements (right column) performed in this work are summarized and compared to the Extrand predictions based on the above- described "contact line density" and "asperity height" criteria.

Experiments	h criterion	L criterion	Extrand's C-W trans. posit.	Experimental C-W trans. posit.
vs p (Fig. 4.5)	$p < 251 \mu\text{m}$	$p < 51 \mu\text{m}$	$p = 51 \mu\text{m}$	$100 < p < 110 \mu\text{m}$
vs d (Fig. 4.11)	always true	$d > 1.2 \mu\text{m}$	$d = 1.2 \mu\text{m}$	$4 < d < 5 \mu\text{m}$
vs h (Fig. 4.13)	$h > 3.8 \mu\text{m}$	always true	$h = 3.8 \mu\text{m}$	$1 < h < 1.8 \mu\text{m}$
vs L (Fig. 4.18) -p=110mm-	always true	$L > 18 \mu\text{m}$	$L = 18 \mu\text{m}$	$40.4 < L < 49.4 \mu\text{m}$
Scaling experiments (Fig. 4.22)				
d = 3 $\mu\text{m}$	$p < 38.8 \mu\text{m}$	$p < 27.7 \mu\text{m}$	$p = 27.7 \mu\text{m}$	$36 < p < 45 \mu\text{m}$
d = 5 $\mu\text{m}$	$p < 64.8 \mu\text{m}$	$p < 35.7 \mu\text{m}$	$p = 35.7 \mu\text{m}$	$60 < p < 75 \mu\text{m}$
d = 10 $\mu\text{m}$	$p < 129.6 \mu\text{m}$	$p < 50.6 \mu\text{m}$	$p = 50.6 \mu\text{m}$	$90 < p < 120 \mu\text{m}$
d = 14 $\mu\text{m}$	$p < 181.4 \mu\text{m}$	$p < 59.8 \mu\text{m}$	$p = 58.8 \mu\text{m}$	$126 < p < 168 \mu\text{m}$
d = 20 $\mu\text{m}$	$p < 259.2 \mu\text{m}$	$p < 71.52 \mu\text{m}$	$p = 71.52 \mu\text{m}$	$150 < p < 180 \mu\text{m}$

Table 7.1 Test of Extrand's model on the experimental data of Chapter 4.

For this calculation, a 3- $\mu\text{L}$  drop was considered, and  $2b = \sqrt{2} p - d$ ,  $\theta_{adv} = 170^\circ$ ,  $\theta_{adv\ flat} = 116^\circ$  taken in the calculation.

---

Quantitative agreement with the experimental data presented in this work is not found, but the “contact line density” criterion predicts the right sense of evolution of the roughness with the experimental parameters (i.e. transition from Cassie to Wenzel with increasing  $p$ , decreasing  $d$ , increasing  $L$ , and increasing  $p/d$ ). However, it should be noted that also the Extrand model is based on the assumption of the drop hemisphericity, with no distortion of the drop base contact line, which would require a rigorous test in view of considering a “contact line density criterion” in the terms proposed by Extrand.

However, it can be affirmed that a thermodynamic analysis remains a more convincing approach, since it lays on a theoretical derivation, whereas Extrand’s model is based on still to be proven assumptions.





---

## APPENDIX 3: Comments on other literature data

*In this appendix the results of some selected experiments found in literature are compared to the thermodynamic approach presented in Chapter 4.*

### Experiments description

Some Cassie-Wenzel transitions as a function of a single roughness parameter have already been reported in literature, although the aim of their authors was neither to explain the position of the observed transition, nor to give a precise parameter value at which this transition should occur. However, it is interesting to observe that they are also correctly described by the thermodynamic interpretation presented in Chapter 4. Four cases briefly described and discussed.

### Yoshimitsu's experiments

Yoshimitsu et al. [44] reported a transition as function of pillar height. They studied square distributions of square pillars (pillar size: 50  $\mu\text{m}$ , spacing: 100  $\mu\text{m}$ ), varying pillar height from 10 to 182  $\mu\text{m}$ , and showed the transition from *wetted* to *composite* regime of 1- $\mu\text{L}$  droplets falling for height values comprised between 10 and 35  $\mu\text{m}$  (with  $\theta_{\text{flat}}=114^\circ$ ). In Fig. 7.1-A, the Yoshimitsu results are represented by the same thermodynamic approach adopted to discuss all the experimental results presented Chapter 4.

### Oner and McCarthy's experiments

Oner and McCarthy [37] reported the *composite-wetted* transitions in other two cases, as a function of a "scaling" parameter (pillar side/spacing), and as a function of "spacing" between consecutive pillars. In the first case, they considered square posts of 40  $\mu\text{m}$  height, in a hexagonal distribution (pillar size:  $x$ , spacing:  $2x$ ,  $x$  varied from 2 to 128  $\mu\text{m}$ ), and showed the transition falling at pillar size  $x$  comprised between 32 and 64  $\mu\text{m}$ . In the second case, they studied  $(8 \times 8)\text{-}\mu\text{m}^2$  square posts, 40- $\mu\text{m}$  height, in a square distribution as function of spacing

(varied between 16 and 56  $\mu\text{m}$ ), and showed the transition following at spacing 2x comprised between 32 and 56  $\mu\text{m}$ . The thermodynamic analysis is reported in Fig. 7.1-B and C respectively for the “scaling” and the “spacing” parameter.

## Jopp’s experiments

Jopp [70] observed a transition from the *wetted* to the *composite* regime as a function of pillar size for square posts, in a square distribution (height 100  $\mu\text{m}$ , spacing 200  $\mu\text{m}$ ) increasing the pillar side length from 40 to 80  $\mu\text{m}$ , with dynamic contact angle measurements with a maximum typical drop of 10  $\mu\text{L}$ . The proposed thermodynamic analysis is reported in Fig. 7.1-D.

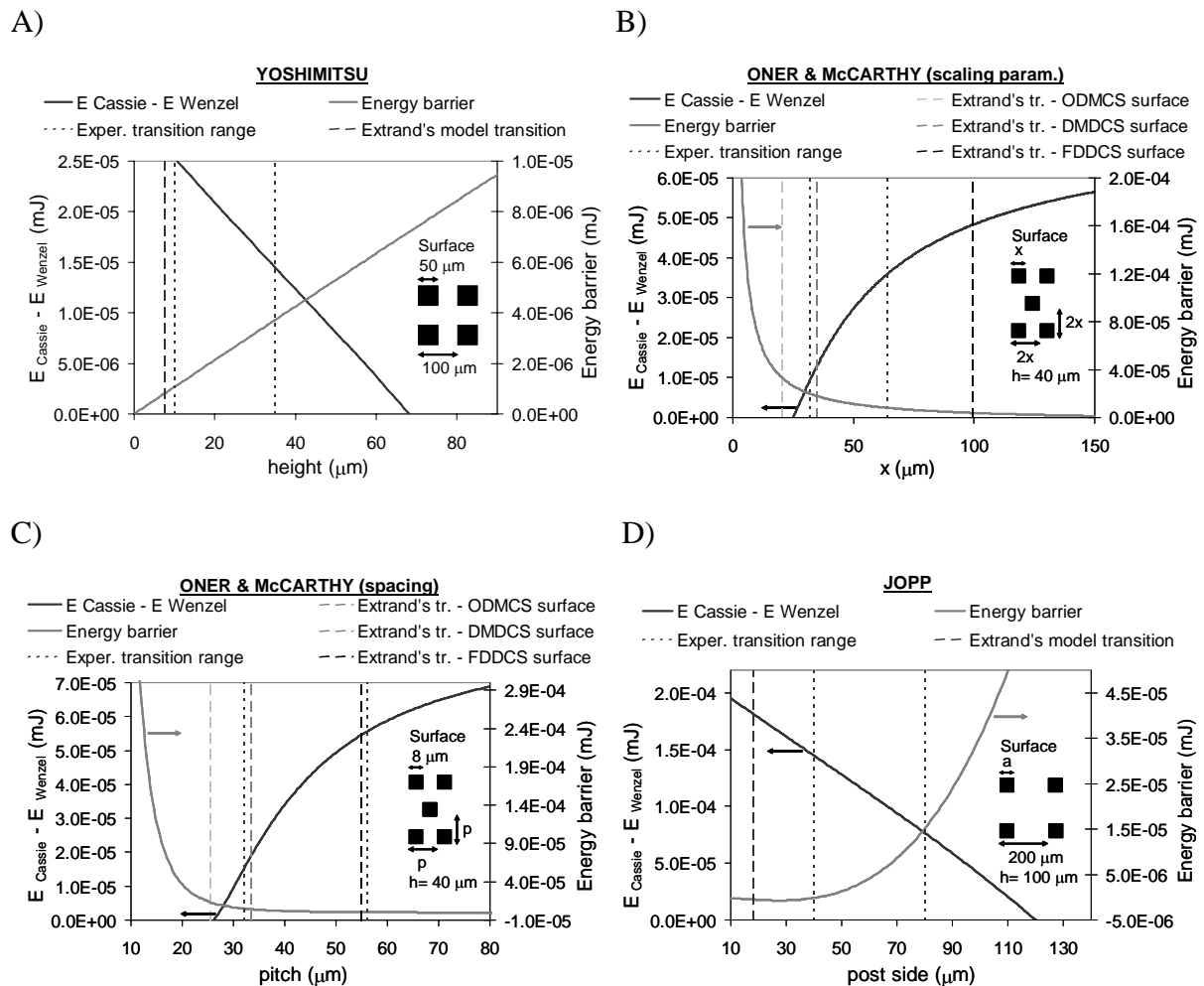


Fig. 7.1 *Thermodynamic analyses of literature data.* A) Experimental results of Yoshimitsu versus pillar height [44]; B) experimental results of Oner and McCarthy [37] versus the scaling parameter  $x$ , described in the inset; C) experimental results of Oner and McCarthy [37] versus spacing  $p$  (i.e. pitch), described in the inset; D) experimental results of Jopp [70] versus post side  $a$ , described in the inset. The transition predicted by Extrand’s model is also reported in all cases for comparison with the model developed in Chapter 4.

---

## Discussion

The thermodynamic analyses presented in Fig. 7.1 show no contradiction between the model presented in Chapter 4 and experimental data of other authors. It is interesting to note that:

1) in all cases, Cassie to Wenzel transitions are observed in the metastability Cassie region;

2) the values of the energy barrier to overcome for reaching the Wenzel thermodynamically favored state from the metastable Cassie state are higher than those calculated for the experimental results presented in this work in Chapter 4. This can possibly depend on the experimental procedure adopted for the drop deposition. In particular, in the dynamic measurements carried out by Oner and McCarthy, and Jopp, more energy is imparted to the drop than in the static measurements performed in this work;

3) the transitions expected from Extrand's model are also reported on each graph for comparison, showing that in all cases there is no quantitative agreement.



---

# REFERENCES

- [1] de Gennes, P.-G.; Brochard-Wyart, F.; Quéré, D., *Capillarity and Wetting phenomena: Drops, Bubbles, Pearls, Waves*. New York: Springer-Verlag, **2004**.
- [2] Barthlott, W. and C. Neinhuis, *Purity of the sacred lotus, or escape from contamination in biological surfaces*. *Planta*, **1997**, 202, 1-8.
- [3] Neinhuis, C. and Barthlott, W., *Characterization and distribution of water-repellent, self-cleaning plant surfaces*. *Annals of Botany* **1997**, 79, 667-677.
- [4] Blossey, R., *Self-cleaning surfaces - virtual realities*. *Nature Materials* **2003**, 2, 301-306.
- [5] Callies, M. and Quere, D., *On water repellency*. *Soft Matter* **2005**, 1, 55-61.
- [6] Martines, E.; Seunarine, K.; Morgan, H.; Gadegaard, N.; Wilkinson, C. D. W.; Riehle, M. O., *Superhydrophobicity and superhydrophilicity of regular nanopatterns*. *Nano Letters* **2005**, 5, 2097-2103.
- [7] Nakajima, A.; Hashimoto, K.; Watanabe, T., *Recent studies on super-hydrophobic films*. *Monatshefte Fur Chemie* **2001**, 132, 31-41.
- [8] Wenzel, R. N., *Resistance of Solid Surfaces to Wetting by Water*. *Industrial and Engineering Chemistry* **1936**, 28, 988-994.
- [9] Cassie, A. B. D.; Baxter, S., *Wettability of Porous Surfaces*. *Transactions of the Faraday Society* **1944**, 40, 546-551.
- [10] Cassie, A. B. D., *Contact Angles*. *Discussions of the Faraday Society* 1948, 3, 11-15.
- [11] R. Shuttleworth and G.L.J. Bailey, *The Spreading of a Liquid over a Rough Solid*. *Discussions of the Faraday Society* **1948**, 3, 16-22.
- [12] Good, R. J., *A Thermodynamic Derivation of Wenzels Modification of Youngs Equation for Contact Angles - Together with a Theory of Hysteresis*. *Journal of the American Chemical Society* **1952**, 74, 5041-5042.
- [13] Bartell, F. E.; Shepard, J. W., *Surface Roughness as Related to Hysteresis of Contact Angles .1. The System Paraffin Water Air*. *Journal of Physical Chemistry* **1953**, 57, 211-215.
- [14] Dettre, R. H.; Johnson, R. E., *Contact Angle Hysteresis. 2. Contact Angle Measurements on Rough Surfaces*. *Contact angle, Wettability and Adhesion - Advances in Chemistry Series No. 43* **1964**, 136-144.
- [15] Johnson, R. E. and Dettre, R. H., *Contact Angle Hysteresis. 1. Study of an Idealized Rough Surface*. *Contact angle, Wettability and Adhesion - Advances in Chemistry series No. 43* **1964**, 112-135.
- [16] Johnson, R. E. and Dettre, R. H., *Contact Angle Hysteresis. III. Study of an Idealized Heterogeneous Surface*. *The Journal of Physical Chemistry* **1964**, 68, 1744-1750.

- 
- [17] Dettre, R. H. and Johnson, R. E., *Contact Angle Hysteresis. IV. Contact Angle Measurements on Heterogeneous Surfaces*. The Journal of Physical Chemistry **1965**, 69, 1507-1515.
- [18] Dettre, R. H. and Johnson, R. E., *Contact Angle Hysteresis - Porous Surfaces*. Society of Chemical Industry **1967**, Monograph N. 25, 144-163
- [19] Huh, C.; Mason, S. G., *Effects of Surface-Roughness on Wetting (Theoretical)*. Journal of Colloid and Interface Science **1977**, 60, 11-38
- [20] Hitchcock, S. J.; Carroll, N. T.; Nicholas, M. G., *Some Effects of Substrate Roughness on Wettability*. Journal of Materials Science **1981**, 16, 714-732.
- [21] Morra, M.; Occhiello, E.; Garbassi, F., *Contact-Angle Hysteresis in Oxygen Plasma Treated Poly(Tetrafluoroethylene)*. Langmuir **1989**, 5, 872-876.
- [22] Hazlett, R. D., *Fractal Applications - Wettability and Contact-Angle*. Journal of Colloid and Interface Science **1990**, 137, 527-533.
- [23] Drelich J. and Miller J. D., *The Effect of Surface Heterogeneity on Pseudo-Line Tension and the Flotation Limit of Fine Particles*. Colloids and Surfaces **1992**, 69, 35-43.
- [24] Drelich, J.; Miller, J. D., *Modification of the Cassie Equation*. Langmuir **1993**, 9, 619-621.
- [25] Drelich, J.; Miller, J. D., *The Effect of Solid-Surface Heterogeneity and Roughness on the Contact-Angle Drop (Bubble) Size Relationship*. Journal of Colloid and Interface Science **1994**, 164, 252-259.
- [26] Drelich, J.; Wilbur, J. W.; Miller, J. D.; Whitesides, G. M., *Contact Angles for Liquid Drops at a Model Heterogeneous Surface Consisting of Alternating and Parallel Hydrophobic/Hydrophilic Strips*. Langmuir **1996**, 12, 1913-1922.
- [27] Onda, T.; Shibuichi, S.; Satoh, N.; Tsujii, K., *Super-water-repellent fractal surfaces*. Langmuir **1996**, 12, 2125-2127.
- [28] Shibuichi, S.; Onda, T.; Satoh, N.; Tsujii, K., *Super water-repellent surfaces resulting from fractal structure*. Journal of Physical Chemistry **1996**, 100, 19512-19517.
- [29] Shibuichi, S.; Yamamoto, T.; Onda, T.; Tsujii, K., *Super water- and oil-repellent surfaces resulting from fractal structure*. Journal of Colloid and Interface Science **1998**, 208, 287-294.
- [30] Tadanaga, K.; Katata, N.; Minami, T., *Formation Process of Super-Water-Repellent Al<sub>2</sub>O<sub>3</sub> Coating Films with High Transparency by Sol-Gel Method*. Journal of American Ceramic Society **1997**, 80, 3213-3216.
- [31] Hozumi, A.; Takai, O., *Preparation of ultra water-repellent films by microwave plasma-enhanced CVD*. Thin Solid Films **1997**, 303, 222-225.
- [32] Swain, P. S.; Lipowsky, R., *Contact angles on heterogeneous surfaces: A new look at Cassie's and Wenzel's laws*. Langmuir **1998**, 14, 6772-6780.
- [33] Marmur, A., *Line tension effect on contact angles: Axisymmetric and cylindrical systems with rough or heterogeneous solid surfaces*. Colloids and Surfaces A - Physicochemical and Engineering Aspects **1998**, 136, 81-88.
- [34] Nakae, H., Inui, Y., Hirata, and H. Saito, *Effects of surface roughness on wettability*. Acta Materialia **1998**, 46, 2313-2318.
-

- 
- [35] Bico, J.; Marzolin, C.; Quere, D., *Pearl drops*. *Europhysics Letters* **1999**, 47, 220-226.
- [36] Chen, W.; Fadeev, A. Y.; Hsieh, M. C.; Oner, D.; Youngblood, J.; McCarthy, T. J., *Ultrahydrophobic and ultralyophobic surfaces: Some comments and examples*. *Langmuir* **1999**, 15, 3395-3399.
- [37] Oner, D.; McCarthy, T. J., *Ultrahydrophobic surfaces. Effects of topography length scales on wettability*. *Langmuir* **2000**, 16, 7777-7782.
- [38] Lipowsky, R.; Lenz, P.; Swain, P. S., *Wetting and dewetting of structured and imprinted surfaces*. *Colloids and Surfaces A - Physicochemical and Engineering Aspects* **2000**, 161, 3-22.
- [39] Herminghaus, S., *Roughness-induced non-wetting*. *Europhysics Letters* **2000**, 52, 165-170.
- [40] Nakajima, A.; Hashimoto, K.; Watanabe, T., *Recent studies on super-hydrophobic films*. *Monatshefte Fur Chemie* **2001**, 132, 31-41.
- [41] Mahadevan, L., *Non-stick water*. *Nature* **2001**, 411, 895-896.
- [42] Extrand, C. W., *Model for contact angles and hysteresis on rough and ultraphobic surfaces*. *Langmuir* **2002**, 18, 7991-7999.
- [43] Feng, L.; Li, S. H.; Li, Y. S.; Li, H. J.; Zhang, L. J.; Zhai, J.; Song, Y. L.; Liu, B. Q.; Jiang, L.; Zhu, D. B., *Super-hydrophobic surfaces: From natural to artificial*. *Advanced Materials* **2002**, 14, 1857-1860.
- [44] Yoshimitsu, Z.; Nakajima, A.; Watanabe, T.; Hashimoto, K., *Effects of surface structure on the hydrophobicity and sliding behavior of water droplets*. *Langmuir* **2002**, 18, 5818-5822.
- [45] Marmur, A., *Wetting on real surfaces*. *Journal of Imaging Science and Technology* 2000, 44, 406-409.
- [46] Marmur, A., *Wetting on hydrophobic rough surfaces: To be heterogeneous or not to be?* *Langmuir*, **2003**, 19, 8343-8348.
- [47] Lafuma, A.; Quere, D., *Superhydrophobic states*. *Nature Materials* **2003**, 2, 457-460.
- [48] Quere, D.; Lafuma, A. and Bico, J. *Slippy and sticky microtextured solids*. *Nanotechnology*, **2003**, 14, 1109-1112.
- [49] Patankar, N. A., *On the modeling of hydrophobic contact angles on rough surfaces*. *Langmuir*, **2003**, 19, 1249-1253.
- [50] He, B.; Patankar, N. A.; Lee, J., *Multiple equilibrium droplet shapes and design criterion for rough hydrophobic surfaces*. *Langmuir* **2003**, 19, 4999-5003.
- [51] Patankar, N. A., *Transition between Superhydrophobic States on Rough Surfaces*. *Langmuir* **2004**, 20, 7097-7102.
- [52] Krupenkin, T. N.; Taylor, J. A.; Schneider, T. M.; Yang, S., *From Rolling Ball to Complete Wetting: The Dynamic Tuning of Liquids on Nanostructured Surfaces*. *Langmuir* **2004**, 20, 3824-3827.
- [53] He, B.; Lee, J.; Patankar, N. A., *Contact angle hysteresis on rough hydrophobic surfaces*. *Colloids and Surfaces A - Physicochemical and Engineering Aspects* **2004**, 248, 101-104.
-

- 
- [54] Patankar, N. A., *Mimicking the Lotus Effect: Influence of Double Roughness Structures and Slender Pillars*. Langmuir **2004**, 20, 8209-8213.
- [55] Extrand, C. W., *Criteria for Ultralyophobic Surfaces*. Langmuir **2004**, 20, 5013-5018.
- [56] Blossey, R., *Self-cleaning surfaces - virtual realities*. Nature Materials **2003**, 2, 301-306.
- [57] Barbieri, L.; Kulik, G.; Hoffmann, P.; Gaillard, C.; van der Lee, A.; Mathieu, H.-J.; Pfeffer, M., *Flow circuit gas-phase silanization and characterization of highly non-wetting molecular coating*. Thin Solid Films **2006**, submitted for publication.
- [58] Hare, E. F.; Shafrin, E. G.; Zisman, W. A. *Properties of Films of Adsorbed Fluorinated Acids*. Journal of Physical Chemistry **1954**, 58, 236-239.
- [59] Zisman, W. A., *Relation of the Equilibrium Contact Angle to Liquid and Solid Constitution*. Contact Angle, Wettability, and Adhesion - Advances in Chemistry Series No 43, **1964**, 1-51.
- [60] Srinivasan, U.; Houston, M. R.; Howe, R. T.; Maboudian, R., *Alkyltrichlorosilane-Based Self-Assembled Monolayer Films for Stiction Reduction in Silicon Micromachines*. Journal of Microelectromechanical Systems **1998**, 7, 252-260.
- [61] Hong, B. S.; Han, J. H.; Cho, Y. J.; Park, M. S.; Dolukhanyan, T.; Sung, C., *Endurable water-repellent glass for automobiles*. Thin Solid Films **1999**, 351, 274-278.
- [62] Akamatsu, Y.; Makita, K.; Hinaba, H.; Minami, T., *Water-repellent coating films on glass prepared from hydrolysis and polycondensation reaction of fluoroalkyltrialkoxysilane*. Thin Solid Films **2001**, 389, 138-145.
- [63] Ashurst, W. R.; Yau, C.; Carraro, C.; Lee, C.; Kluth, G. J.; Howe, R. T.; Maboudian, R., *Alkene based monolayer films as anti-stiction coatings for polysilicon MEMS*. Sensors and Actuators A **2001**, 91, 239-248.
- [64] Fadeev, A. Y.; Soboleva, O. A.; Summ, B. D., *Wettability of Organosilicon and Organofluorosilicon Monolayers Covalently Grafted on Quartz*. Colloid Journal **1997**, 59, 222-225.
- [65] Hozumi, A.; Ushiyama, K.; Sugimura, H.; Takai, O., *Fluoroalkylsilane Monolayer Formed by Chemical Vapor Surface Modification on Hydroxylated Oxide Surfaces*. Langmuir **1999**, 15, 7600-7604.
- [66] Schondelmaier, D.; Cramm, S.; Klingeler, R.; Morenzin, J.; Zilkens, C.; Eberhardt, W., *Orientation and Self-Assembly of Hydrophobic Fluoroalkylsilanes*. Langmuir **2002**, 18, 6242-6245.
- [67] Morra, M.; Occhiello, E.; Garbassi, F., *Contact-Angle Hysteresis in Oxygen Plasma Treated Poly(Tetrafluoroethylene)*. Langmuir **1989**, 5, 872-876.
- [68] Miwa, M.; Nakajima, A.; Fujishima, A.; Hashimoto, K.; Watanabe, T., *Effects of the surface roughness on sliding angles of water droplets on superhydrophobic surfaces*. Langmuir **2000**, 16, 5754-5760.
- [69] Erbil, H. Y.; Demirel, A. L.; Avci, Y.; Mert, O., *Transformation of a Simple Plastic into a Superhydrophobic Surface*. Science **2003**, 299, 1377-1380.
- [70] Jopp, J.; Gröll, H.; Yeruslami-Rozen, R., *Wetting Behavior of Water Droplets on Hydrophobic Microtextures of Comparable Size*. Langmuir **2004**, 20, 10015-10019.
-



- 
- [71] Ou, J.; Perot, B.; Rothstein, P., *Laminar drag reduction in microchannels using ultrahydrophobic surfaces*. *Physics of Fluids* **2004**, 16, 4635-4643.
- [72] Callies, M.; Chen, Y.; Marty, F.; Pépin, A.; Quéré, D., *Microfabricated textured surfaces for super-hydrophobicity investigations*. *Microelectronic Engineering* **2005**, 78-79, 100-105.
- [73] Lee, J.; He, B.; Patankar, N. A., *A roughness-based wettability switching membrane device for hydrophobic surfaces*. *Journal of Micromechanical Microengineering* **2005**, 15, 591-600.
- [74] Jeong, H. E.; Lee, S. H.; Kim, J. K.; Suh, K. Y., *Nanoengineered Multiscale Hierarchical Structures with Tailored Wetting Properties*. *Langmuir* **2006**, 22, 1640-1645.
- [75] Li, H.; Wang, X.; Song, Y.; Liu, Y.; Li, Q.; Jiang, L.; Zhu, D. B., *Super-Amphiphobic Aligned Carbon Nanotube Films*. *Angewandte Chemie* **2001**, 113, 1793-1796.
- [76] Lau, K. K. S.; Bico, J.; Teo, K. B. K.; Chhowalla, M.; Amaratunga, G. A. J.; Milne, W. I.; McKinley, G. H.; Gleason, K. K., *Superhydrophobic carbon nanotube forests*. *Nano Letters* **2003**, 3, 1701-1705.
- [77] Fan, J.-G.; Tang, X.-J.; Zhao, Y.-P., *Water contact angles of vertically aligned Si nanorod arrays*. *Nanotechnology* **2004**, 15, 501-504.
- [78] Tsoi, S.; Fok, E.; Sit, J. C.; Veinot, J. G. C., *Superhydrophobic, High Surface Area, 3-D SiO<sub>2</sub> Nanostructures through Siloxane-Based Surface Functionalization*. *Langmuir* **2004**, 20, 10771-10774.
- [79] Young, T., *An essay on the cohesion of fluids*. *Philosophical Transactions of the Royal Society of London* **1805**, 95, 65-87.
- [80] Quéré, D., *Non-sticking drops*. *Reports on Progress in Physics* **2005**, 68, 2495-2532.
- [81] Wolansky, G.; Marmur, A., *The actual contact angle on a heterogeneous rough surface in three dimensions*. *Langmuir* **1998**, 14, 5292-5297.
- [82] Wolansky, G.; Marmur, A., *Apparent contact angle on rough surfaces: the Wenzel equation revisited*. *Colloids and Surface A* **1999**, 156, 381-388.
- [83] Huang, L.; Lau, S. P.; Yang, H. Y.; Leong, E. S. P.; Yu, S. F.; Prawer, S., *Stable superhydrophobic surface via carbon nanotubes coated with a ZnO thin film*. *Journal of Physical Chemistry B* **2005**, 109, 7746-7748.
- [84] Brandon, S.; Haimovich, N.; Yeger, E.; Marmur, A., *Partial wetting of chemically patterned surfaces: The effect of drop size*. *Journal of Colloid and Interface Science* **2003**, 263, 237-243.
- [85] Busscher, H. J.; Vanpelt, A. W. J.; Deboer, P.; Dejong, H. P.; Arends, J., *The Effect of Surface Roughening of Polymers on Measured Contact Angles of Liquids*. *Colloids and Surfaces* **1984**, 9, 319-331.
- [86] Sun, T. L.; Wang, G. J.; Feng, L.; Liu, B. Q.; Ma, Y. M.; Jiang, L.; Zhu, D. B., *Reversible switching between superhydrophilicity and superhydrophobicity*. *Angewandte Chemie-International Edition* **2004**, 43, 357-360.
- [87] Liu, H.; Feng, L.; Zhai, J.; Jiang, L.; Zhu, D., *Reversible wettability of a chemical vapor deposition prepared ZnO film between superhydrophobicity and superhydrophilicity*. *Langmuir* **2004**, 20, 5659-5661.
-

- 
- [88] Yu, X.; Wang, Z.; Jiang, Y.; Shi, F.; Zhang, X., *Reversible pH-responsive surface: From superhydrophobicity to superhydrophilicity*. *Advanced Materials* **2005**, *17*, 1289-1293.
- [89] Hitchcock, S. J.; Carroll, N. T. ; Nicholas, M. G., *Some Effects of Substrate Roughness on Wettability*. *Journal of Materials Science* **1981**, *16*, 714-732.
- [90] Kijlstra, J.; Reihls, K.; Klamt, A., *Roughness and topology of ultra-hydrophobic surfaces*. *Colloids and Surfaces A* **2002**, *206*, 521-529.
- [91] Lundgren, M.; Allan, N. L.; Cosgrove, T.; George, N., *Molecular dynamics study of wetting of a pillar surface*. *Langmuir* **2003**, *19*, 7127-7129.
- [92] Bico, J.; Tordeux, C.; Quéré, D., *Rough wetting*. *Europhysics Letters* **2001**, *55*, 214-220.
- [93] Ishino, C.; Okumura, K.; Quéré, D., *Wetting transitions on rough surfaces*. *Europhysics Letters* **2004**, *68*, 419-425.
- [94] Quéré, D., *Surface chemistry - Fakir droplets*. *Nature Materials* **2002**, *1*, 14-15.
- [95] Extrand, C. W., *Designing for Optimum Liquid Repellency*. *Langmuir* **2006**, *22*, 1711-1714.
- [96] Richard, D. and Quéré, D., *Viscous drops rolling on a tilted non-wettable solid*. *Europhysics Letters* **1999**, *48*, 286-291.
- [97] Cox, R. G., *The spreading of a liquid on a rough solid surface*. *Journal of Fluid Mechanics* **1983**, *131*, 1-26.
- [98] Li, D.; Neumann, A. W., *Surface heterogeneity and contact angle hysteresis*. *Colloid Polymer Science* **1992**, *270*, 498-504.
- [99] Joanny, J. F. and de Gennes, P. G., *A model for contact angle hysteresis*. *Journal of Physical Chemistry* **1985**, 552-562.
- [100] de Gennes, P. G., *Wetting: statics and dynamics*. *Reviews on Modern Physics* **1985**, *57*, 827-863
- [101] Marmur, A., *Thermodynamic aspects of contact angle hysteresis*. *Advances in Colloid and Interface Science* **1994**, *50*, 121-141.
- [102] Good, R. J. and Koo, M. N., *The effect of drop size on contact angle*. *Journal of Colloid and Interface Science* **1979**, *71*, 283-292.
- [103] Drelich, J.; Miller, J. D.; Hupka, J., *The effect of drop size on contact angle over a wide range of drop volumes*. *Journal of Colloids and Interface Science* **1993**, *155*, 379-385.
- [104] Marmur, A., *Contact angle hysteresis on heterogeneous smooth surfaces*. *Journal of Colloid and Interface Science* **1994**, *168*, 40-46.
- [105] Drelich, J.; Miller, J. D.; Good, R. J., *The Effect of Drop (Bubble) Size on Advancing and Receding Contact Angles for Heterogeneous and Rough Solid Surfaces as Observed with Sessile-Drop and Captive-Bubble Techniques*. *Journal of Colloids and Interface Science* **1996**, *179*, 37-50.
- [106] Ruckenstein, E. and Gourisankar, S. V., *Environmentally induced restructuring of polymer surfaces and its influence on their wetting characteristics in an aqueous environment*. *Journal of Colloid and Interface Science* **1985**, *107*, 488-502.
- [107] Shanahan, M. E. R. and Carre, A., *Viscoelastic Dissipation in Wetting and Adhesion Phenomena*. *Langmuir* **1995**, *11*, 1396-1402.
-

- 
- [108] Extrand, C. W. and Kumagai, Y., *Contact Angles and Hysteresis on Soft Surfaces*. Journal of Colloid and Interface Science **1996**, 184, 191-200.
- [109] Timmons, C. O. and Zisman, W. A., *The effect of liquid structure on contact angle hysteresis*. Journal of Colloid and Interface Science **1966**, 22, 165-171.
- [110] Vergelati, C.; Perwuelz, A.; Vovelle, L.; Romero, M. A.; Holl, Y., *Poly(ethylene terephthalate) surface dynamics in air and water studied by tensiometry and molecular modelling*. Polymer **1994**, 35, 262-270.
- [111] Neumann, A. W. and Good, R. J., *Thermodynamics of contact angles I. Heterogeneous solid surfaces*. Journal of Colloids and Interface Science **1972**, 38, 341-358.
- [112] Huh, C.; Mason, S. G., *Effect of surface roughness on wetting (theoretical)*. Journal of Colloids and Interface Science **1977**, 60, 11-38.
- [113] Schwartz, L. W. and Garoff, S., *Contact angle hysteresis on heterogeneous surfaces*. Langmuir **1985**, 1, 219-230.
- [114] Extrand, C. W., *Contact Angles and Their Hysteresis as a Measure of Liquid-Solid Adhesion*. Langmuir **2004**, 20, 4017-4021.
- [115] Extrand, C. W. and Kumagai, Y., *An experimental study of contact angle hysteresis*. Journal of Colloid and Interface Science **1997**, 194, 378-383.
- [116] McHale, G.; Shirtcliffe, N. J.; Newton, M. I., *Contact-Angle Hysteresis on Superhydrophobic Surfaces*. Langmuir **2004**, 20, 10146-10149.
- [117] Li, W.; Amirfazli, A., *A thermodynamic approach for determining the contact angle hysteresis for superhydrophobic surfaces*. Journal of Colloid and Interface Science **2005**, 292, 195-201.
- [118] Roura, P.; Fort, J., *Comment on "effects of the surface roughness on sliding angles of water droplets on superhydrophobic surfaces"*. Langmuir **2002**, 18, 566-569.
- [119] Li, D., *Drop size dependence of contact angles and line tensions of solid-liquid systems*. Colloids and Surfaces A **1996**, 116, 1-23.
- [120] Widom, B., *Line Tension and the Shape of a Sessile Drop*. Journal of Physical Chemistry **1995**, 99, 2803-2806.
- [121] Malcolm, J. D.; Paynter, H. M., *Simultaneous Determination of Contact-Angle and Interfacial-Tension from Sessile Drop Measurements*. Journal of Colloid and Interface Science **1981**, 82, 269-275.
- [122] Mahadevan, L.; Pomeau, Y., *Rolling droplets*. Physics of Fluids **1999**, 11, 2449-2453.
- [123] Chatterjee, J., *Limiting conditions for applying the spherical section assumption in contact angle estimation*. Journal of Colloid and Interface Science **2003**, 259, 139-147.
- [124] Yang, M. W. and Lin, S. Y., *A method for correcting the contact angle from the theta/2 method*. Colloids and Surfaces A **2003**, 220, 199-210.
- [125] Cheng, P.; Li, D.; Boruvka, L.; Rotenberg, Y.; Neumann, A. W., *Automation of Axisymmetric Drop Shape-Analysis for Measurement of Interfacial-Tensions and Contact Angles*. Colloids and Surfaces **1990**, 43, 151-167.
- [126] Li, D.; Cheng, P.; Neumann, A. W., *Contact-Angle Measurement by Axisymmetrical Drop Shape-Analysis (ADSA)*. Advances in Colloid and Interface Science **1992**, 39, 347-382.
-

- 
- [127] Girault, H. H.; Schiffrin, D. J.; Smith, B. D. V., *Drop Image-Processing for Surface and Interfacial-Tension Measurements*. Journal of Electroanalytical Chemistry **1982**, 137, 207-217.
- [128] Spelt, J. K.; Rotenberg, Y.; Absolom, D. R.; Neumann, A. W., *Sessile-Drop Contact-Angle Measurements Using Axisymmetrical Drop Shape-Analysis*. Colloids and Surfaces **1987**, 24, 127-137.
- [129] Hoorfar, M.; Neumann, A. W., *Axisymmetric Drop Shape Analysis (ADSA) for the Determination of Surface Tension and Contact Angle*. The Journal of Adhesion **2004**, 80, 727-743.
- [130] Skinner, F. K.; Rotenberg, Y.; Neumann, A. W., *Contact-Angle Measurements from the Contact Diameter of Sessile Drops by Means of a Modified Axisymmetric Drop Shape-Analysis*. Journal of Colloid and Interface Science **1989**, 130, 25-34.
- [131] Iliev S. D.; Pesheva, N. C., *Wetting properties of well-structured heterogeneous substrates*. Langmuir **2003**, 19, 9923-9931.
- [132] Sakai, H.; Fujii, T., *The dependence of the apparent contact angles on gravity*. Journal of Colloid and Interface Science **1999**, 210, 152-156.
- [133] Pompe, T. and Herminghaus, S., *Three-phase contact line energetics from nanoscale liquid surface topographies*. Physical Review Letters **2000**, 85, 1930-1933.
- [134] Babak, V. G., *Generalised line tension theory revisited*. Colloids and Surfaces A **1999**, 156, 423-448.
- [135] Boruvka, L.; Neumann, A. W., *Generalization of Classical-Theory of Capillarity*. Journal of Chemical Physics **1977**, 66, 5464-5476.
- [136] Drelich, J., *The significance and magnitude of the line tension in three-phase (solid-liquid-fluid) systems*. Colloids and Surfaces A **1996**, 116, 43-54.
- [137] Xia, F.; Gray, W. G.; Chen, P., *Thermodynamic fundamental equation of contact lines: selection of independent variables*. Journal of Colloid and Interface Science **2003**, 261, 464-475.
- [138] Toshev, B. V.; Platikanov, D.; Scheludko, A., *Line Tension in 3-Phase Equilibrium Systems*. Langmuir **1988**, 4, 489-499.
- [139] Gaydos, J. and Neumann, A. W., *The Dependence of Contact Angles on Drop Size and Line Tension*. Journal of Colloid and Interface Science **1987**, 120, 76-86.
- [140] Duncan, D.; Li, D.; Gaydos, J.; Neumann, A. W., *Correlation of Line Tension and Solid-Liquid Interfacial-Tension from the Measurement of Drop Size Dependence of Contact Angles*. Journal of Colloid and Interface Science **1995**, 169, 256-261.
- [141] Amirfazli, A.; Hanig, S.; Muller, A.; Neumann, A. W., *Measurements of line tension for solid-liquid-vapor systems using drop size dependence of contact angles and its correlation with solid-liquid interfacial tension*. Langmuir **2000**, 16, 2024-2031.
- [142] Amirfazli, A.; Kwok, D. Y.; Gaydos, J.; Neumann, A. W., *Line tension measurements through drop size dependence of contact angle*. Journal of Colloid and Interface Science **1998**, 205, 1-11.
- [143] Marmur, A., *Equilibrium contact angles: Theory and measurement*. Colloids and Surfaces A **1996**, 116, 55-61.

- 
- [144] Marmur, A., *Line tension and intrinsic contact angle in solid-liquid-fluid systems*. Journal of colloids and interface science **1997**, 186, 462-466.
- [145] Shirtcliffe, N.; McHale, G.; Newton, M. I.; Chabrol, G.; Perry, C. C., *Dual-scale Roughness Produces Unusually Water-Repellent Surfaces*. Advanced Materials **2004**, 16, 1929-1932.
- [146] Zhu, L.; Xiu, Y.; Xu, J.; Tamirisa, P. A.; Hess, D. W.; Wong, C.-P., *Superhydrophobicity on Two-Tier Rough Surfaces Fabricated by Controlled Growth of Aligned Carbon Nanotube Arrays Coated with Fluorocarbon*. Langmuir **2005**, 21, 11208-11212.
- [147] Whiteside, G. M.; Grzybowski, B., *Self-Assembly at All Scales*. Science **2002**, 295, 2418-2421.
- [148] Clark, T. D.; Ferrigno, R.; Tien, J.; Paul, E. K.; Whiteside, G. M., *Template-Directed Self-Assembly of 10- $\mu$ m-Sized Hexagonal Plates*. Journal of American Chemical Society **2002**, 124, 5419-5426.
- [149] Biederman, H.; Bilkova, P.; Jezek, J.; Hlidek, P.; Slavinska, D., *RF magnetron sputtering of polymers*. Journal of Non-Crystalline Solids **1997**, 218, 44-49.
- [150] Biederman, H.; Stelmashuk, V.; Kholodkov, I.; Choukourov, A.; Slavinska, D., *RF sputtering of hydrocarbon polymers and their derivatives*. Surface and Coatings Technology **2003**, 174, 27-32.
- [151] Youngblood, J. and McCarthy, T. J., *Ultrahydrophobic Polymer Surfaces Prepared by Simultaneous Ablation of Polypropylene and Sputtering of Poly(tetrafluoroethylene) Using Radio Frequency Plasma*. Macromolecules **1999**, 32, 6800-6806.
- [152] Hirayama, M. K. N.; Caseri, W. R.; Suter, U. W., *Strongly attached ultrathin polymer layers on metal surfaces obtained by activation of Si-H bonds*. Applied Surface Science **1999**, 143, 256-264.
- [153] Haas, K.-H.; Amberg-Schwab, S.; Rose, K., *Functionalized coating materials based on inorganic-organic polymers*. Thin Solid Films **1999**, 351, 198-203.
- [154] Veeramasuneni, S.; Drelich, J.; Miller, J. D.; Yamauchi, G., *Hydrophobicity of ion-plated PFTE coatings*. Progress in Organic Coatings **1997**, 31, 265-270.
- [155] Hozumi, A. and Takai, O., *Preparation of ultra water-repellent films by microwave plasma-enhanced CVD*. Thin Solid Films **1997**, 303, 222-225.
- [156] Takay, O.; Hozumi, A.; Sugimoto, N., *Coating of transparent water-repellent thin films by plasma-enhanced CVD*. Journal of Non-Crystalline Solids **1997**, 218, 280-285.
- [157] Ulman, A., *An Introduction to Ultrathin Organic Films - from Langmuir-Blodgett to Self-Assembly*. United Kingdom Edition, ed. **1991**, Academic Press.
- [158] Ulman, A., *Formation and Structure of Self-Assembled Monolayers*. Chemical Reviews **1996**, 96, 1533-1554.
- [159] Boksanyi, L.; Liardon, O.; Kovats, E.s., *Chemically modified silicon dioxide surfaces. Reaction of n-alkyldimethylsilanols and n-oxaalkyldimethylsilanols with the hydrated surface of silicon dioxide. The question of the limiting surface concentration*. Advances in Colloid and Interface Science **1976**, 6, 95-137.
- [160] Riedo, F.; Czencz, M.; Liardon, O.; Kovats, E.s., *Chemically modified silicon dioxide surfaces. Wetting properties of compact n-alkyl-dimethylsiloxy layers, and their mixed*
-

- 
- surface crystals. The question of wetting of molecularly rough and of swollen surfaces.* Helvetica Chimica Acta **1978**, 61, 1912-1941.
- [161] Sagiv, J., *Organized Monolayers by Adsorption. 1. Formation and Structure of Oleophobic Mixed Monolayers on Solid Surfaces.* Journal of American Chemical Society **1980**, 102, 92-98.
- [162] Pomerantz, M.; Segmuller, A.; Netzer, L.; Sagiv, J., *Coverage of Si substrates by self-assembling monolayers and multilayers as measured by IR, wettability and X-ray diffraction.* Thin Solid Films **1985**, 132, 153-162.
- [163] Silberzan, P.; Léger, L.; Ausserré, D.; Benattar, J. J., *Silanization of Silica Surfaces. A New Method of Constructing Pure or Mixed Monolayers.* Langmuir **1991**, 7, 1647-1651.
- [164] Brzoska, J. B.; Shahidzadeh, N.; Rondelez, F., *Evidence of a transition temperature for the optimum deposition of grafted monolayer coatings.* Nature **1992**, 360, 719-721.
- [165] Brzoska, J. B.; Azouz, I. B.; Rondelez, F., *Silanization of Solid Substrates: A Step toward Reproducibility.* Langmuir **1994**, 10, 4367-4373.
- [166] Rye, R. R., *Transition Temperature n-Alkyltrichlorosilane Monolayers.* Langmuir **1997**, 13, 2588-2590.
- [167] Tripp, C. P.; Hair, M. L., *Reaction of Chloromethylsilanes with Silica: A Low-Frequency Infrared Study.* Langmuir **1991**, 7, 923-927.
- [168] Rye, R. R.; Nelson, G. C.; Dugger, M. T., *Mechanistic Aspect of Alkylchlorosilane Coupling Reactions.* Langmuir **1997**, 13, 2965-2972.
- [169] McGovern, M.; Kallury, K. M. R.; Thompson, M., *Role of solvent on the silanization of glass with octadecyltrichlorosilane.* Langmuir **1994**, 10, 3607-3614.
- [170] Szabo', K.; Ha, N. L.; Schneider, P.; Zeltner, P.; Kovats, E.s., *Monofunctional (Dimethylamino)silane as Silylating Agent.* Helvetica Chimica Acta **1984**, 67, 2128-2142.
- [171] Wasserman, S. R.; Tao, Y.-T.; Whiteside, G. M., *Structure and Reactivity of Alkylsiloxane Monolayers Formed by Reaction of Alkyltrichlorosilane on Silicon Substrates.* Langmuir **1989**, 5, 1074-1087.
- [172] Banga, R.; Yarwood, J.; Morgan, A. M.; Evans, B.; Kells, J., *In-situ FTIR studies of the kinetics ad self assembly of alkyl and perfluoroalkyl trichlorosilanes on silicon.* Thin Solid Films **1996**, 284-285, 261-266.
- [173] Vallant, T.; Kattner, J.; Brunner, H.; Mayer, U.; Hoffmann, H., *Investigation of the Formation and Structure of Self-assembled Alkylsiloxane Monolayers on Silicon Using In Situ Attenuated Total Reflection Infrared Spectroscopy.* Langmuir **1999**, 15, 5339-5346.
- [174] Richter, A. G., *In situ Interrupted Growth Studies of Self-Assembled Monolayers Using X-ray Reflectivity.* Ph.D. Dissertation, Northwestern University: Evanston, Illinois, 2000.
- [175] Burkhard, C. A.; Rochow, E. G.; Booth, H. S.; Hartt, J., *The present state of organosilicon chemistry.* Chemical Reviews **1947**, 41, 97-149.
-

- 
- [176] Banga, R.; Yarwood, J., *FTIR and AFM Studies of the Kinetics and Self Assembly of Alkyltrichlorosilane and (Perfluoroalkyl)trichlorosilane onto Glass and Silicon*. *Langmuir* **1995**, 11, 4393-4399.
- [177] Duchet, J.; Chabert, B.; Chapel, J. P.; Gérard, J. F.; Chevelon, J. M.; Jaffrezic-Renault, N., *Influence of the Deposition Process on the Structure of Grafted Alkylsilane Layers*. *Langmuir* **1997**, 13, 2271-2278.
- [178] Hoffmann, P. W.; Stelzle, M.; Rabolt, J. F., *Vapor Phase Self-Assembly of Fluorinated Monolayers on Silicon and Germanium Oxide*. *Langmuir* **1997**, 13, 1877-1880.
- [179] Dussan, V. E. B., *On the spreading of liquids on solid surfaces: static and dynamic contact lines*. *Annual Review on Fluid Mechanics* **1979**, 11, 371-400.
- [180] Kwok, D. Y.; Neumann, A. W., *Contact angle measurement and contact angle interpretation*. *Advances in Colloid and Interface Science* **1999**, 81, 167-249.
- [181] Korosi, G.; Kovats, E.s., *Density and surface tension of 83 organic liquids*. *Journal of Chemical & Engineering Data* **1981**, 26, 323-332.
- [182] Iler, R. K., *The Chemistry of Silica*. John Wiley & Sons, **1979**, Chapter 6.
- [183] Leyden, D. E., *Silica Surface*. In “*Silanes, Surfaces, and Interfaces Symposium*”, Ed. Gordon and Breach Science Publishers, **1985**.
- [184] Nishino, T.; Meguro, M.; Nakamae, K.; Matsushita, M.; Ueda, Y., *The Lowest Surface Free Energy Based on -CF<sub>3</sub> Alignment*. *Langmuir* **1999**, 15, 4321-4323.
- [185] Tamada, K.; Ishida, T.; Knoll, W.; Fukushima, H.; Colorado, R. J.; Graupe, M.; Shmakova, O. E.; Lee, T. R., *Molecular Packing of Semifluorinated Alkanethiol Self-Assembling Monolayer on Gold: Influence of Alkyl Spacer Length*. *Langmuir* **2001**, 17, 1913-1921.
- [186] Zhuravlev, L. T., *The surface chemistry of amorphous silica. Zhuravlev model*. *Colloids and Surfaces A* **2000**, 173, 1-38.
- [187] Fadeev, A. Y.; McCarthy, T. J., *Binary Monolayer Mixtures: Modification of Nanopores in Silicon-Supported Tris(trimethylsiloxy)silyl Monolayers*. *Langmuir* **1999**, 15, 7238-7243.
- [188] Shirahata, N.; Yonezawa, T.; Seo, W.-S.; Kaumoto, K., *Photoinduced Cleavage of Alkyl Monolayers on Si*. *Langmuir* **2004**, 20, 1517-1520.
- [189] Shirahata, N.; Seo, W.-S.; Kinoshita, T.; Yonezawa, T.; Hozumi, A.; Yokogawa, Y.; Kameyama, T.; Masuda, Y.; Kaumoto, K., *Interfacial Observation of an Alkylsilane Self-Assembled Monolayer on Hydrogen-Terminated Si*. *Langmuir* **2004**, 20, 8942-8946.
- [190] Tidswell, I. M.; Ocko, B. M.; Pershan, P. S.; Wasserman, S. R.; Whiteside, G. M., *X-ray specular reflection studies of silicon coated by organic monolayers (alkylsiloxanes)*. *Physical Review B* **1990**, 41, 1111-1128.
- [191] Geer, R. E.; Stenger, D. A.; Chen, M. S.; Calvert, J. M.; Shashidhar, R., *X-ray and Ellipsometric Studies of Self-Assembled Monolayers of Fluorinated Chlorosilanes*. *Langmuir* **1994**, 10, 1171-1176.
- [192] Colorado Jr., R.; Lee, T. R., *Physical organic probes of interfacial wettability reveal the importance of surface dipole effects*. *Journal of Physical Organic Chemistry* **2000**, 13, (12), 796-807.
-

- 
- [193] De Coninck, J.; Ruiz, J.; Miracle-Sole, S., *Generalized Young's equation for rough and heterogeneous substrates: A microscopic proof*. Physical Review E **2002**, 65-036139, 1-4.
- [194] Dupuis, A.; Yeomans, J. M., *Modelling droplets on superhydrophobic surfaces: equilibrium states and transitions*. Langmuir **2005**, 21, 2624-2629.
- [195] Hibert, C.; O'Brien, J.; McCarthy, B.; Kelleher, A. M.; O'Neill, B.; Hughes, P. J., *High aspect ratio silicon nanofabrication technology*. MNE2005 - International Conference on Micro- and Nano-Engineering, Vienna **2005**.
- [196] Lee, W.; Jin, M.-K.; Yoo, W.-C.; Lee, J.-K., *Nanostructuring of Polymeric Substrate with Well-Defined Nanometer-Scale Topography and Tailored Surface Wettability*. Langmuir **2004**, 20, 7665-7669.
- [197] Jiang, Y.; Wang, Z.; Yu, X.; Shi, F.; Xu, H.; Zhang, X., *Self-Assembled Monolayers of Dendron Thiols for Electrodeposition of Gold Nanostructures: Toward Fabrication of Superhydrophobic/Superhydrophilic Surfaces and pH-Responsive Surfaces*. Langmuir **2005**, 21, 1986-1990.
- [198] Ma, M.; Hill, R.-M.; Lowery, J. L.; Fridrikh, S. V.; Rutledge, G. C., *Electrospun Poly(Styrene-block-dimethylsiloxane) Block Copolymer Fibers Exhibiting Superhydrophobicity*. Langmuir **2005**, 21, 5549-5554.
- [199] Journet, C.; Moulinet, S.; Ybert, C.; Purcell, S. T.; Bocquet, L., *Contact angle measurements on superhydrophobic carbon nanotube forests: Effect of fluid pressure*. Europhysics Letters **2005**, 71, 104-109.
- [200] Zhen, Q.-S.; Yu, Y.; Zhao, Z.-H., *Effect of Hydraulic Pressure on the Stability and Transition of Wetting Modes of Superhydrophobic Surfaces*. Langmuir **2005**, 21, 12207-12212.
- [201] Brakke, K. A., *The Surface Evolver*. Experimental Mathematics **1992**, 1, 141-165.
- [202] Stalder, A. F.; Kulik, G.; Sage, D.; Barbieri, L.; Hoffmann, P., *A snake-based approach to accurate determination of both contact points and contact angles*. Colloids and Surfaces A **2006**, 286, 92-103.



---

# ACKNOWLEDGMENTS

First, I would like to express my gratitude to Dr. MER Patrik Hoffmann, my thesis director, for kindly offering me the opportunity to work in his group at the Advanced Photonics Laboratory (IOA) during the last six years, at the beginning as diploma student for almost two years, and later as PhD student. His professional and human support and encouragement have been constant during the whole period, as well as his contagious enthusiasm, and his scientifically valuable teachings and suggestions.

Above all, I would like to thank Dr. Estelle Wagner. Although we formally worked together only one year, her guidance, wisdom and encouragement have been fundamental for the development of this work. Thanks for her valuable contribution in developing the theoretical approach presented in this work, and for having participated in a so active way to the redaction of our first Langmuir article. I am also and especially grateful for her kindness, and precious friendship, which I am sure will survive to the many kilometers that separate us today.

It was an honor for me that Dr. David Quèrè from the ESPCI - Paris, Prof. Henri Gouin, from the University of Marseille, Prof. Paul Muralt from EPFL, and Prof. Max-Oliver Hongler from EPFL accepted to be members of the jury for my thesis. My sincere thanks to all of them.

*Merci* to Ms Regina Frei, for working so hard and doing such a good semester project with me, and to Mr Aurelien Stalder for having developed precious computer programs for contact angle estimations during his semester and diploma works.

I am grateful to Dr. Arie van der Lee of the UMR-CNRS – Montpellier, for his work at the Swiss Light Source – Villigen, for his precious coaching and the nice time together for the characterization of the perfluorosilanized coating thickness.

---

I would like to thank the CMI staff (Center of Micro- and Nanotechnology of the EPFL) for the formation in the clean room, and for having been always present in solving the technical problems during the preparation of all samples studied in this work. My special gratitude to Cyrille Hibert, Georges Racine, and Irene Magnenat.

I would like to thank everyone at IOA for creating an ideal atmosphere to live and work. A special thought to all today and former members of the “NRG” group (Nanostructuring Research Group), in the past “MAD” group (Material Ablation Deposition) for their presence and help both professionally and personally.

“Grazie di cuore” to all Italian friends met at the EPFL, for the nice time spent having lunch and coffee breaks together, and for allowing me to feel not so strong the distance from my country.

Another “sentito grazie” to all my “forever friends”. Even if we are far and we cannot share the daily life, their presence significantly contributes to make me grateful to life.

At the end of this list, my greatest thanks goes to the most important persons of my life: to my brother Gianluigi, for having being a constant support during all my life, for his encouragement, and his love; and to my husband Giovanni and our “big-little” sun Giulia, for being my smile and making me immensely happy in every day of our life together.

## Laura Barbieri

Italian, 34 years, married  
One daughter (Giulia, born December 14th, 2004)  
Tel: +41 (0)76 408 83 85  
E-mail: laura.barbieri72@hotmail.com



### EDUCATION

- June 2002 – 2006     **Ph.D. student**  
at Advanced Photonics Laboratory, Swiss Federal Institute of Technology - Lausanne (EPFL).  
*“Wetting properties of flat-top periodically structured superhydrophobic surfaces”* (Dr. P. Hoffmann)
- April 2002     **Laurea in Chemistry** at Università degli Studi di Genova (Genoa, Italy).  
*“Realization and characterization of perfluoroalkylsilane nano-layers for optical devices”*. Supervisors: Dr. Patrik Hoffmann (EPFL-Lausanne) and Prof. Franco Merlo (University of Genoa).
- July 1991     **High School Diploma in Scientific Studies** at Liceo Scientifico Statale “O. Grassi” (Savona, Italy).

### LANGUAGES

Italian	Mother tongue
English	Good knowledge
French	Fluent in speaking, basic knowledge in writing

### PROFESSIONAL EXPERIENCES

- June 2002 – 2006     **Swiss Federal Institute of Technology of Lausanne**, Advanced Photonics Laboratory (EPFL /STI-IOA-APL)  
- **PhD assistant** in the group of Dr. Patrik Hoffmann.  
Research on the roughness influence on superhydrophobic properties of periodically structures flat-top surfaces.
- Writing and presenting reports in the CTI-TopNano21 program
  - Supervision of semester and diploma students work.
  - Assistant at the course of “Chemistry of surfaces”, 2nd year Microtechnology (EPFL) students.
- Jul 2000 – Apr 2002     **Swiss Federal Institute of Technology of Lausanne**, Advanced Photonics Laboratory (EPFL /STI-IOA-APL)  
- **Research activities** in the group of Dr. Patrik Hoffmann (to obtain the Laurea in Chemistry at the University of Genoa, Italy).

---

*Project title: Realization and characterization of non-wetting nano-scale coatings for precision optics applications (CTI<sup>1</sup> - TopNano 21 project n° 4686.2).*

Jul 1995 – May 2000: Full-time commercial and administrative activities in the consumer credit sector, for Prestitempo<sup>2</sup> Office of Savona, Italy.

### **CONFERENCES AND SCHOOLS**

**NANO-8/2004**, Internat. Confer. on Nanometer-Scale Sci. and Tech., Venice, Italy (oral pres.).

**SPS/2003**, Suisse Physical Society Annual Meeting, Basel, Switzerland (poster).

**Atelier LEA/2002**, Atelier Microtechnique, Arc et Senans, France.

**TopNano21/2002**, Annual Meeting, Berne, Switzerland.

**Workshop on Nanoscience/2002**, Twannberg, Switzerland (Best Poster Award).

**TopNano21/2000**, Annual Meeting, Berne, Switzerland.

**2000- Techniques for chemical analysis of surfaces**, Post formation course at the Materials Institute (EPFL).

### **SCIENTIFIC PUBLICATIONS**

- L. Barbieri, E. Halary-Wagner, P. Hoffmann, *Cassie-Wenzel Transition on Superhydrophobic Pillar-Like Structured Surfaces: Dynamic Contact Investigations with a NON-Negligible Extra-Pressure*, in preparation.
- L. Barbieri, E. Halary-Wagner, P. Hoffmann, *Cassie-Wenzel Transition on Superhydrophobic Pillar-Like Structured Surfaces: Dynamic Contact Investigations with a Negligible Extra-Pressure*, in preparation.
- B. Moser, K. Wasmer, L. Barbieri, J. Michler, *Strength and fracture behaviour of silicon micro-pillars*, accepted for publication on Journal of Material Research, December **2006**.
- L. Barbieri, E. Halary-Wagner, P. Hoffmann, *Water Wetting Transition Parameters of Perfluorinated Substrates with Periodically Distributed Flat-Top Microscale Obstacles*, accepted for publication on Langmuir, November **2006**.
- L. Barbieri, G. Kulik, P. Hoffman, C. Gaillard, A. van der Lee, H.-J. Mathieu, M. Pfeffer, *Flow circuit gas-phase silanization and characterization of highly non-wetting molecular coating*, submitted to Thin Solid Films, January **2006**.
- A. F. Stalder, G. Kulik, D. Sage, L. Barbieri, P. Hoffmann, *A snake-based approach to accurate determination of both contact points and contact angles*, Colloids and Surfaces A: Physicochemical and Engineering Aspects, Vol. 286, p. 92-106, **2006**.
- T. Kasai, B. Bhushan, G. Kulik, L. Barbieri, P. Hoffmann, *Micro/nanotribological study of perfluorosilane SAMs for antistiction and low wear*, Journal of Vacuum Science and Technology B, Vol. 23, p. 995-1003, **2005**.
- B. Bhushan, T. Kasai, G. Kulik, L. Barbieri, P. Hoffmann, *AFM study of perfluoroalkylsilane and alkylsilane self-assembled monolayers for anti-stiction in MEMS/NEMS*, Ultramicroscopy, Vol. 105, p. 176-188, **2005**.

---

1. Commission for Technology and Innovation - Switzerland.

2. Business division of Deutsche Bank SpA, one of the leading companies in Italy for personal loan and installment payment.